Alma Mater Studiorum · Università di Bologna

School of Science

Department of Physics and Astronomy

Master Degree Programme in Astrophysics and Cosmology

Propagation of Ultra High Energy Cosmic Rays in Cosmic Magnetic Fields

Graduation Thesis

Presented by:
Allegra Firinu

Supervisor:
Chiar.mo Professor Franco Vazza

Co-supervisor:
Chiar.mo Professor Carmelo Evoli

Academic Year 2024-2025
Graduation Date III

Abstract

The origin of Ultra High Energy Cosmic Rays (UHECRs) constitutes an open question in Astrophysics, since the presence of Extragalactic Magnetic Fields (EGMFs), that permeate our Universe, can interfere with their propagation by deflecting their trajectories, leading them into a diffusive regime of propagation. This effect, the so-called magnetic horizon, limits the distance that those particles can travel and impacts on the observed spectrum of UHECRs by reducing the detected flux.
Hence, the aim of this Thesis is to quantify the influence of the magnetic horizon studying the propagation of a population of ultra high energy cosmic protons. This is done by the julia-based code UMAREL, specifically designed for this research, which injects protons in a simulated portion of the Universe recreated by the ENZO cosmological simulation which exploits the latest LOFAR observations of the Residual Rotation Measure (RRM). In this way, UMAREL has at its disposal realistic values for the magnetic field strengths and, taking into account the energy loss mechanisms that the protons experience, it can trace hypothetical and feasible trajectories of UHECRs in moving through cosmic magnetic fields. In such manner, it is possible to concretely observe the impact of the magnetic fields on the motion of the particles and to test which propagation regime, among the ones proposed by literature, best reproduces our measurements.

This Thesis is structured as follows: the first chapter is dedicated to an introduction of UHECRs, which starts with a brief historical excursus, followed by a description of the main features that characterise these particles. Afterwards, for this analysis, it is essential to outline the environmental conditions in which UHECRs are expected to propagate, thus two sections are respectively devoted to the depiction of the observed values of the EGMFs and to the explanation of the various energy loss mechanisms suffered by particles moving in different environments.
Successively, a Methods section describes the two pillars of this research: the ENZO cosmological simulation and the UMAREL code, with a description of the many tests taken to explore the propagation under different conditions. Subsequently, the obtained results are inserted in the Results chapter, in which it is displayed an introduction to the Bohm diffusive regime, used as a reference in this Thesis, along with the computational procedure adopted to compare the empirical measurements obtained from the simulation with the theoretical ones. Therefore, the results are contextualised in the Discussion section, in which alternative models to the Bohm normal diffusion are also examined. Lastly, the Conclusions part retraces the main reasoning adopted in this Thesis with the corresponding outcomes reached in this investigation and the possible future perspectives.

Contents

1 Introduction

Cosmic Rays are energetic particles that continuously *rain* on Earth. They consist principally of protons and nuclei (98%) along with a small component of electrons (2%). The cosmic radiation is originally accelerated in proximity of astrophysical sources and then traverses vast distances through the interstellar and intergalactic medium, interacting with various astrophysical environments which contribute in modifying their arrival direction, composition and energy. The birth year of this new branch of Astrophysics is 1912, when Victor Franz Hess (1883-1964), onboard of a baloon, revealed the nature of the increasing ionisation levels of our atmosphere with altitude: he explained that this increase is caused by the interaction of charges coming from space with the molecules of the external layers of the atmosphere, producing new ions (see Fig 2). Later on, in the '20s Robert Millikan (1868-1953) named those extraterrestrial particles *cosmic rays* while in the '30s, Bruno Rossi (1905-1993) demonstrated that they carry a positive electric charge.

Figure 1: Victor Hess, pictured at the center, during preparations for a high-altitude measurement campaign in 1911 (credits: New York Times).

The astrophysical study of the origin and propagation of cosmic rays needed to await the advent of **satellites** in the '60s, by means of which it was discovered that their typical spectrum resembles the one of high energy particles emitted from galactic and extragalactic radio sources.

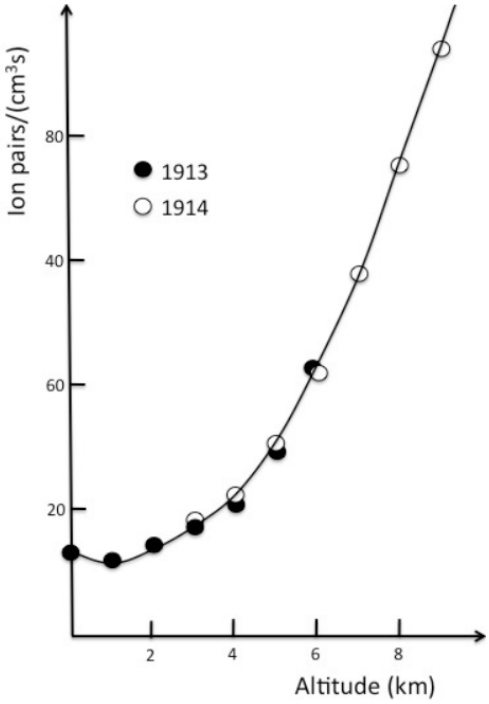

Figure 2: The increasing ionisation level in our atmosphere as the altitude increases (Cronin [18]).

Another crucial result regards the chemical composition resembling the Solar abundances, which, at the GeV order, presents some differences for what concerns lithium, beryllium and boron, that are more copious

in cosmic rays than in the Solar System due to the spallation processes of carbon and oxygen, and manganese, vanadium and scandium produced by the fragmentation of iron (Fig. 6). In this context, spallation refers to a nuclear reaction in which high-energy cosmic ray particles (usually protons) collide with heavier nuclei, causing them to fragment into lighter nuclei and subatomic particles. Moreover, cosmic rays follow an isotropic distribution, which constitutes a seminal outcome in understanding their features.

In the next sections, we will explore different techniques employed to detect cosmic rays, and how they differ based on the observed energy range of the particles (Sec. 1.1). Following this, we will analyze the energy distribution of cosmic rays (Sec. 2), highlighting the fact that the spectrum is a power law with many features which unveil important information about their origin.
We will also investigate the crucial role played by the magnetic field, starting from a description of its key properties and how it affects the propagation of cosmic rays by defining the so-called **magnetic horizon** which represents the maximum distance that a particle is allowed to travel under the effect of the deflections induced by the magnetic field, within the typical energy loss timescale. The end of this chapter will also present the main mechanisms that cause energy losses for cosmic rays, describing how the cosmological expansion and the interaction with the Cosmic Microwave Background work on the energy of the particle.

1.1 Direct and indirect cosmic rays detection

The detection techniques for cosmic rays depend on the energy regime of the particle that, colliding with the atoms and molecules of Earth's atmosphere, produces the so-called *air shower*, a cascade of lighter elements such as pions, muons, neutrinos and electrons that can be observed either from space or from the ground.

Therefore, depending on whether the detection is made before, or after, the interaction of the particle with the medium in which it travels, cosmic rays are classified into **primary** and **secondary**.
The former needs *direct techniques* to be detected, meaning that baloons and satellites are respectively sent at high altitudes and in space, generally above 100 km. In this way, it is possible to intercept cosmic rays and measure their energy, composition and arrival direction, through their nuclear interaction with the device, typically **calorimeters** and **spectrometers**.

Direct detectors are structured in alternating layers of absorbing/passive materials (lead), that induces a shower of secondary particles, and active components such as scintillators that capture the signal of the passing cosmic ray. This device is able to measure the energy of the particle and to identify the type of cosmic ray.
The second exploits the deflection of charged particles into a known magnetic field to derive the momentum, the electric charge and the directionality. Due to the action of the Lorentz force ($\vec{F} = q\,(\vec{v} \times \vec{B})$) the charge is deflected and thanks to the presence of tracking detector it is possible to reconstruct its trajectory and its Larmor radius, which in turns allows to obtain the momentum.
Several experiments based on these methods led to important results. For example, the BESS-polar flight (2007-2008) was an experiment in which a baloon carried at high altitude and equipped with a superconducting magnet spectrometer identified the presence of protons, antiprotons and light nuclei.
Another prominent case was the Payload for Antimatter Matter Exploration and Light nuclei Astrophysics (PAMELA), launched on board of a Russian satellite in June 2006: it was the first satellite-based experiment dedicated to the detection of the antimatter component of cosmic rays.

On the other hand, the study of cosmic rays with energies above $\sim 10 - 100$ TeV cannot rely on the direct detections due to the paucity of the events. However, it is possible to study the air showers produced by the interaction of the primary particle with our atmosphere, using the *Extensive Air Shower Arrays*, a set of detectors covering several thousands of km^2. This is an **indirect method** which exploits the *Cherenkov radiation* phenomenon, according to which a charge moving in a medium with a velocity higher than the speed of light in that medium ($v > c/n$ with n the refraction index), emits radiation along a narrow cone with aperture $\cos\theta_c = 1/n\beta$ and spectrum per unit path dx:

$$\frac{d^2N}{dx\,d\lambda} = \frac{2\pi Z^2}{\lambda^2}\alpha\,\sin^2\theta_c \tag{1}$$

where Z indicates the atomic number, $\alpha = 1/137$ is the fine structure constant and λ the wavelength of the Cherenkov radiation Since the refraction index of our atmosphere depends on density and pressure and increases with altitude, in order to observe this radiation, detectors must be positioned at high altitudes (Cherenkov telescopes), or alternatively, where medium with higher n can be used; for instance water tanks, where $n = 1.33$, allow to observe Cherenkov light within a larger cone $\theta_c \approx 43°$ when the particles pass through purified water.
Moreover, the extension of the cascade strongly depends on the nature of the primary particle: the Heitler model suggests that a γ-ray photon with initial energy E_0 traveling through a medium interacts with the sourroundings generating an e^+/e^- pair, each with energy $E_0/2$. The pair will interact with the ions via Bremsstrahlung generating another γ photon and so on, until the electrons/positrons energy falls below an energy threshold under which the free-free emission will not be possible anymore.
Conversely, if the air shower is started by a proton or a heavy nuclei, the interactions with the atmosphere will provide a more complex cascade, with a wide variety of possible particles such as muons, charged and neutral pions and an electromagnetic shower, meaning that the cascade is expected to be broader.

Thus, the Cherenkov cone is a fundamental tool as it allows the reconstruction of the direction, initial energy and the type of incoming cosmic ray. In fact, the design of Cherenkov telescopes relies on the **stereoscopic technique** to improve angular and energy resolution. It consists of multiple telescopes set at high altitude spread over a large collecting area observing simultaneously the same event in different perspectives: combining the obtained images enables to reconstruct the trajectory of the particle and to define the axis of the Cherenkov cone, which is fundamental to distinguish whether the cascade was originated by a cosmic ray or a γ-ray photon.

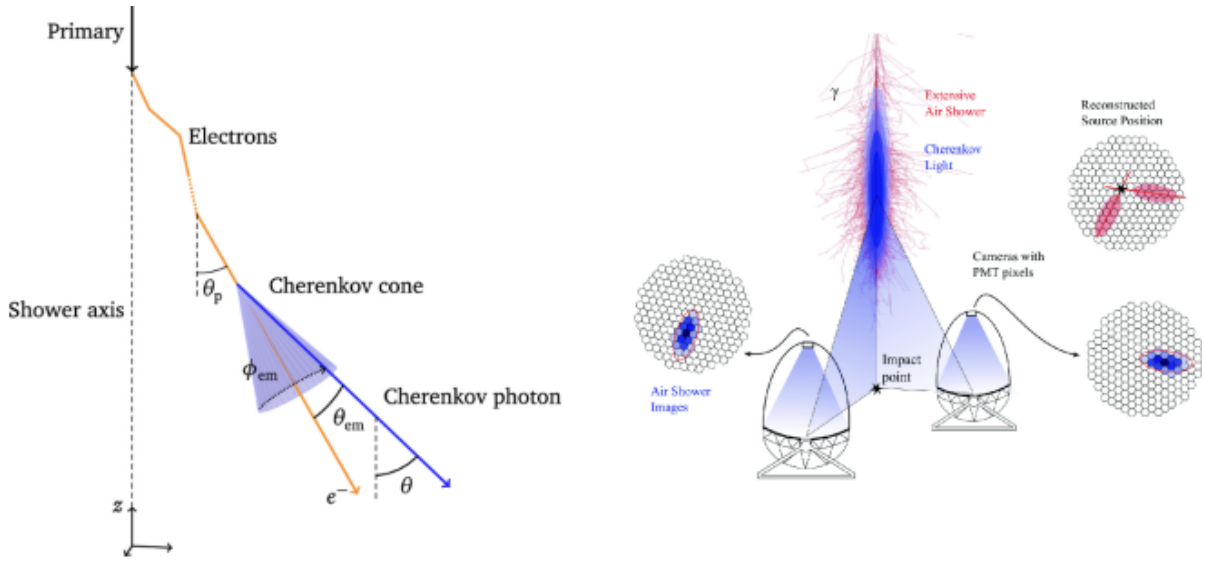

Figure 3: Schematic view of the angular distribution of Cherenkov light in air showersArbeletche and de Souza [6]

The Pierre Auger Observatory (PAO), located in Argentina, constitutes a key example of large-scale arrays. It is the largest detector for ultra high energy cosmic rays, covering an area of $3000\,\mathrm{km}^2$ and receiving, on average, $\sim 30,000$ events/year with energies above 10^{18} eV. It uses two complementary detection methods to estimate the energy, mass and arrival direction of cosmic rays:

- **Surface Detectors (SD)** that consist of 1600 plastic tanks filled with water in order to enable the emission of the Cherenkov light when the charge travels through the medium observing particles day and night. The arrival times at the detectors provide the arrival direction of the primary particle, and the shape of the Cherenkov signal as a function of time in each detector provides composition estimates of the cosmic ray

- **Fluorescence Detectors (FD)** that rely on the fast radiative decay of atmospheric nitrogen molecules excited by the passage of the cosmic ray, allowing an *isotropic* fluorescent emission. This detector operates on clear and dark nights and permits to reconstruct the longitudinal profile of the energy deposition of the shower in the atmosphere, dE/dX where X is the product of the atmospheric density and the traversed length. The height of maximum energy deposition, X_{max} [g cm^{-2}], depends on the nuclear mass A of the particle

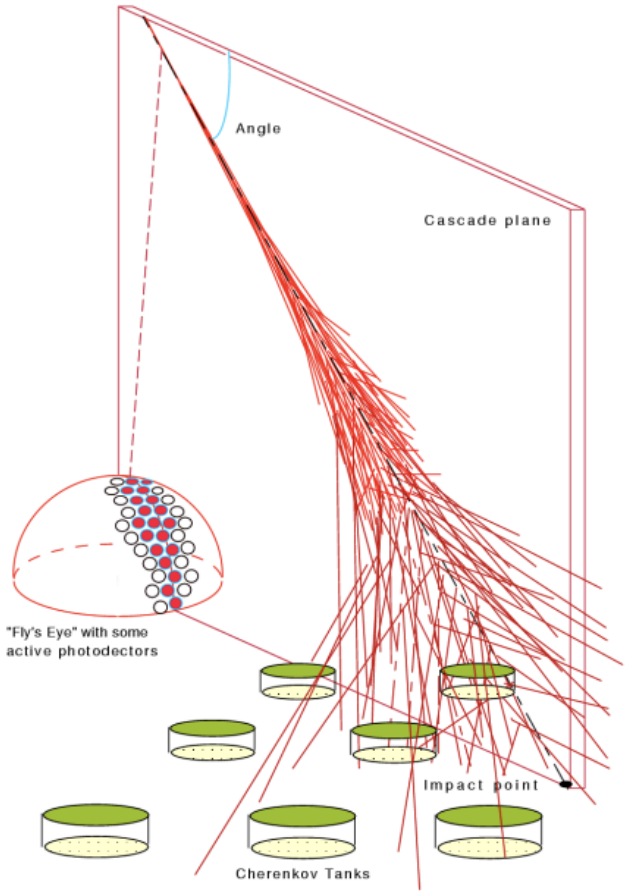

Figure 4: Conceptual design of the Pierre Auger Observatory. A fluorescence detector overlooks an array of water-Cherenkov detector (Watson [57])

Another relevant example is the Telescope Array (TA) in Utah that operates as a scale down version of the Pierre Auger Observatory confirming that these hybrid detectors will help in better constraining the composition and origin of energetic cosmic rays, by collecting more robust events.

1.2 Energy Distribution

Nowadays, thanks to the advanced techniques for the detection of cosmic rays, it is possible to reconstruct their **energy spectrum**, which represents a fundamental tool to disclose the main properties of those particles. The energy distribution observed at Earth spans over a wide range of values, from tens of MeV up to tens of EeV and, to a first approximation, is well described by a power-law:

$$N(E)\,dE = KE^{-\delta}dE \tag{2}$$

which suggests that cosmic rays are a non-thermal population of particles. The plot below (Fig.5) displays the spectrum obtained from various experiments and points out different slopes, depending on the energy

range of detection.

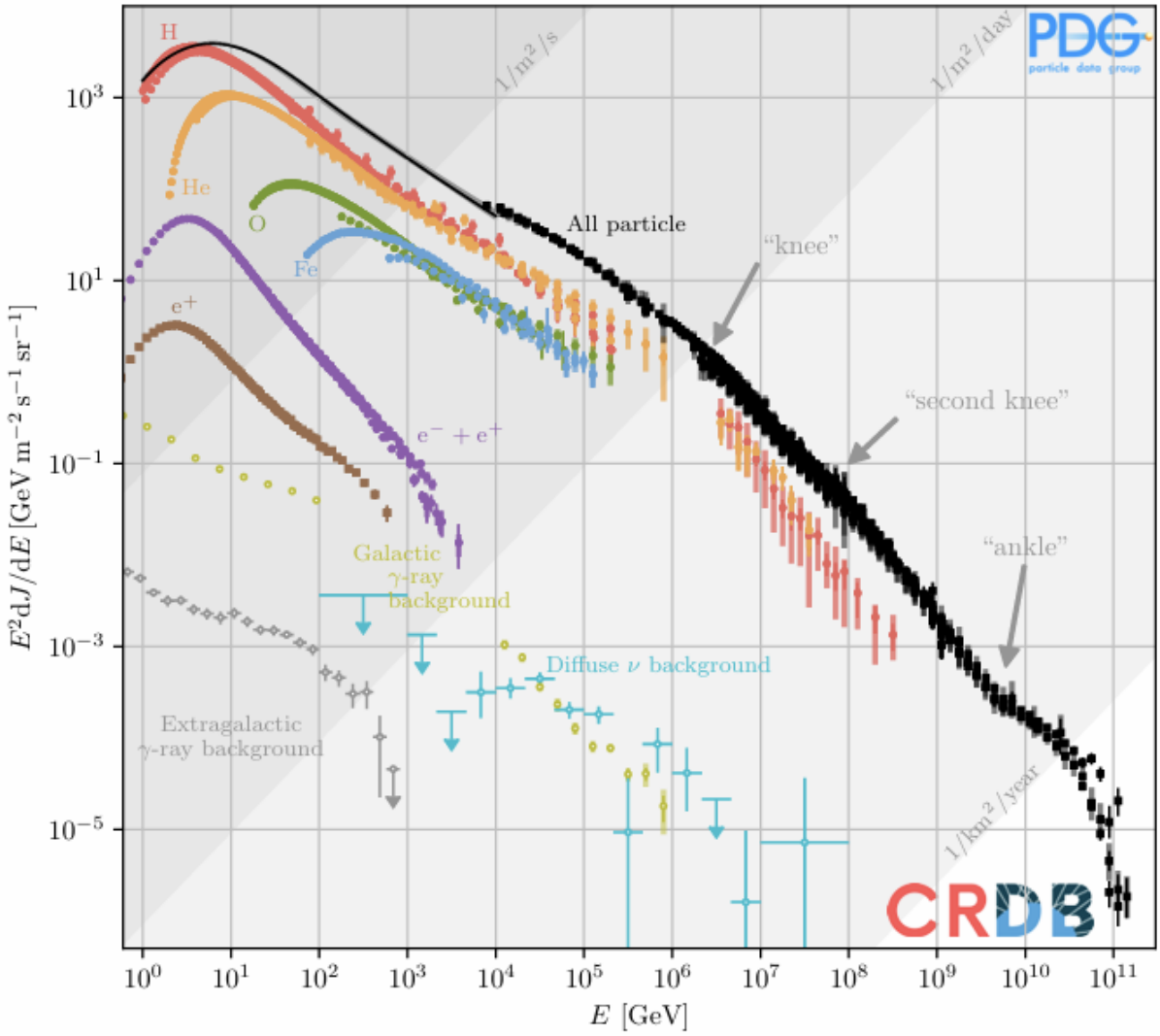

Figure 5: The spectrum of cosmic rays (CRs). Shown are measurements of the intensity of charged and neutral CRs, multiplied by kinetic energy squared. The data for the charged CRs have been extracted from the Cosmic Ray Database (CRDB). The image has been taken from Navas et al. [39].

In Fig.5, we can see that *below* 10 GeV, the spectrum is curved downward, due to the solar modulation effect, caused by the solar outflowing, evidence that the solar activity strongly disturbs the propagation of those particles towards the Earth.

On the other hand, *above* 10 GeV, we can distinguish **three** main structures: at the PeV order there is the **knee**, where the spectrum changes its slope from $\delta \sim 2.7$ to $\delta \sim 3.1$, then, at $\sim 10^{18}$ eV, the hardening of the spectrum highlights the **ankle** and, in the end, the so-called **GZK cutoff**, named after Kenneth Greisen, Georgiy Zatsepin e Vadim Kuzmin, who predicted its existence in 1966, represents the interaction of CRs with photons of the Cosmic Microwave Background and the Extragalactic Background Light.
These features are useful in the determination of the *origin* of cosmic rays: for instance, the knee suggests the transition from a galactic accelerator to another one, whereas the ankle flags the passage from a galactic origin to an extragalactic one, since above 10^{18} eV cosmic rays exhibit a Larmor radius $r_L \propto E/B$ larger than the maximum magnetic field correlation length, thus they are not confined in our galaxy, but are able to escape from it.

For what concerns the *chemical composition* of Cosmic rays, galactic CRs present some similarities with the Solar System composition, suggesting a stellar origin for these particles. However, there are some differences between the solar and the cosmic ray abundances regarding the light elements: Lithium, Berillium and Boron, that are secondary nuclei produced via spallation of heavier elements, are more copious in the CRs, and, similarly, Manganese, Vanadium and Scandium that come from the fragmentation of Iron (see Fig6). This constitutes the proof that they diffuse in the interstellar medium by interacting with other particles via spallation and fragmentation, consequently modifying their chemical properties before reaching us.

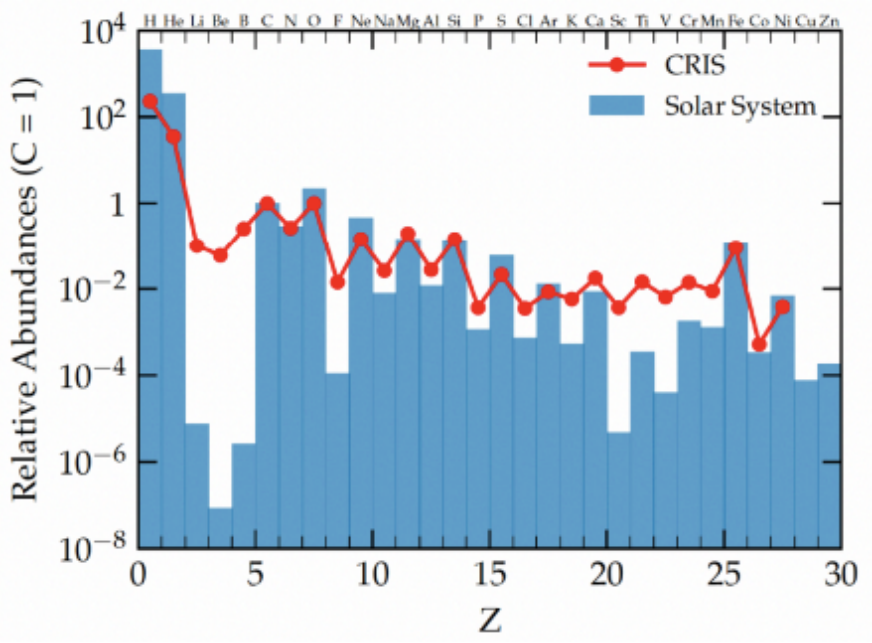

Figure 6: A comparison between the chemical composition of Cosmic Rays (red line) and the chemical abundances in the Solar System Gaisser et al. [24].

Galactic cosmic rays originate mainly due to Supernova explosions occurring in our galaxy, that, thanks to the Diffusive Shock Acceleration mechanisms, are able to boost their energies up to the observed values. However,as mentioned before, the change in the slope at $\sim 10^{16}$ eV from 2.7 to 3.1 suggests that other *PeVatron* accelerators able to explain these energies may exist: possible candidates are Pulsars, which, thanks to the strong electric field induced by their 10^{12} G magnetic fields and their rapid rotation (of the order of ms), could account for these observed energies, but up to now, it is not yet clear whether their contribution is enough.

Now, focusing on the energies beyond the **ankle** ($> 10^{18}$ eV), cosmic rays are also called **Ultra High Energy Cosmic Rays** (UHECRs) and represent the main topic of this research.
These high energies suggest an extragalactic origin also proved by an extremely isotropic distribution of events recorded by the Telescope Array (TA) and the Pierre Auger Observatory (PAO). Indeed, a seminal result in this context is the PAO discovery of a small dipole anisotropy ($\sim 6\%$) at 5.2σ of CRs pointing towards the galactic anticenter for energies larger than $\sim 8 \times 10^{18}$ eV (see Fig.7) which was another confirmation of their extragalactic origin (Collaboration et al. [17]).

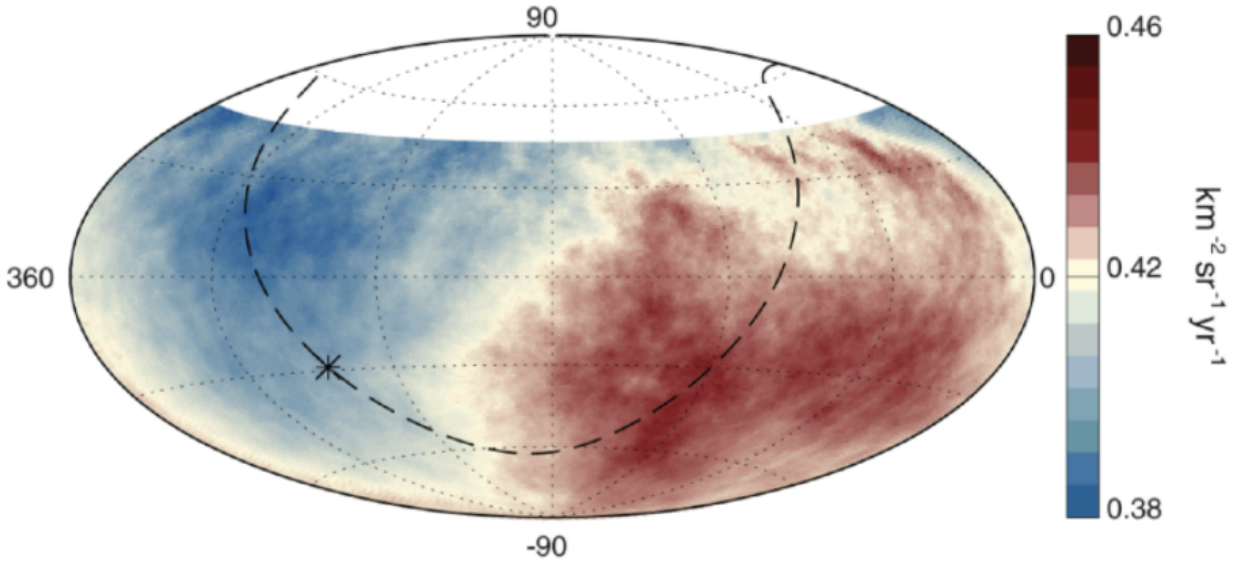

Figure 7: Sky map taken from Collaboration et al. [17] showing the fluxes of particles above 8×10^{18} eV in equatorial coordinates. The galactic center is marked with an asterisk and the galactic plane with a dashed line.

According to the Hillas criterion (Hillas [29]), a necessary condition to accelerate cosmic rays to energies higher than the ankle is the *confinement of the particles* in the acceleration region, suggesting, as possible accelerating sites, accreting compact objects such as neutron stars and supermassive black holes. In other words, sources of UHECRs must be able to confine the particle for one gyration, meaning that their size R needs to be larger than the Larmor radius of the particle, and have a motional electric field large enough to reach a given energy within the source. Thus, if a particle escapes from the region where it was accelerated, it will be unable to gain more energy. This situation imposes a limit on the maximum energy E_{max} of CR that can be expressed as follows:

$$E_{max} \approx 10^{21}\,\mathrm{eV}\, Z\beta \left(\frac{R}{1\,\mathrm{Mpc}}\right)\left(\frac{B}{\mu\mathrm{G}}\right) \tag{3}$$

where R is the size of the object and B its magnetic field. Eq.3 can be translated into a diagram (Fig.8) that shows classes of objects in terms of the product of their radial size R and magnetic field B: regardless of the specific acceleration mechanism, only objects above the line can be sources capable of confining CRs until they become UHECRs.

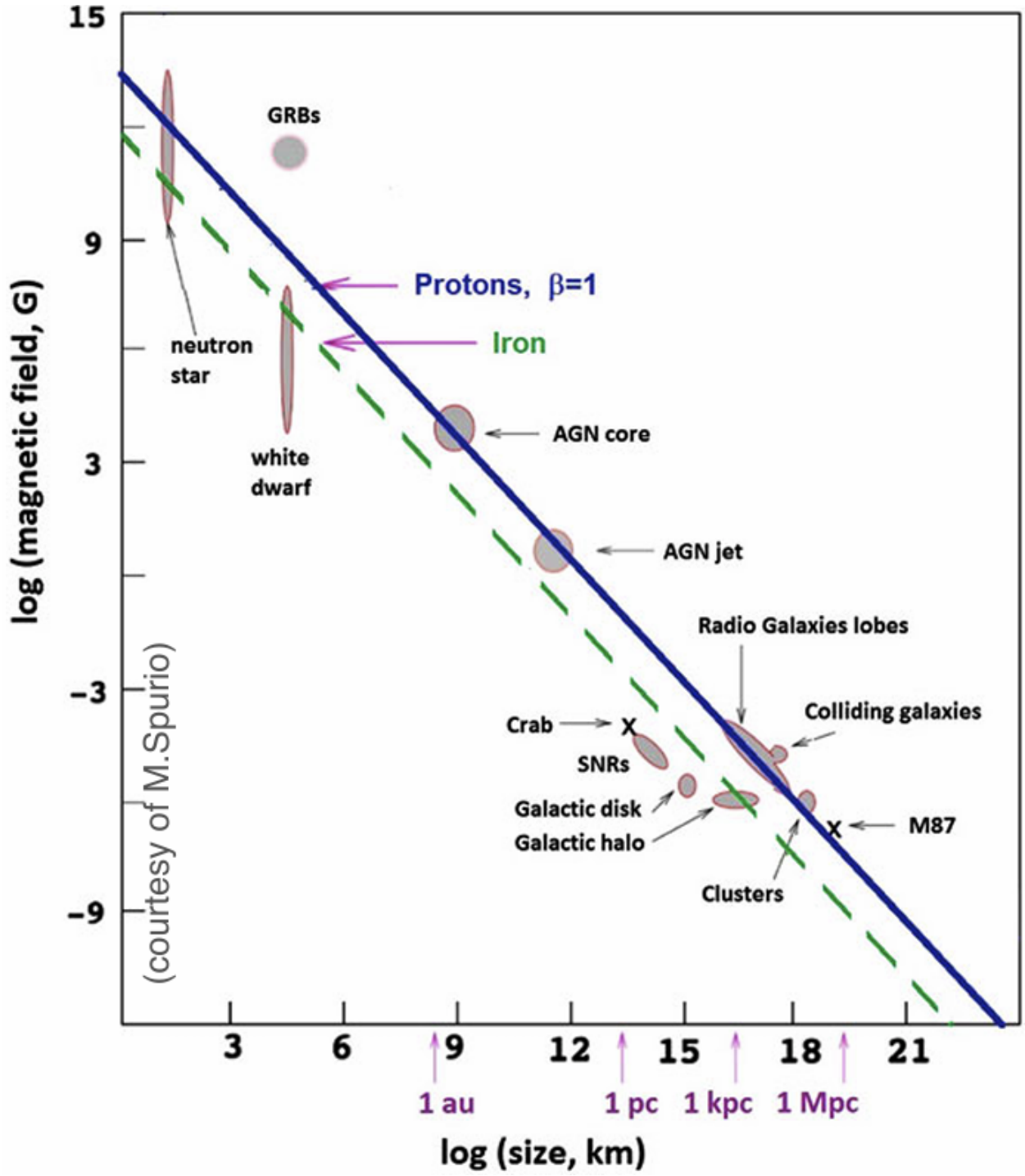

Figure 8: Hillas diagram displaying which size and magnetic field an object should have to be considered a source of UHECRs. The plot shows that only a few objects in the Universe can fulfil both conditions for generating 10^{20} eV protons (Adamo et al. [2]).

However, in order to reach 10^{20} eV other interesting candidates are considered, such as **Gamma Ray Bursts** (GRBs) where the interaction of relativistic expanding fireball and the surrounding medium may generate a shock, able to boost particles to the needed energy. **Active Galactic Nuclei** constitutes possible site for particle acceleration thanks to Fermi II, diffusive shock acceleration mechanisms and magnetic reconnection occuring at the jet base; additionally, winds driven by **starburst galaxies** may contribute for

energizing particles at those levels.

Actually, we should also consider that the propagation of UHECRs of a given energy can also depend on the energy loss mechanisms. In fact, most recent observations suggest that additional spectral features emerge above 10^{18} eV (Biteau [8]): a flattening of the spectrum, known as the *instep*, followed by a flux suppression, called the *toe*, denotes that the propagation of nuclei beyond the ankle is limited due to the interaction with the photons of the Cosmic Microwave Background (CMB) and the infrared component of the Extragalactic Background Light (EBL) causing an **energy loss**, responsible for this observed drop. In this regard, the most detailed modelling of the spectrum above 10^{19} eV proposes that the presence of a GZK cutoff is more compatible with a sequence of heavier nuclei sorted in mass number: in fact, the PAO found evidence that the composition of UHECRs gets heavier to higher energies, as shown in the figure below taken from Abdul Halim et al. [1].

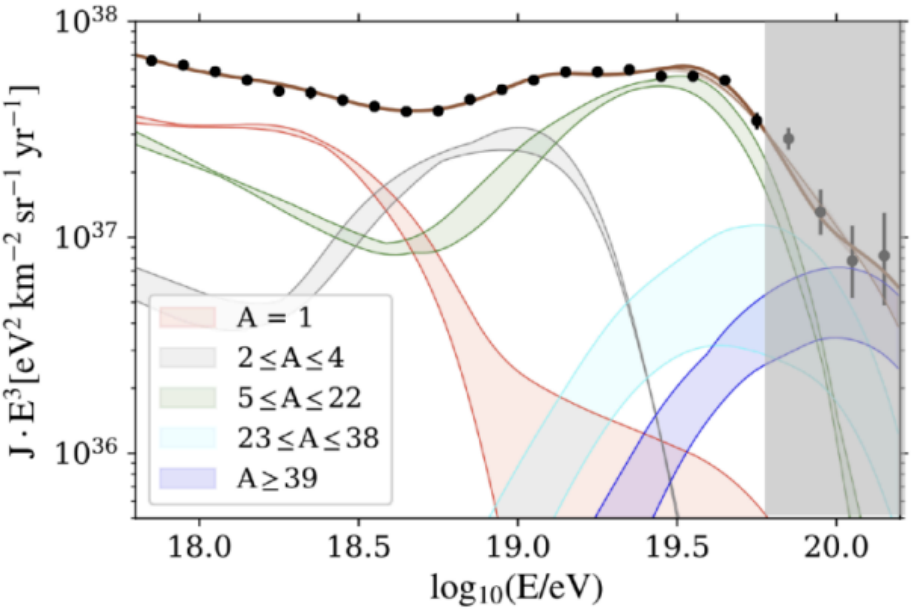

Figure 9: Modelled flux on Earth: dotted lines in the spectrum plots represent the flux coming from the primary nuclei while solid lines correspond to the total flux (primary plus secondary) of each mass group.

In addition, as these particles traverse vast distances, their paths are further distorted by the presence of large-scale magnetic fields, affecting the propagation of cosmic rays for which we can define the average deflection angle for a source at a distance D larger than the correlation length l_B:

$$\theta \approx 0.8^\circ \times Z \left(\frac{E}{10^{20}\,\mathrm{eV}}\right)^{-1} \left(\frac{D}{10\,\mathrm{Mpc}}\right)^{1/2} \left(\frac{l_B}{1\,\mathrm{Mpc}}\right)^{1/2} \frac{B}{1\,\mathrm{nG}} \tag{4}$$

Indeed, these deflections allow us to define the **magnetic horizon** that adds uncertainties to the reconstructions of their original direction, thereby complicating the identification of their astrophysical sources. For this purpose, my Thesis wants to answer the following question:

what is the role of magnetic fields in the propagation of UHECRs?

1.3 Extragalactic magnetic fields: models and observations

Magnetic fields play a crucial role in Astrophysics since they represent an ubiquitous element in the Universe, observed across different cosmological epochs and over a wide range of scales, from planets and stars to galaxy clusters, cosmic filaments and even in rarefied environments.
In fact, observational and theoretical studies suggest that the strength of magnetic fields correlates with the density of the surrounding medium: denser regions, such as galaxy cluster cores, typically host magnetic

fields at the μG level, while less dense environments like filaments or voids exhibit fields in the nG range or below. This behaviour can be explained through the adiabatic compression of an initial seed field during structure formation. In the simple case of adiabatic compression during a spherical collapse, under the assumption of ideal magnetohydrodynanic (MHD) and in the absence of significant turbulence or dynamo amplification, the field lines are frozen into the plasma whose compression results in compression of flux lines. Thus, the expected growth of the magnetic field strength scales with gas density, as a consequence of magnetic flux conservation:

$$B = B_0 \left(\frac{n}{n_0}\right)^{2/3} \tag{5}$$

where B_0 and n_0 represent, respectively, the magnetic field and gas density at an initial epoch (see Pignataro, G. V. et al. [44]).

Indeed, according to the Λ Cold Dark Matter (ΛCDM) model, the formation of structures is able to explain the strengths of the magnetic fields in dense regions, as observed in the centre of galaxy clusters and filaments. In fact, the hierarchical merge of small structures into progressively large systems can be considered the responsible for the formation of turbulent gas motions and magnetic dynamo that allow the amplification of any seed field up to the observed values of the μG order (Donnert et al. [20]).

Other observational evidence that supports the connection between the gas density and the magnetic field strength is for example, a recent estimates based on the Rotation Measure of background polarised sources behind or within the Coma cluster which revealed a central magnetic field of $3 - 7\,\mu$G which scales with the ICM thermal density as $B \propto n_{th}^{0.5-1}$ (Bonafede et al. [9]), in agreement with the theoretical 2/3 exponent of Eq.5.

This observational scaling between magnetic field strength and gas density, together with the amplification mechanisms expected in the ΛCDM scenario, can be formally described by the **induction equation** of magnetohydrodynamics. In the ideal MHD limit, the magnetic field evolution in the ICM is given by:

$$\frac{\partial \mathbf{B}}{\partial t} = -\mathbf{v} \cdot \nabla \mathbf{B} + \mathbf{B} \cdot \nabla \mathbf{v} - \mathbf{B} \nabla \cdot \mathbf{v} + \eta \Delta \mathbf{B} \tag{6}$$

where the first term represents the advection of field lines, the second one the stretching, the third the compression and the fourth the magnetic field dissipation, with $\eta = c_s/4\pi\sigma$ accounting for the diffusivity and σ for the conductivity. Because the ICM can be assumed to be a nearly perfect plasma, with the thermal pressure $n_{th} k_B T$ larger than the magnetic one $B^2/8\pi$, characterised by high conductivity and low diffusivity ($\eta \sim 0$), Eq.6 predicts that the magnetic fields are frozen into the plasma and advected with the bulk motions of the medium (Ostriker [40]). Moreover, Eq.6 is a conservation equation for magnetic flux, implying that magnetic fields have to be seeded by some mechanisms also at high redshift. As reported in Donnert et al. [20], it is reasonable to assume some form of turbulent dynamo processes in the clusters and filaments, but it is also fundamental to consider plasma-physical arguments to understand the fast growth of seed fields by many orders of magnitude. For example, there are clear theoretical predictions, as the *small-scale dynamo*, according to which magnetic field amplification by turbulence is a consequence of the stretching and folding of pre-existing field lines by the random velocity field of turbulence, which amplifies the field locally due to flux conservation. Still, astrophysical environments differ significantly from these idealized models: structure formation drives turbulence localized, episodic and multi-scale in the presence of a strong gravitational potential in galaxy clusters.

Thus, advanced simulations, combined with radio observations, attempted to better constrain a possible origin of *cosmic magnetism* and to quantify the influence that these seeding mechanisms have on the final magnetic field. According to numerical works, the micro-Gauss magnetic field measured with Faraday Rotation and synchrotron emission are compatible with many different origin scenarios converging to a dynamo effect started by a non-zero seed magnetic field.

- According to the **primordial origin** scenario, magnetic fields seem to be already present at the epoch of Cosmic Microwave Background and got later advected, compressed and amplified up to the observed value within galaxy clusters and groups, explaining why the magnetic cosmic web follows the same pattern as the matter cosmic web as shown in Fig. 10c. Some of the proposed scenarios involve the generation of currents during inflation, phase transitions and baryogenesis, just to name a few (Harrison

[28], Kahniashvili et al. [30], Durrer and Neronov [22]). According to these models, these primordial seed fields may produce small coherence lengths, whose structure may still persist today, also in the cosmic voids in a large range of seed fields value, from 10^{-34} to 10^{-9} G.

- On the other hand, magnetic field seeds can be injected in the cosmic web by **astrophysical sources**. Semi-analytical simulations of magnetized winds (Bertone et al. [7]) have shown that starburst galaxies are able to seed the Intergalactic Medium with magnetic fields, with values ranging between $10^{-12} - 10^{-8}$ G, later amplified thanks to turbulent diffusion and dynamo processes. In addition, jets and winds from active galactic nuclei seem to be possible candidates for the magnetisation of the central regions of clusters and groups (Dubois and Teyssier [21], Xu et al. [58]), as well as of filaments, while numerical simulations showed that these mechanisms alone cannot account for the magnetic field strength of $\geq 10^{-15}$ G detected in voids through the analysis of γ-ray observations (Bondarenko et al. [10], Tjemsland et al. [48]).

It is reasonable that something in between the primordial and the astrophysical scenarios, like additional processes such as the Biermann battery mechanism (see [34]), might provide additional seeding of magnetic fields across cosmic evolution.
To test and constrain these scenarios, observations play a crucial role. In particular, measurements of the **Faraday rotation** from polarized radio sources and the synchrotron emission coming from cosmic filaments and galaxy clusters of the cosmic web allow us to estimate the distribution and strengths of magnetic fields *beyond* dense and collapsed structures.

To contextualize the theoretical discussion, we now turn to specific observations that have allowed researchers to constrain magnetic fields strengths in different environments.
As previously mentioned, cosmic structures grow following merging processes that cause strong shocks, that, beside amplifying the magnetic field, are also able to accelerate the surrounding particles up to relativistic energies, leading to an extended radio emission observed in galaxy clusters and filaments via the emission of synchrotron radiation.

While this phenomenon is routinely observed *within* clusters of galaxies ([51]), in a few cases it has also been observed *outside* clusters of galaxies and it offers a potential way of probing magnetic fields in an environment which may still retain memory of primordial magnetic seeding events.

A relevant example is the case of **Abell 0399** and **Abell 0401**, two merging clusters separated by a projected distance of 3 Mpc in which a radio bridge shows diffuse synchrotron emission corresponding to a magnetic field strength of $\sim 0.5\,\mu$G, as inferred from measurements conducted by LOFAR-High Band Antenna ([12]), highlighting the presence of magnetic fields and relativistic particles on scale larger than those of galaxy clusters. Complementarily, the Planck spacecraft observed a signal due to the Sunyaev-Zeldovich effect which showd the large-scale filament of gas connecting the two systems (Ade et al. [3])

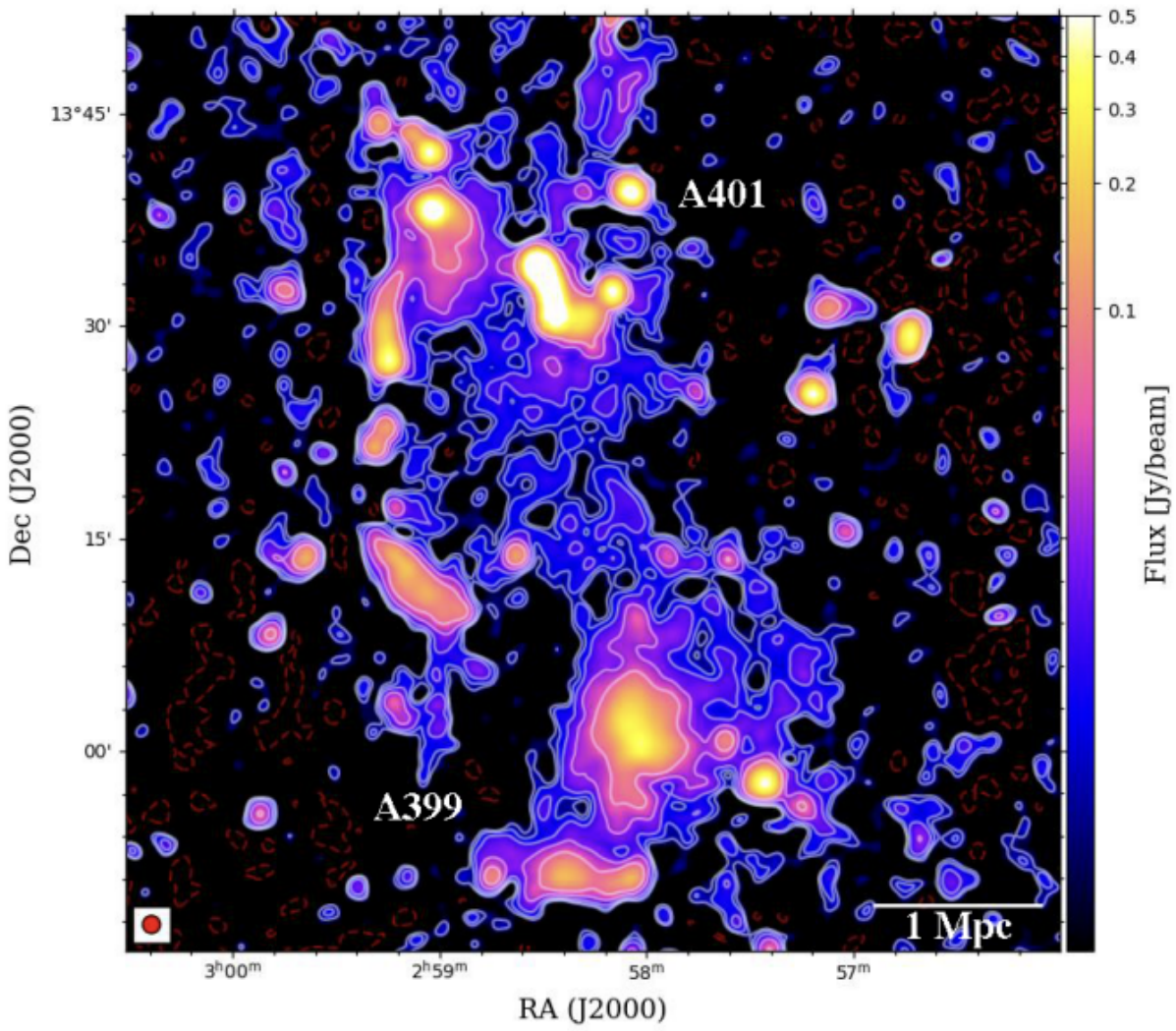

Figure 10: Radio image at 60 MHz of the A399-A401 clusters pair with compact sources and the $\sigma_{\rm rms} = 3\,{\rm mJy\,beam^{-1}}$ taken from Pignataro, G. V. et al. [43]. The color scale indicates the flux density in Jy/beam, with contour levels, in white, starting at $2\sigma_{\rm rms}$, $3\sigma_{\rm rms}$ and then increase to $20\sigma_{\rm rms}$ with factor of 2. The negative contour level $-3\sigma_{\rm rms}$ is in red.

Similarly, two other clusters connected by filaments of 10-20 Mpc present a faint diffuse emission, ascribable to a $\leq 0.25\,\mu G$ magnetic fields, which can be used to derive an upper limit for the magnetisation of these extended structures ([36]).

Moreover, diffuse radio emission has been detected on even larger scales, allowing to statistically estimate upper limits on the amplitude of the magnetic field by cross-correlating signals between the large-scale distribution of galaxies detected through optical and Infrared surveys and the radio observations of Murchison Widefield Array (MWA). The lack of correlation suggests an upper limit of $\sim 0.1\,\mu$G on the average magnetisation of the cosmic web at redshift $z \leq 0.1$ (Brown et al. [11], Vernstrom et al. [55]).

Beside the observation of the synchrotron emission, another useful tool is the Faraday Rotation Measure (RM), a measure of the polarization angle rotation produced when polarized radiation travels through a magnetized medium populated by free electrons. Since the RM depends on the magnetic field component along the line-of-sight (LOS), weighted by the electron number density, and integrated along the LOS from the source to the observer ($RM = \int_{los} n_e H_{||}\, dl$), it enables a sort of tomography of the cosmic web, provided a sufficiently dense grid of background sources is present (Akahori et al. [4], Vacca et al. [49]). This approach is limited by the low amount of polarized sources, but this limitation is expected to be addressed in the

future with instruments such as the Square Kilometer Array (SKA) (Locatelli et al. [35]). A recent study by Pshirkov et al. [45] based on the lack of evolution of RM in sources observed with the NRAO VLA Sky Survey placed upper limits for the extragalactic magnetic field in the range of $0.65 - 1.7$ nG.
By cross-correlating the Rotation Measure signal of 1742 radio galaxies from the NVSS survey (Taylor et al. [47]) with the distribution of optical and infrared galaxies at redshift $z \leq 0.5$, Amaral et al. [5] recently set an upper limit of 3.8 rad/m^2 for the contribution of the magnetised cosmic web, which may suggest a ≤ 30 nG on the magnetisation of the cosmic web on 1-2.5 Mpc.
Another method to constrain intergalactic magnetic fields involves the measurement of the excess RM between random pairs of extended radio galaxies by comparing the ΔRM differences as a function of angular separation between physically associated radio galaxy pairs and randomly aligned lobes (Stuardi et al. [46], Vernstrom et al. [56]). In particular, O'Sullivan et al. [41] analyzed 349 radio galaxies observed with the LOFAR-HBA and found that the RM difference between physical and random pairs was $|\Delta \mathrm{RM}^2| \leq 1.9\,\mathrm{rad}^2/\mathrm{m}^4$ which constraints the magnetisation of cosmic matter to ≤ 4 nG.
Another key reference for this Thesis is the study conducted by Carretti et al. [15] which uses a LOFAR catalogue of RMs defined as a combination of a Galactic and an extragalactic terms. Their analysis lead to a present day magnetic field in filaments (far from possible magnetic sources) of $B \sim 11 - 15$ nG, favouring a primordial magnetogenesis scenario.

At the opposite side of the electromagnetic spectrum, an additional tool to detect intergalactic magnetic fields is the use of blazars. The jets produced by blazars can emit very high energy γ-rays, up to the $1 - 10$ TeV regime. The TeV photon can encounter a UV-optical photon of the Extra-galactic Background Light (EBL), and when this happens the TeV photon scatters off the EBL one allowing the production of an electron-positron (e^+e^-) pair. In turn, the pair can travel short distances before interacting with a CMB photon via Inverse Compton, thus creating a GeV photon which, along with all the other produced GeV photons, will be observed as a GeV halos. The presence of the intergalactic magnetic field can strongly affect the propagation of the pair by bending their trajectories, and if the field is strong enough, the final GeV halo will not be visible. The non-observation of the halo allows to infer lower limits on the strenght of the magnetic field. According to this technique, assuming a Larmor radius $R_L = E_e/eB \sim 100\,\mathrm{Mpc}$ for an e^+/e^- with energies $E_e \sim 1$ TeV subjected to a bending angle of 0.1°, the magnetic field should be $\sim 10^{-17}$ G. The Figure below, taken from Vachaspati [50], displays the *three legs* in the TeV photon journey from the blazar to the Earth.

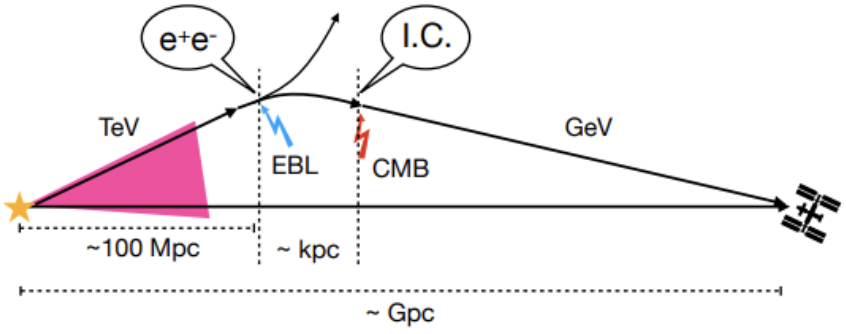

Figure 11: The three legs of the TeV photon's journey from the blazar to the observer in the presence of an inter-galactic magnetic field. The first TeV leg is terminated by pair production off an EBL photon, the second leg is in the form of lepton pairs and is terminated by an inverse Compton (I.C.) scattering event. The final GeV photon leg then propagates to the detector, perhaps onboard a satellite. Vachaspati [50]

Finally, more indirect constraints on the amplitude of magnetic fields on the largest scales have been inferred from the Cosmic Microwave Background which can be turned into an estimate on the current magnetisation of voids giving fields in the range of approximately 10^{-16} to 10^{-9} G (Vazza et al. [54]).

1.4 Propagation of Cosmic Rays in Magnetic Fields

Regardless its origin, the presence of a magnetic field strongly affects the propagation of cosmic rays by deflecting their trajectories. We define the **Larmor radius** as the characteristic radius of the circular motion that a charged particle describes when moving through a magnetic field due to the action of the Lorentz force:

$$r_L = \frac{p\,c}{qBc} \approx \frac{E}{ZeBc} \tag{7}$$

where p is the momentum, $q = Ze$ the charge, B the magnetic field and E the energy of the cosmic ray which is linked to its momentum as:

$$E = \sqrt{(pc)^2 + (m_0c^2)^2} \tag{8}$$

This means that particles moving nearly at the speed of light have energies $E \sim pc$. The general equation of motion of a charged cosmic ray is:

$$\frac{\mathrm{d}(\gamma\, m\vec{v})}{\mathrm{d}t} = \gamma\, m\frac{\mathrm{d}\vec{v}}{\mathrm{d}t} = q\,(\vec{E} + \vec{v}\times\vec{B}) \tag{9}$$

where the electric field $\vec{E}$ can be neglected since in most astrophysical plasma, it is rapidly short-circuit by the motion of free charges, thus the dynamics of charges is mainly governed by the Lorentz Force.
In order to understand how cosmic rays propagate through magnetized environment, is also important to consider the interplay between three characteristic velocities involved in the process:

- the particle velocity $v \sim c$, which reflects the relativistic motion of the particles;
- the Alfven speed $v_A = \frac{B}{\sqrt{\mu_0\rho}}$ that represents the propagation speed of the magnetic field perturbation in the plasma;
- the bulk gas velocity v_{gas} which accounts for the motion of the fluid in which particles travel;

Additionally, we define three relevant spatial scales :

- the particle Larmor radius $r_L = \gamma mv/qB$, which is the typical radius of gyration of a charged particle in a magnetic field;
- the length scale of magnetic fluctuations $l_B \sim |B/\nabla B|$, characterizing the spatial variation of the magnetic field;
- the length scale of gas velocity fluctuations, L, that represents the typical size over which the bulk gas velocity varies significantly;

In this way it is possible to distinguish different modalities of propagation of cosmic rays, depending on the combination of the above quantities:

- **ballistic** propagation occurs when $r_L \gg l_B, L$ and $v \gg v_A, v_{gas}$, which is typical for particles moving in a slowly varying magnetic field;
- **diffusive** propagation takes place in highly magnetised medium, when $r_L \ll l_B$ and $v_A \gg v_{gas}$;
- **turbulent** transport happens when $r_L \ll l_B \leq L$ and $v_{gas} \gg v_A$;

The regime treated in my Thesis depends on the current energy of the particle, but overall the propagation of our UHECRs follows a diffusive transport.
Another key quantity fundamental to the study of the propagation of CRs through magnetic fields is the **rigidity** defined as:

$$R = \frac{E}{Ze} \quad [\,\mathrm{V}\,] \tag{10}$$

which refers to the resistance of a charge against deflections in a magnetic field B. Since the rigidity is linked to the *gyroradius* of the particle via $r_g = R/B$, this implies that the higher the rigidity the smaller the curvature of the particle's trajectory, thus the less relevant the impact of the magnetic field on the particle.

1.4.1 Ballistic propagation

For the specific case of **ballistic** propagation of a cosmic ray in a quasi-static magnetic field (when $|\Delta B/B| \leq 1$), the effect of the magnetic field on the particle can be described by the **magnetic rigidity**:

$$R = \frac{E}{Ze} \quad [\,\mathrm{V}\,] \tag{11}$$

which refers to the resistance of a charge against deflections in a magnetic field B. Since the rigidity is linked to the *gyroradius* of the particle via $r_g = R/B$, this implies that the higher the rigidity the smaller the curvature of the particle's trajectory.

If we consider a charged particle gyrating around its guiding center (which is the axis of the particle's trajectory) in a magnetic field, it can be seen as a current loop, with $i = Zev_\perp/2\pi r$ and associated area $A = \pi r^2$, where $v_\perp$ is the velocity component perpendicular to the magnetic field. Thus, we define the magnetic moment μ of the current loop as:

$$\mu = iA = \frac{zev_\perp r}{2} = \frac{m_0 v_\perp^2}{2B} = \frac{w_\perp}{B} \qquad r = \frac{m_0 v_\perp}{zeB} \tag{12}$$

where $w_\perp$ is the kinetic energy of the particle in the perpendicular direction of the guiding center. In such conditions, the slowly varying magnetic field will induce an electromotive force ε which works on the particle per orbit as:

$$Ze\varepsilon = ze\pi r^2 \frac{\mathrm{d}B}{\mathrm{d}t} = ze\pi r^2 \frac{\Delta B}{\Delta T} \tag{13}$$

Given the period of one orbit $\Delta T = 2\pi r/v_\perp$, the change in kinetic energy is:

$$\Delta w_\perp = \frac{zerv_\perp}{2}\Delta B = \frac{m_0 v_\perp^2}{2B}\Delta B = \frac{w_\perp}{B}\Delta B \tag{14}$$

and corresponds, in terms of magnetic moment, to:

$$\Delta\mu = \Delta\left(\frac{mv_\perp^2/2}{B}\right) = \frac{\Delta(mv_\perp^2/2)}{B} - (mv_\perp^2/2)\frac{\Delta B}{B^2} = 0 \tag{15}$$

This means that the magnetic momentum μ is conserved under slow variations of magnetic field. As a consequence, $mv_\perp^2/2B = const$, $p_\perp^2/B = const$ and implies that $\Delta(B\, r_L^2) = 0$ which describes that if the orbit shrinks, the magnetic field must increase as r_L^{-2}. Those are known as the *adiabatic invariants* of a particle's motion.

1.4.2 Diffusive propagation

Now, we will address the **diffusive** propagation of cosmic rays in case of a tangled magnetic field: this process is represented by a *random* walk, in which every step in the propagation is fully independent from the previous. This indicates that the average displacement of particles after N step is:

$$\langle \vec{r} \rangle = \sum_i \vec{r}/N \approx 0 \tag{16}$$

which means that the distribution of trajectories broadens with times:

$$\langle r^2 \rangle^{0.5} = (\sum_i r_i^2/N)^{0.5} > 0 \qquad \langle r^2 \rangle \sim N l_0^2 \tag{17}$$

where l_0 is the typical length of a single step.

Having the correlation between time t and number of steps N it is possible to write the **diffusion coefficient D** as

$$D \sim \frac{N l_0^2}{t} \sim v l_0 \tag{18}$$

which, in the three dimensional case, takes the form as $D \sim vl_0/3$. The diffusion of relativistic particles in a plasma is well described by the **Bohm diffusion model** which assumes that for particles nearly propagating at the speed of light ($v \sim c$) in an entirely random magnetic field, the Bohm diffusion coefficient is:

$$D_{Bohm} = 3 \times 10^{22} \times \frac{E\,[\mathrm{GeV}]}{B\,[\mu\mathrm{G}]} \quad [\frac{\mathrm{cm}^2}{s}] \tag{19}$$

This relation highlights that the diffusion coefficient of cosmic rays depends on their energy which in turn defines the Larmor radius.

1.4.3 Turbulent propagation

Another important mechanism that should be considered is the **turbulent** propagation, according to which the evolution of propagation of cosmic rays is correlated in time and space, thus it follows statistical laws connected with the physics of the flow which allow us to outline the properties of the fluid.
The combination of diffusive and turbulent models constitute a more sophisticated one, which assumes that the magnetic field presents structures that cover scales of $\sim L_0 \gg r_g$, so that cosmic rays can diffuse over longer distances. We define the *turbulent coefficient* D_{turb}:

$$D_{turb}(E) \propto 2 \times 10^{29} (\frac{E[\mathrm{GeV}]}{B[\mu\mathrm{G}]})^{1/3} (\frac{L_0}{20\,\mathrm{kpc}})^{2/3} \quad [\mathrm{cm}^2/\mathrm{s}] \tag{20}$$

which shows a shallower dependence on the particle energy if compared with the Bohm coefficient presented in the previous section.

1.5 Energy Losses

Another important physical ingredient that regulates the evolution of relativistic particles, including the one studied in my Thesis, is represented by the **energy losses**.
Indeed, cosmic rays can interact with the surrounding environment through several mechanisms depending on the type of particle.

At these high energy regimes, *protons* can lose their energy due to:

- **cosmological expansion** for which we define the energy loss length l through:

$$l^{-1} \equiv \frac{1}{E}\frac{dE}{dx} \tag{21}$$

  Having the Hubble constant $H_0 = -\frac{1}{E}\frac{dE}{dx}$, the maximum distance travelled by an UHECR at the speed of light is $l_{ad} = \frac{c}{H_0} \simeq 4$ Gpc. This mechanism is dominant in the low energy regime, particularly affecting particles with energies lower than 10^{18} eV;

- **interaction with photons** of the Cosmic Microwave Background (CMB) which permeates all space. In the rest frame of the cosmic ray, those photons have very high energies and this can lead to:
  - *pion-production*: CMB photons have frequency $\nu \sim 1.5 \times 10^{11}$ Hz and energy $\langle \epsilon_{CMB} \rangle \sim 6 \times 10^{-4}$ eV. The production of pions can take place if the photon has an energy ϵ larger than the one of the cosmic proton $\epsilon_{\gamma p}$ in the particle rest frame ($\epsilon_{\gamma p} = 200$ MeV). If this is the case, then the following reactions can occur:

$$p + \gamma_{CMB} \rightarrow \Delta^+ \rightarrow \begin{cases} n + \pi^+ \\ p + \pi^0 \rightarrow p + \gamma + \gamma \\ p + N\pi \end{cases} \tag{22}$$

    where Δ^+ is the Delta baryon with a mean lifetime of $\approx 10^{-24}$ s and mass $\sim 1232\,\mathrm{MeV/c^2}$. In turn, the neutral pion π^0 will decay in two photons, the charged pion π^+ into a charged muon μ^+ and a muonic neutrino ν_μ, whereas the neutron decays in a less energetic proton after 15 minutes.

In other words, the requirement is that the collision can happen only if the relative Lorentz factor of the proton γ is large in such a way that $\epsilon_{\gamma p} \sim 2\gamma \langle \epsilon_{CMB} \rangle$ which can be obtained considering that in the CR reference frame, the energy of the photon is given by:

$$\epsilon = \gamma \langle \epsilon_{CMB} \rangle (1 + \frac{v}{c} \cos\theta) \tag{23}$$

Thus, assuming that the proton moves at $v \approx c$ and the interaction angle is $\cos\theta = 1$, γ must be a least 1.7×10^{11} (or $E = 1.7 \times 10^{20}$ eV) in order to satisfy the requirement $\epsilon \geq \epsilon_{\gamma p} \approx 200\,\text{MeV}$. Actually, we should integrate over the entire CMB spectrum and over all angles. Therefore, the threshold for the photo-pion production process decreases to $E_c \approx 5 \times 10^{19}$ eV, which falls within the energy range observed for UHECRs.

Considering that the number density of CMB photons is $N_\gamma \approx 500/\text{cm}^3 = 5 \times 10^8/\text{m}^3$ and the cross section $\sigma_{\pi p} = 2.5 \times 10^{-32}\,\text{m}^{-2}$, we can define the *mean free path* for a single scattering as $\lambda = \frac{1}{\sigma_{\pi p} N_\gamma} \approx 10^{23}$ m which correspond to a propagation length of ≈ 3 Mpc or, in terms of time, to 10^7 years. When a pion is created, this event produces an energy of $\gamma\, m_\pi c^2$ from which we obtain the fractional energy loss of the cosmic proton: $\Delta E_{\gamma p}/E \approx m_\pi/m_p \sim 1/10$. This means that after 10 collisions, the maximum propagation length for a cosmic proton is:

$$l_{p\gamma} = \frac{1}{\langle y\, \sigma_{p\gamma}\, N_{p\gamma} \rangle} = 30\,\text{Mpc} \tag{24}$$

where $y = \frac{E - E'}{E}$ represents the energy lost at each interaction, $N_{p\gamma}$ is the photon number density and $\sigma_{p\gamma}$ is the cross-section integrated over the momentum distribution of photons. This corresponds to a travel time of $\Delta t \sim l_{p\gamma}/c \sim 10^8$ years. In other words, cosmic protons with energies higher than 10^{19} eV cannot originate from further than ~ 30 Mpc from our Galaxy, thus there should be a drop of observed events for energies higher than 5×10^{19} eV.

This constitutes the drop in the energy distribution called **GZK cut-off**, named after Greisen, Kuzmin and Zatsepin, whose existence depends upon the value of γ of the cosmic rays.

– *electron-positron production* described by:

$$p + \gamma \rightarrow p + e^+ e^- \tag{25}$$

Similarly to the previous mechanism, we can define the critical energy for protons that enable the e^+/e^- pair production at $E_c = 1.02$ MeV, implying that this reaction is possible if the cosmic protons have $\gamma \geq 10^9$ which corresponds to an energy of 10^{18} eV.

Those three effects that affects the energy loss of protons are summarized in the plot below.

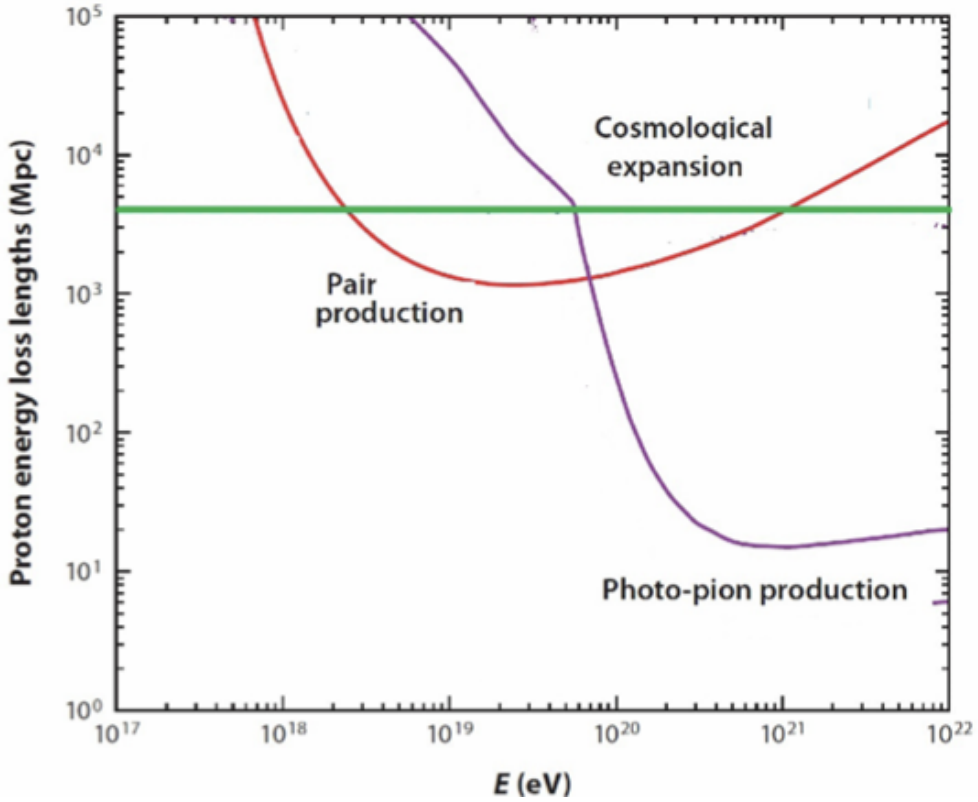

Figure 12: The energy loss lengths for high energy proton propagating through the CMB [2]

Figure 12 compares the relative contributions of the three processes in the case of UHECR protons as a function of energy. We can see that the pair production is dominant below $\sim 10^{18}$ eV: in fact, for this process the cross-section is $\sigma_{pair} = 10^{-30}\,\mathrm{m}^{-2}$, 40 times larger than the one for photo-pion production ($\sigma_{p\gamma} = 2.5 \times 10^{-32}\,\mathrm{m}^{-2}$), thus, each photo-pair production removes only 10^{-3} of the energy of the proton and so the timescale to lose energy is $\Delta t = 2.5 \times 10^9$ years, 25 times longer than the pion production case.

For what concerns heavy nuclei, such as Iron, the GZK cut-off occurs at energies well beyond 10^{19} eV: for a given energy, the Lorentz factor is defined as $\gamma = \frac{E}{Am_pc^2}$, with A the atomic mass number, meaning that the heavier the nucleus, the lower the Lorentz factor. Since the photo-pion production requires that CMB photons are boosted by $\gamma \geq 10^{11}$ to satisfy the energy $\epsilon_r \approx 200$ MeV, nuclei with large A have a GZK cut off shifted by $\sim A$ and a similar effect shifts the e^+/e^- production effect to higher energies.
Moreover, heavy nuclei undergo other energy loss mechanisms such as photodisintegration, due to the interaction of a heavy nuclei with a CMB or EBL photon which provide enough energy to break the bond between the nucleons, according to:

$$A + \gamma \rightarrow (A-1) + N \tag{26}$$

where A is the mass number of the nucleus and N is the nucleon.
This process can change the chemical composition of cosmic rays and causes energy losses per nucleons. The plot below, taken from Biteau [8] shows the energy loss length of nuclei of Hydrogen, Helium, Nitrogen and Iron as a function of energy: in general, the higher the energy of the particle, the shorter the allowed covered distance, and depending on the atomic mass number several energy loss mechanisms can affect the energy loss length.

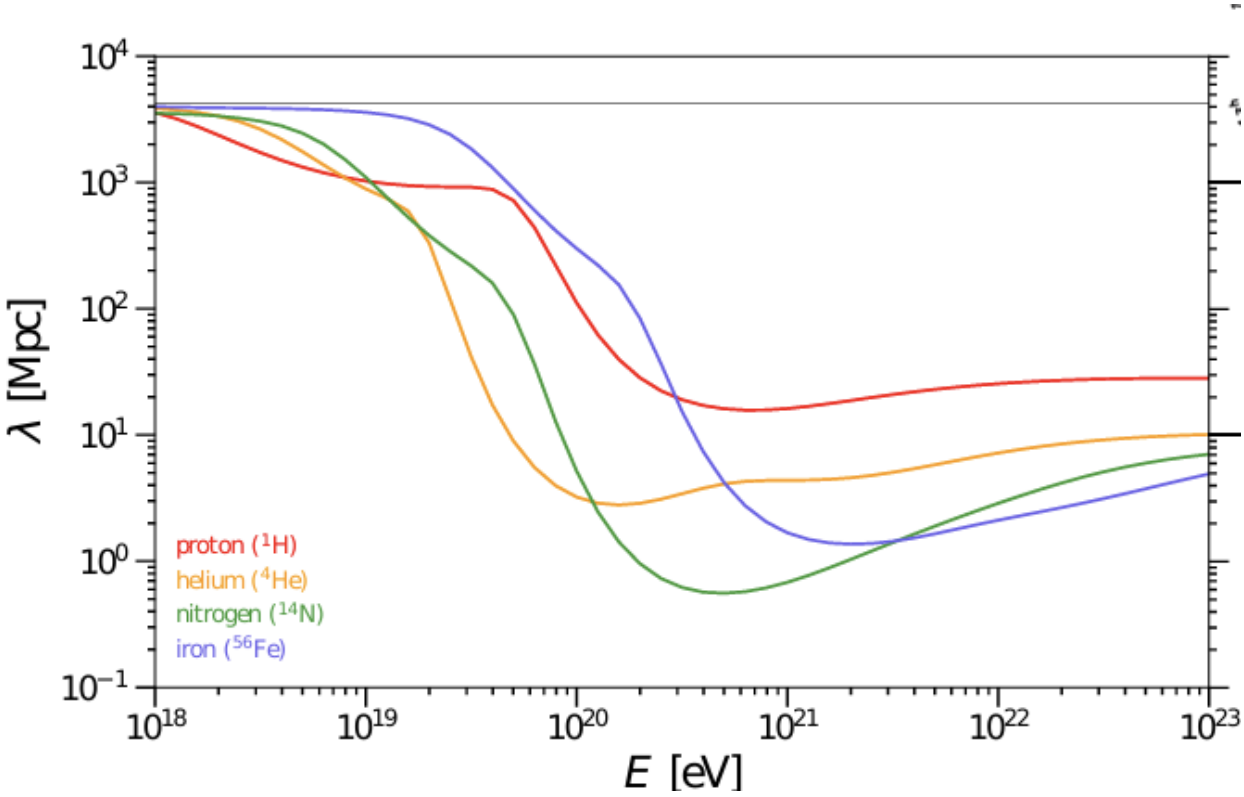

Figure 13: Energy loss length of nuclei of hydrogen, helium, nitrogen and iron as a function of energy Biteau [8]

2 Methods

The aim of my Thesis project is to explore the propagation of Ultra High Energy Cosmic Rays (UHECRs), using state-of-the-art cosmological simulations of extragalactic magnetism (Sec.2.1) and simulating the propagation of UHECRs with a new algorithm, used for the first time in this Thesis (Sec.2.2).

2.1 ENZO Cosmological Simulations

I used a set of newly produced cosmological magneto-hydrodynamical simulations using ENZO [1], designed to investigate the injection and evolution of cosmic rays and magnetic fields by different mechanisms operating in the cosmic web.

In detail, the simulation I analyzed covers a comoving volume of $(42.5\ \mathrm{Mpc})^3$ with a static grid of 1024^3 cells, giving a constant spatial resolution of 41.5 kpc/cell and a constant mass resolution of $1.01 \times 10^7\ \mathrm{M}_\odot$ per dark matter particle. The run includes equilibrium gas cooling, a "sub-grid" dynamo amplification model at run-time, which allows the estimation of the maximum contribution of a dynamo in low density environments [see e.g. 53], while the treatment of primordial magnetic fields and feedback from galaxy formation processes was chosen from a larger suite of simulations, described in Vazza et al. [52].

2.1.1 Non-gravitational physics

The adopted star formation recipe follows the method by Kravtsov [33], designed to reproduce the observed Kennicutt's law [32] and with free parameters calibrated to reasonably reproduce the integrated star formation history and the stellar mass function of galaxies at $z \leq 2$. The feedback from star forming particles assumes a fixed fraction of energy/momentum/mass ejected per each formed star particles, $E_{SN} = \epsilon_{SF} m_* c^2$, with efficiency calibrated to $\epsilon_{SF} = 10^{-8}$ as in previous work [53]. The simulation also considers that 90% of the feedback energy is released in the thermal form (i.e. hot supernovae-driven winds), distributed the 27 nearest cells around the star particle, and 10% in the form of magnetic energy, assigned to magnetic dipoles by each feedback burst.

The feedback from active galactic nuclei has been implemented by assuming that, at each timestep of the simulation, the highest density peaks in the simulation harbor a supermassive black hole, to which we assign a realistic mass based on observed scaling relation [e.g. 25]. The code computes the instantaneous mass growth rate onto each supermassive black hole by following the standard Bondi–Hoyle formalism, in which there is (as typically for simulations at this resolution) an ad-hoc "boost" parameter meant to compensate for the lack of resolution around the Bondi radius. Depending on the temperature of the accreted gas, the code employs either "cold gas accretion" feedback (in which most of the energy is distributed in the form of thermal energy in the neighborhood of each simulated AGN) or "hot gas accretion" feedback (in which most of the energy is released in the form of bipolar kinetic jets). In both cases, the feedback routine releases 10% of the feedback energy in the form of magnetic energy, through pairs of magnetized loops wrapped around the direction of kinetic jets. This magnetic field is added to the simulation, leading to "magnetic bubbles" correlated with halos in the simulated volume. A more detailed description of all parameters used in this and in the other model variations of the entire suite of cosmological simulations is given in Vazza et al. [52].

2.1.2 The extragalactic magnetic field model

The simulation I analyzed was calibrated to reproduce several key observables of the galaxy distribution, which can used to predict the maximal magnetization by feedback processes (by AGN and star formation) in a realistic way. This simulation has been selected because it yields the best comparison with recent LOFAR observations of the Residual Rotation Measure (RRM) as a function of redshift, $\mathrm{R}RM(z)$, as in Carretti et al. [15] and in Carretti and Vazza [16]. These works showed that no purely astrophysical magnetization mechanism can, alone, account for the observed RRM rms for $z \geq 1$.

The magnetic field in this simulation (taken from a larger suite of runs) is predominantly primordial, but also a realistic astrophysical contribution is considered, as a result of galaxy formation-related processes. The stochastic primordial initialization of the magnetic field is obtained by drawing magnetic field vectors

[1] enzo-project.org

from a power-law spectrum: $P_B(k) = P_{B0}k^{-1}$, and with a normalization set to $(\langle B^2 \rangle)^{0.5} \approx 0.37\,\mathrm{nG}$ after smoothing the field to a physical scale of 1 Mpc (comoving), as usually done in CMB analysis [e.g. 42]. The initial normalization of $(\langle B^2 \rangle)^{0.5} \approx 0.37\,\mathrm{nG}$ is ~ 5 times below the existing CMB constraints, and is driven by the recent sensitivity obtained by LOFAR radio observations [e.g. 16].

Figure 14 shows the comparison between the observed trend of the Residual Rotation Measure of polarized background sources located at different redshifts measured using LOFAR [15], and a few model variations in the suite of Enzo cosmological simulations. The model chosen for this Thesis is the one giving an overall best match to the observed $RRM(z)$ at most redshift, while other purely astrophysical seeding scenarios are unable to match the observed trend of $RRM(z)$ at high redshift.

The maps in the next Figure show the projected distribution of dark matter, baryonic matter, baryon temperature and magnetic fields along the line of sight in the simulation at $z = 0$, which I used to simulate the propagation of UHECRs (see next Section). In particular, Fig.10c gives an impression of the 3-dimensional distribution of magnetic fields crossed by UHECRs during their propagation: the magnetic field is not uniformely distribuited, but it tends to follow a clear pattern resembling the cosmic structures (see Fig. 10a). The regions with intense magnetic fields $B \geq 10^{-9}$ G (yellow/orange) are mostly concentrated along filaments and in correspondence of gravitationally bound structures where $\rho \geq 10^{-29}\,\mathrm{g/cm^3}$, such as clusters or groups of galaxies. in fact, these regions represent sites in which the merging processes and turbulence mentioned above can lead to the amplification of the magnetic field. Moreover, inside the haloes several mechanisms due to accretion can enhance the magnetic field value up to $B \gg 10^{-8}$ G. Nevertheless, these regions are highly localized, thus the volume filling is low.
Conversely, the darker patches correspond to the lowest density regions of the Universe, the so-called cosmic voids, where the magnetic field presents extremely low values, below $10^{-9.75}$ G, providing a larger volume filling.

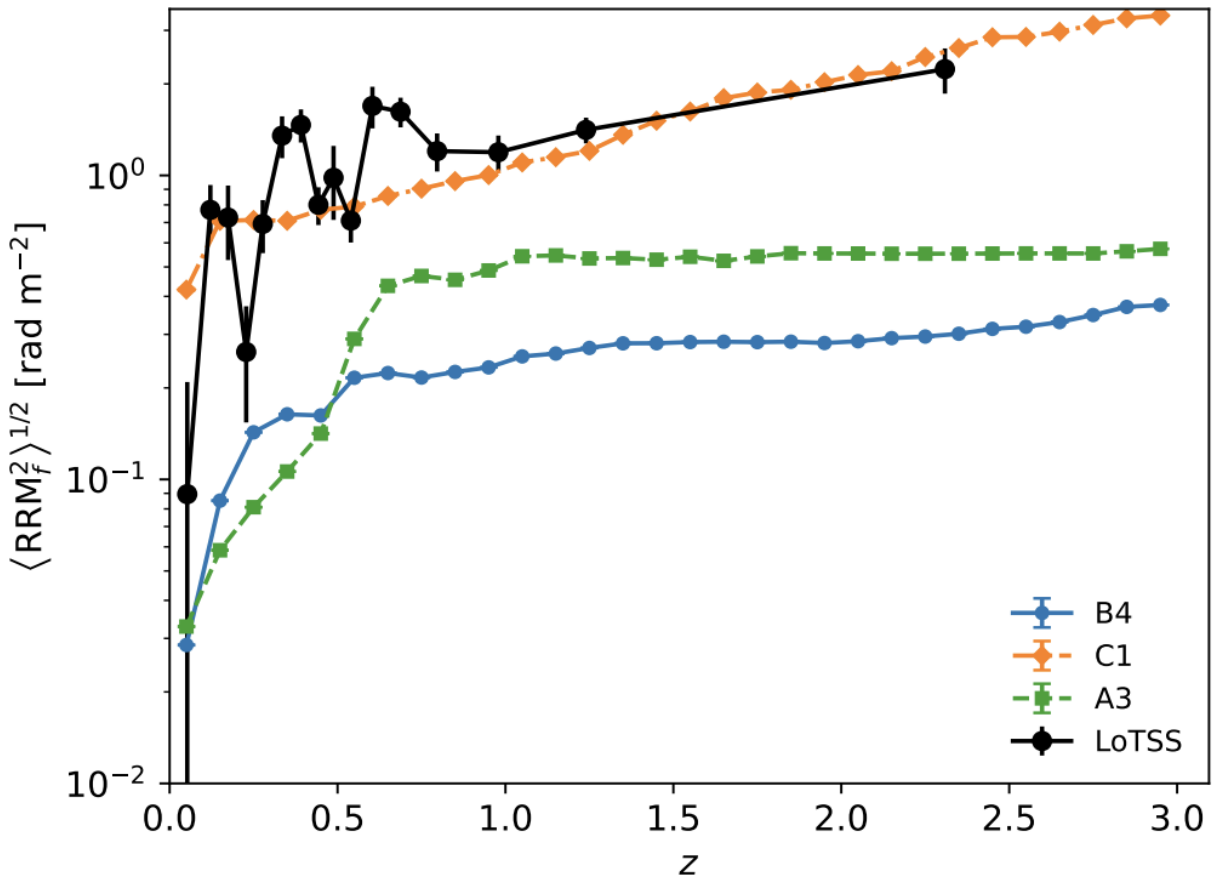

Figure 14: Observed trend of the Residual Rotation Measure of polarized background sources located at different redshifts (black points with errorbars) measured using LOFAR by Carretti et al. [15], and comparison with a few model realization of cosmological MHD simulations (lines with colors). The model chosen for this Thesis is the C1 model, which comprise a combination of primordial and astrophysical sources of magnetic fields. The other two models shown here only contain variations of astrophysical seeding scenarios of magnetic fields, and are unable to match the observed trend of $RRM(z)$ from sources at high redshift (see Vazza et al. 52 for more details).

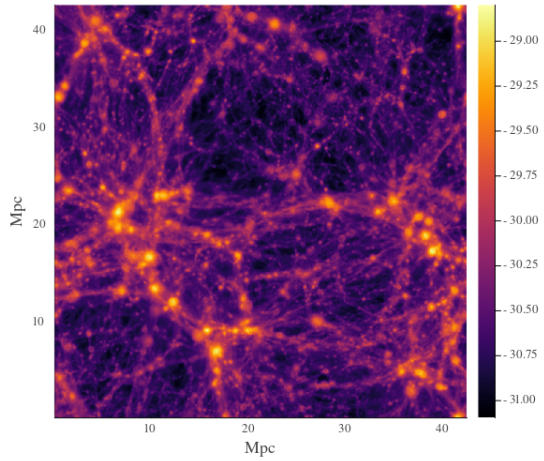

10a: Projection of baryonic density [g/cm^3] in logarithmic scale

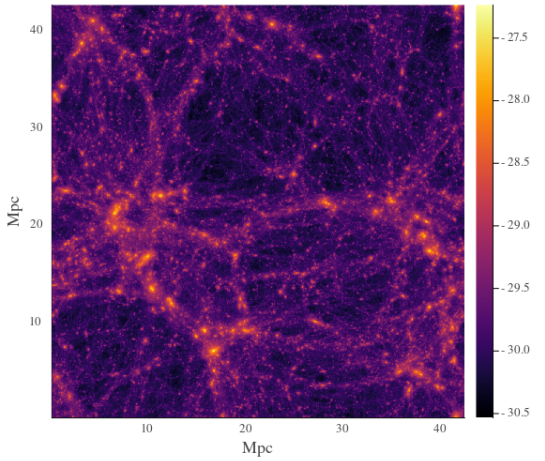

10b: Projection of Dark Matter density [g/cm^3] in logarithmic scale

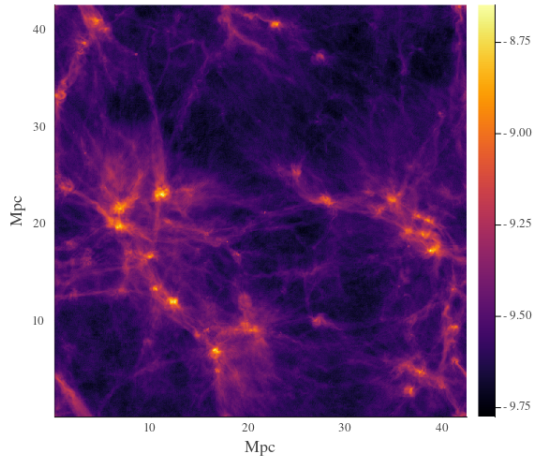

10c: Projection of magnetic field [G] in logarithmic scale

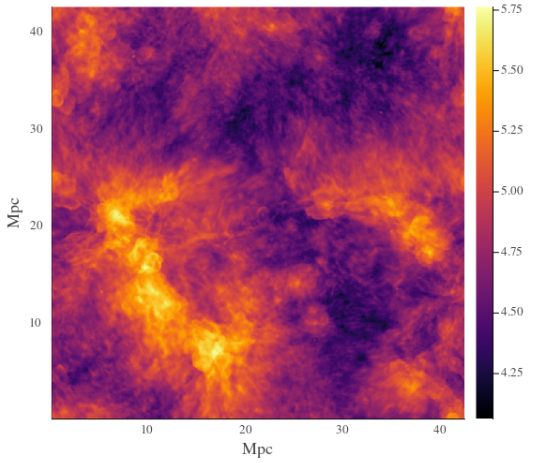

10d: Projection of temperature [K] in logarithmic scale

2.2 UMAREL

The analysis of propagation of UHECRs starts with the injection of particles into the simulated volume described in Sec. 2.1. This is done by the julia-based numerical code UMAREL [2], which injects large sets of cosmic rays in the simulated volume, and it self-consistently evolves their spatial evolution and energy evolution in time [3].

Other codes, also public ones, have been developed in the recent past to simulate the propagation of cosmic rays, both in the extragalactic or galactic context, like CRPropa [37], CRbeam [31], DRAGON [23], to name a few. However, for the somewhat limited physical complexity related to this first cursory study of UHECR proton propagation in the magnetized Universe, it appeared much more efficient to develop an in-house numerical code, which ensures more flexibility and capabilities of customisation for our scientific

[2]Ultra high energy cosmic rays in Magnetic fields Affected by Rigidity and Energy Losses
[3]https://github.com/FrancoVazza/UMAREL

needs.

In the standard setup, cosmic rays in UMAREL are injected only above large values of matter density, corresponding to the innermost regions of massive halos ($\geq 10^{11} M_{\odot}$) in order to mimic a plausible scenario in which energetic events within galaxies originate UHECRs.

The population of particles can be selected among Protons, Helium, Iron and Nitrogen, with initial random velocity vectors (in all cases assuming $|\vec{v}| = c$) and initial energy randomly chosen in the range $10^{17} - 10^{22}$ eV. The random energy is selected uniformly in log(E) space, which is equivalent to generating a $N(E) \propto E^{-1}$ initial spectrum. This spectrum is much flatter than the spectrum of observed UHECRs, and the reason to choose this slope is to generate a fair amount of trajectories for UHECRs both at the low and high-end energy of the spectrum, across 4 orders of magnitude. In a procedure explained in Sec.5, we can appropriately weight in post-processing the simulated statistics of UHECR propagation based on their energy, so that we can approximately mimic the behaviour of a more realistic $N(E) \propto E^{-2}$ injection spectrum.

The investigation of the 3D evolution of those cosmic rays is based on the **Boris Pusher** method (Decyk et al. [19]), an algorithm which solves the relativistic equations of motion for charges under the action of the Lorentz force:

$$\frac{d(m\gamma\vec{v})}{dt} = q\,[\,\vec{E} + \vec{v} \times \frac{\vec{B}}{c}\,] \tag{27}$$

The algorithm implemented in UMAREL works under periodic boundary conditions and assumes protons moving at $|\,\vec{v}\,| = c$, under the influence of the magnetic field. The algorithm follows the *kick-drift-kick* integration scheme, commonly used in charged particle dynamics to ensure numerical stability and conservation of motion.
The procedure for each timestep is structured in this way:

- **kick** (first half-step): the particle velocity is updated by half a timestep, under the influence of the Lorentz force according to:

$$\vec{v}^{(1/2)} = \vec{v}_i^{(0)} + \frac{1}{2}\Delta t \Delta \vec{v} \tag{28}$$

  The conservation of the velocity module is ensured by rescaling the velocity vector:

$$\vec{v}^{(1/2)} = \vec{v}^{(1/2)} \cdot \sqrt{\frac{|\vec{v}^{(0)}|^2}{|\vec{v}^{(1/2)}|^2}} \tag{29}$$

- **drift**: the particle position is changed over a full timestep using the updated velocity:

$$\vec{x}^{(1)} = \vec{x}^{(0)} + \frac{\vec{v}^{(1/2)}\,\Delta t}{scale} \qquad \text{scale} = dx \cdot 10^{-3} \cdot \text{cmtoMpc} \tag{30}$$

  where in this simulation $dx = 41.5$ kpc represents the resolution of the grid converted in physical units using cmtoMpc $= 3.08 \times 10^{24}$ cm/kpc;

- **kick**: the velocity is updated again due to the action of the Lorentz force, always guaranteeing the $|\vec{v}| = c$:

$$\Delta\vec{v}_2 = \frac{q}{m}\frac{\Delta t}{2}\frac{\vec{v}^{(1)} \times \vec{B}}{c} \tag{31}$$

$$\vec{v}^{(2)} = \vec{v}^{(1)} + \Delta\vec{v}_2 \tag{32}$$

Between one advection timestep and the other, UMAREL computes the effects of energy losses on UHECRs, which in turns affect their spatial evolution by changing (always as a decrease) their Lorentz factor. The energy losses are implemented by using tabulated loss rates curves depending on the particle's charge Z. More precisely, the characteristic timescale for energy losses is defined as:

$$\Delta t_{loss} = \frac{E}{dE/dt} \tag{33}$$

Two update regimes are implemented, depending on the relation between Δt_{loss} and the simulation timestep Δt:

- if $\Delta t_{loss} \gg \Delta t$

$$E^{(1)} = E^{(0)} \cdot (1 - \frac{dE}{dt} \cdot \Delta t) \tag{34}$$

- if instead, $\Delta t_{loss} \ll \Delta t$, the update is iterated over $n = \frac{\Delta t}{\Delta t_{loss}}$ substeps to avoid excessive loss per step;

The energy loss mechanisms considered in the code are the one mentioned in Sec.1.5 and are mainly due to the interaction of the cosmic rays with the photons of the CMB, with a contribution of photons of the Extragalactic Background Light (EBL).
In addition, the amount of energy lost depends on the energy of the particle itself: the higher the energy the more ingent the loss.
The plot below (Fig.11) shows the amount of energy lost based on the energy of the particle and the mechanism responsible for that loss: adiabatic expansion, pair production and pion production.

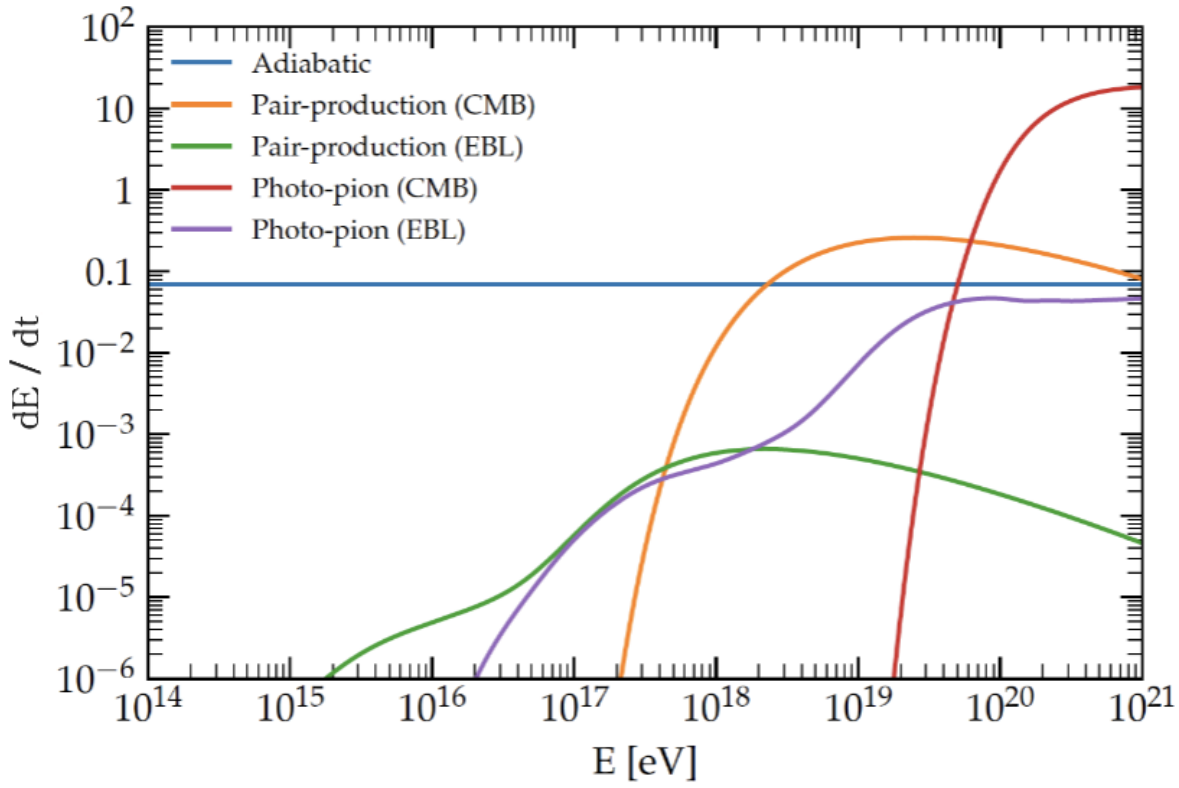

Figure 11: Energy loss rate (in units of dlog(E)/dt [1/Gyr]) as a function of the cosmic ray energy, for the case of protons, as is tabulated in the numerical code used for this Thesis (Sec.2.2). Different colors show the relative impact of the different loss mechanisms.

2.2.1 Testing the code: numerical effects

UMAREL has been developed and applied for the first time to produce the results of this Thesis, and therefore I devoted a significant amount of time to produce benchmark and various convergence tests to ensure that the algorithm was properly working, and also to tune some of UMAREL's internal parameters. For instance, the choice of the timestep Δt plays a crucial role in guaranteeing the stability and the accuracy during the computation. In this regard, the Courant-Friedrichs-Lewy condition (CFL) has been applied in order to ensure the numerical convergence of the solutions based on the grid resolution Δx and the particle velocity v.

$$\text{CFL} = \frac{v\Delta t}{\Delta x} \tag{35}$$

More specifically, the timestep is defined as dt = CFL ∗ scale/vc, where the scale = dx · 10^{-3} · cmtoMpc, with grid resolution dx = 41.5 kpc, particle velocity vc =$c \sim 3 \times 10^{10}$ cm/s and CFL = 3.0 which provides a dt ≈ 1.27×10^{13} s that correspond to almost 0.5 million years.
Before settling on this value, I performed several tests: the reasons why a lower number has not been taken into account are purely related to compiling time limitations, since a lower CFL number would have required a large number of iterations without a tangible improvement in the accuracy.

In the remainder of my Thesis, the average distance covered by UHECRs as a function of time is one of the main diagnostics that I will study to monitor the effect of intergalactic magnetic fields. Therefore, here I discuss the effects of the CFL directly on this quantity. The plot below, obtained with `mag_hor` (Sec.5)[4], shows the distance travelled with respect to the injection site, by a population of 10^2 protons with initial energy 10^{19} eV. The three curves indicate that a too large CFL number, such as 9, for simulations that involve a long evolution is not a good choice as it leads to underestimates of the true distance covered by cosmic rays, and it does not converge to the result of runs with a better time resolution. In contrast, small CFL number and small timesteps allows to reach a better accuracy. Since the curves obtained with CLF = 1, 3 are perfectly overlapped, I opted for CFL = 3, as it permits to save memory [5], computing time *and* to ensure the convergence.

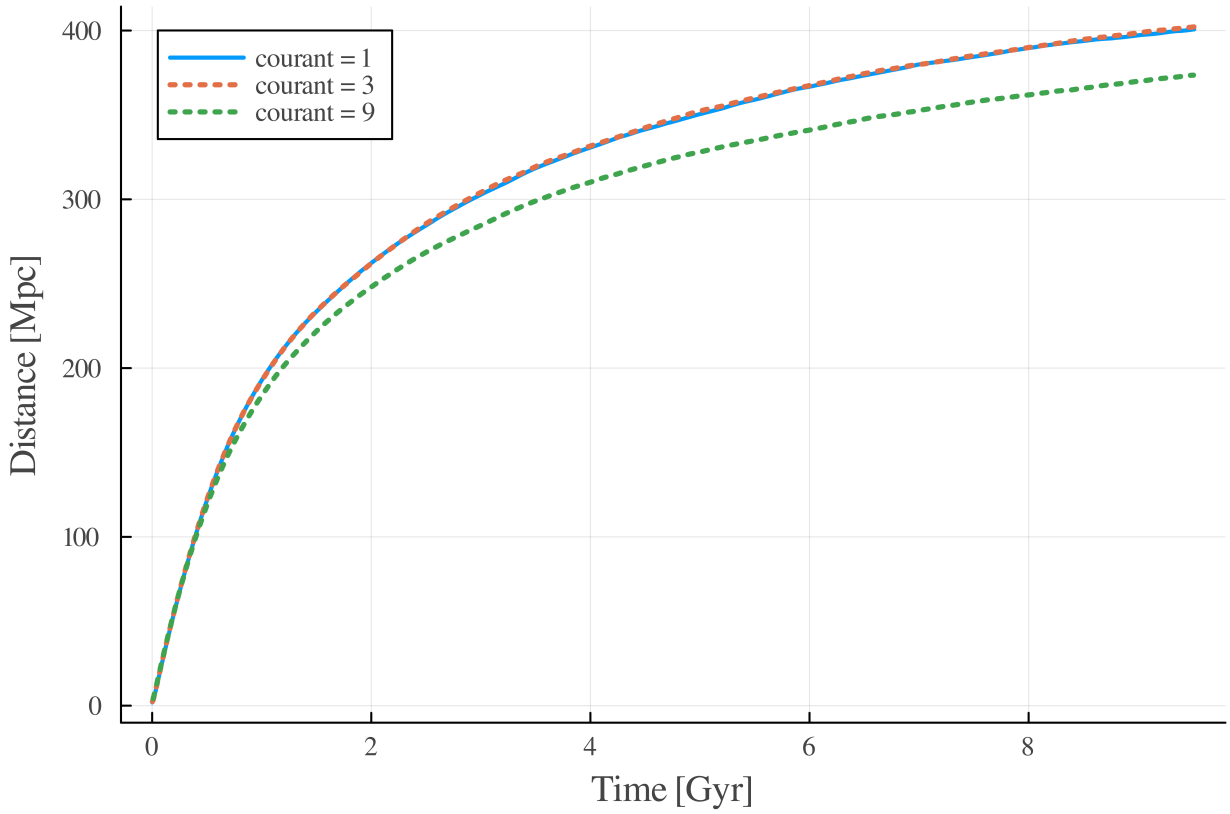

Figure 12: Average distance travelled by particles with initial energy of 10^{19} eV over 10 Gyrs computed with CFL = 1.0, 3.0, 9.0

Next, I studied how the UHECRs trajectories depend on the randomness in the initial set up by running several simulations where all the physical parameters (energy, density field and magnetic field) were kept the same, whereas the random seed responsible for the starting position and direction of each cosmic ray was

[4]See the following section and the appendix for more details

[5]It should be noticed that saving timesteps does indeed produce a saving in memory, and not only in computing time, because in the analysis performed in my Thesis the full trajectories of cosmic rays have to be recorded and analysed in post-processing (see next Sections). Hence a reconstruction of the same trajectories with fewer timesteps also produce a proportionally smaller amount of data to store and process after each UMAREL simulation.

varied.
It is important to highlight that, as previously mentioned, the UMAREL code injects particles only in cells with densities higher than a threshold, which are kept the same for this run. However, inside each cell the injection site and the direction of motion are random.

Therefore, this test helps answer whether the initial positions and direction of motion can impact on the average distance travelled by UHECRs. The plot below (Fig.13) shows the distance travelled by 100 protons with initial energy 10^{19} eV, for four different initial random injections. The small variance computed at all epochs, up to 10 Gyrs of evolution, convincingly shows that random variations of the initial injection positions and initial velocities does not affect the covered distance in any significant way, and hence in the rest of the Thesis single generation of UHECRs with one single random injection are sufficient to measure all important trends.

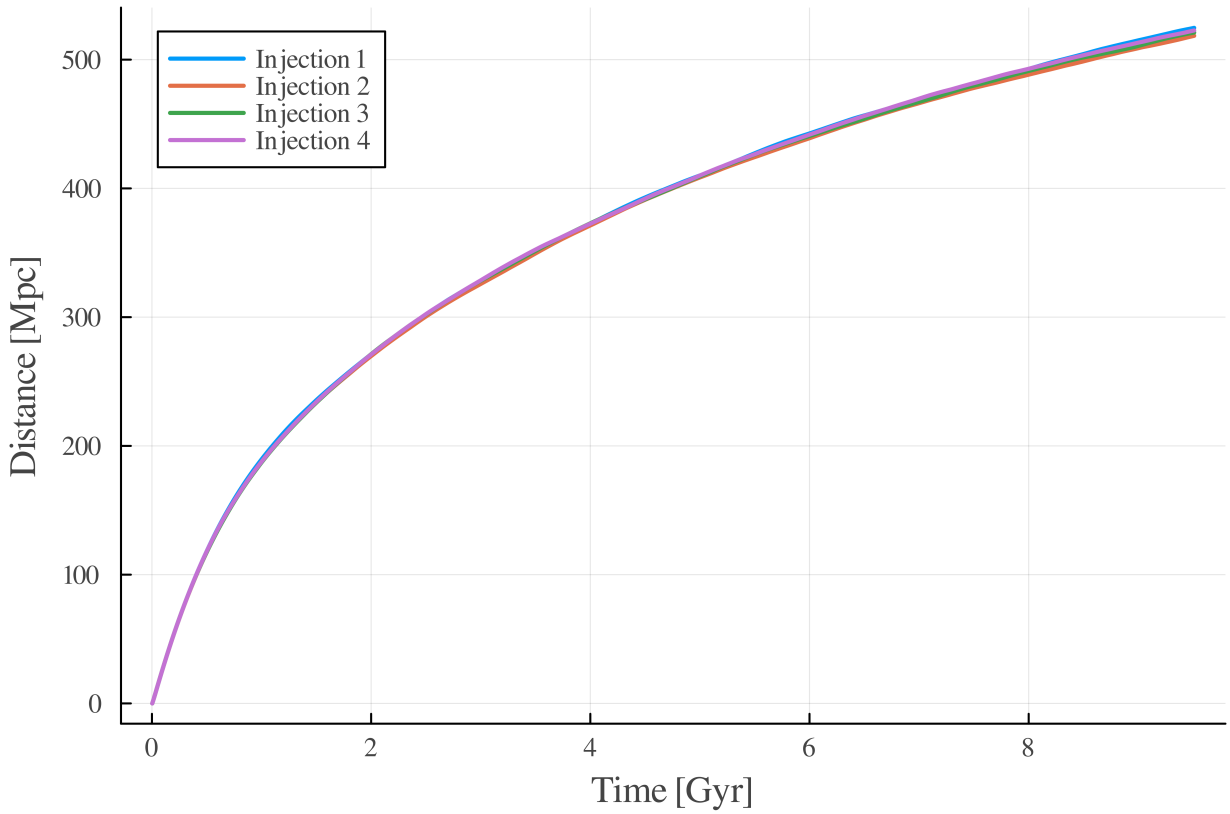

Figure 13: Comparison between different randomly chosen injection site of a population of 100 protons with initial energy of 10^{19} eV.

2.2.2 Testing the code: physical effects

Once the time-step has been set, it was necessary to test the physical validity of UMAREL by exploring different environmental setups; as already displayed in sections 1.4 and 1.5, the propagation of cosmic rays is strongly affected by the presence of the magnetic field and the energy loss mechanisms. For this purpose, three different scenarios have been developed and compared with each other:

1. **no field model**, an environment with a negligible magnetic field, where particles' propagation is only influenced by the energy loss processes;

2. **no losses model**, a magnetized environment where particles do not suffer energy losses, and the propagation is only affected by the presence of the magnetic field;

3. **fiducial model**, a realistic environment, in which the energy losses and the magnetic field are both taken into account;

Firstly, 93501 protons ($Z = 1$) were injected from various haloes with an initial energy randomly chosen in the range $10^{17} - 10^{21}$ eV in a volume of 700^3 cells.
Subsequently, UMAREL provides a map representing the initial location of CRs (Fig.14a) and a file encoding, for each particle, the information about their position (x, y, z) and energy at each timestep (see Fig.14b), covering 10 Gyr evolution.

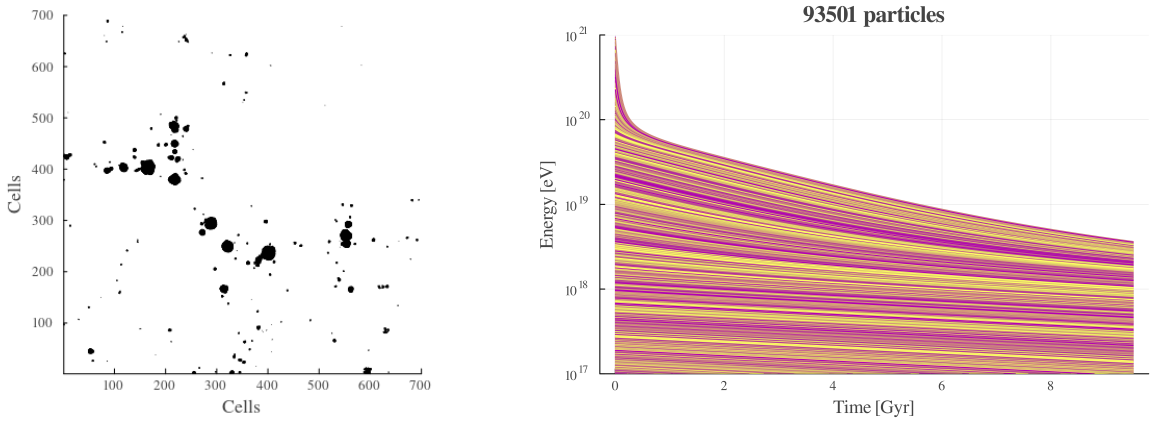

14a **14b**

Figure 14: On the left the map representing the initial location of CRs in terms of cells. The dark spots indicate the haloes from which UHECRs are injected. On the right, the energy evolution for each proton from the initial energy at the injection time to the end of the simulation

For this investigation, I developed two julia-based codes : `mag_hor` (Sec.5) and `arrival_energy` (Sec.5), both of them using the 3D evolution of the protons provided by UMAREL. The first one groups the particles depending on their *initial energy* and computes the distance travelled with respect to the injection position covering a time interval of 10 Gyr.
Instead, the second one searches for the timestep at which a particle reaches a certain energy value, representing the *arrival energy* at which the particle is detected, in order to reconstruct the path of the proton from the injection until the time of detection. Then, for each arrival energy, I computed the fraction of Cosmic Rays able to cover a certain distance.
These two algorithms were used in all three scenarios mentioned above, in order to better quantify the effect of the losses and the magnetic field, which are explained in the following sections.

Testing the impact of magnetic fields

The first analysis is to test the impact of the magnetic field: to this end, in this section we are going to compare the realistic scenario, in which protons propagate in the magnetized medium, presented in Sec.2.1.2, with a model where the field is set to a negligible value ($B = 10^{-20}$ G). In both cases, the energy loss mechanisms due to the adiabatic expansion, pair and pion production, described in Sec.1.5, are considered. The UMAREL code provides the following propagation maps in the two cases that allow us to have a first look on the scales covered during the propagation.

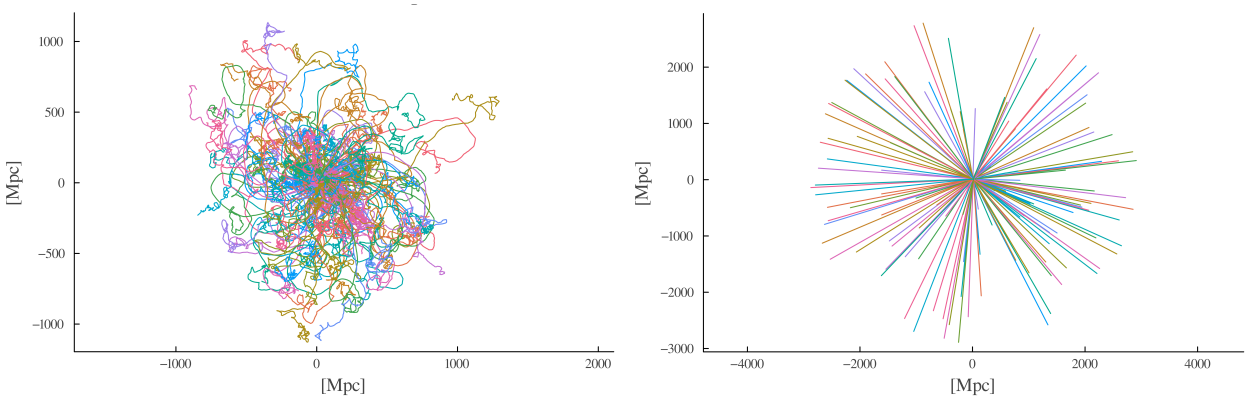

15a: Fiducial model

15b: Non-magnetized environment

Figure 15: On the left, a representation of the path travelled by protons affected by energy losses in a magnetized medium; on the right the same protons are injected in a negligible magnetic field: notice the different length scale representing the distance covered

As we can see, the ensemble of trajectories in Fig. 15a covers a smaller projected area if compared with Fig. 15b and this can be explained referring to sections 1.4.1 and 1.4.2: in a non magnetized environment, as the one in Fig.15b, the path travelled by the particle well represents a **ballistic propagation**, where the trajectories are straight lines. Conversely, if we consider the presence of the field (Fig.15a), the motion of the particle is strictly connected to the intensity of the magnetic field which makes the protons drift and travel complicated trajectories based on their **Larmor radius** $r_L \propto E/ZB$. This means that, without a magnetic field, protons are able to travel longer distances than in a magnetized medium, in which the propagation depends on the **rigidity** of the particle $R = \frac{E}{Ze}$.
Therefore, in order to quantify the effect of the magnetic field, I used the `mag_hor` code mentioned above (Sec.5). I grouped the particles depending on three initial energy bins (10^{18} , 10^{19} and 10^{20} eV), then for each of them, I have computed their distance with respect to the injection site, averaging over the selected sample of protons. The algorithm produces the following plot, which displays the same population of protons according to the **fiducial** and the **non magnetized** model.

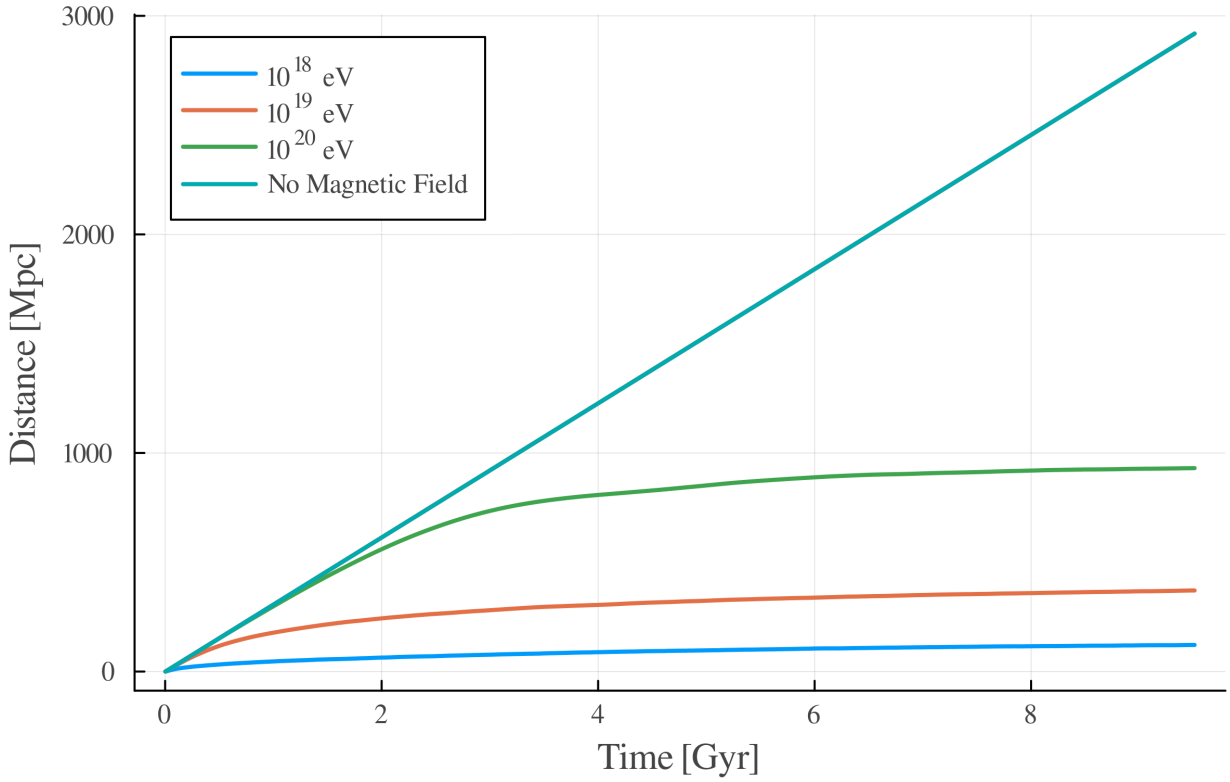

Figure 16: Average distance over time covered by UHECRs with an initial energy randomly chosen between 10^{18}, 10^{19} and 10^{20} eV at injection.

The straight line represents the ballistic propagation in a non-magnetized medium and we can notice how the distance is independent from the energy of the particle, since all the protons move at the speed of light, according to $d = c \cdot t$. On the other hand, adding the magnetic field allows us to distinguish the path based on the initial energy of the particle, due to the effect of the **rigidity** $\mathrm{R} \propto E/Z$: protons with initial energy 10^{20} eV have a higher resistance against the magnetic field, therefore after few Gyrs they are able to cover the same distance as in the non-magnetized case. In contrast, low energy particles are more affected by the magnetic field, thus, at a fixed time interval, low energy protons travel a shorter distance than the high energy ones.

Another useful test is to recreate a detection event implementing another julia code, `arrival_energy` (see Sec.5). At these energy ranges, the observed spectrum behaves as $E^{-3.1}$ and considering the energy losses presented in Sec.1.5, it is compatible to an **injection spectrum** that follows the E^{-2} trend, as the ones of strong shock acceleration, Fermi and so on.
However, such a high steepness would require an extremely low statistic at these high energy regimes: for instance, at 10^{17} eV, we expect to detect 10^6 events, whereas at 10^{20} eV only 1 event.
Thus, in order to overcome the low statistic problem, as literature suggests, the injection spectrum is built to behave as E^{-1} and is constructed in such a way that, every 1000 particles with initial energy of 10^{17} eV corresponds 1 particle with initial energy of 10^{20} eV.
Then, a further weighing of E^{-1} is applied to the energy data allowing us to obtain realistic weighed averages for the cosmic rays sample and to avoid the low number statistic problem for the high energy protons.

Again, using the positions and energy data supplied by UMAREL, for both the non magnetized and fiducial case, I selected different energy bins ($10^{17}, 10^{18}, 10^{19}$ and 10^{20} eV) representing the *arrival energy* of the cosmic ray on Earth, and, for each particle, I have extracted the timestep at which the specific energy bin is reached. This moment is assumed to correspond to the detection time, that is used to trace the trajectory from the beginning of the simulation up to the instant at which the cosmic ray hits the Earth. Subsequently, I have computed the fraction of protons arriving with a specific energy that succeeded in reaching a certain

distance for all possible epochs in the simulation.
This procedure allows us to reconstruct the propagation history of particles that are detectable at Earth with a given energy, as well as to identify characteristic propagation scales.

To have a better visualisation of this procedure, Fig.17 shows a decreasing trend of the fraction of CRs with respect to the distance: the farther the distance the fewer particles can reach it. The solid curves represent the fiducial case, whereas the dotted ones describe the propagation scenario in which there is no magnetic field.

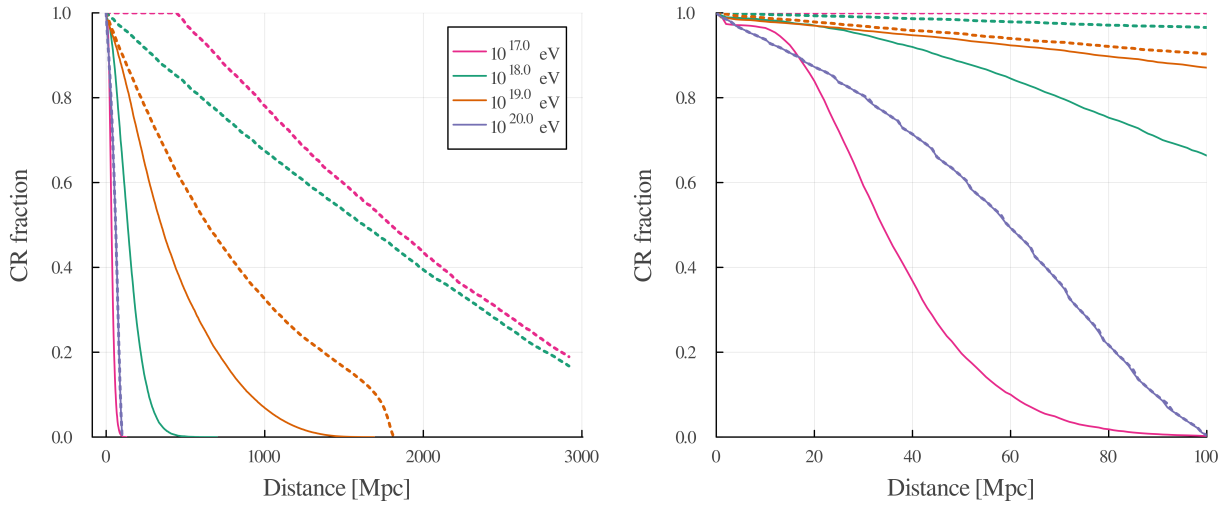

Figure 17: Comparison between the fraction of protons arriving with certain energies and their corresponding hypothetical travelled distance in the fiducial case (solid curves) and in the no magnetic field model (dotted curves)

Fig. 17 clearly shows that the particles with an arrival energy of 10^{20} eV cover the same distance in both models, as shown by the two perfectly overimposed curves. On the other hand, protons detected at lower energies have crossed a significantly lower distance in the magnetized environment than in the no field case, in which they are only affected by the energy losses. This discrepancy decreases as the arrival energy increases since the effect of the rigidity on the particle becomes more and more relevant, meaning that in a magnetic field the energetic protons are able to travel more easily than low energy particles.

Testing the effects of energy losses

Now, we investigate how the energy loss mechanism can affect the propagation of protons: thus, we are going to compare the fiducial case with a model in which losses are not taken into account and the only present effect is the one of the magnetic field. This means that the interaction with the CMB and EBL photons does not cause a loss of energy, which is maintained constant from the time of the injection until the end of the simulation.
For this study, a crucial result that must be taken as a reference is the one already shown in Fig. 11, which describes how the amount of energy lost depends on the current energy of the particle and the dominating energy loss mechanism. The effect related to the loss mechanisms can be visualized in the color maps produced by UMAREL. When ignoring losses, the trajectories are deflected since the magnetic field is still present, but the tracks are not so tangled as in the fiducial model, actually they cover a wider area. This is due to the fact that the omission of the losses is in turn reflected in the rigidity term: if a particle does not lose its energy, then the rigidity can maintain higher values; therefore the proton will have a better resistance against the magnetic field and will be able to cover larger distances.

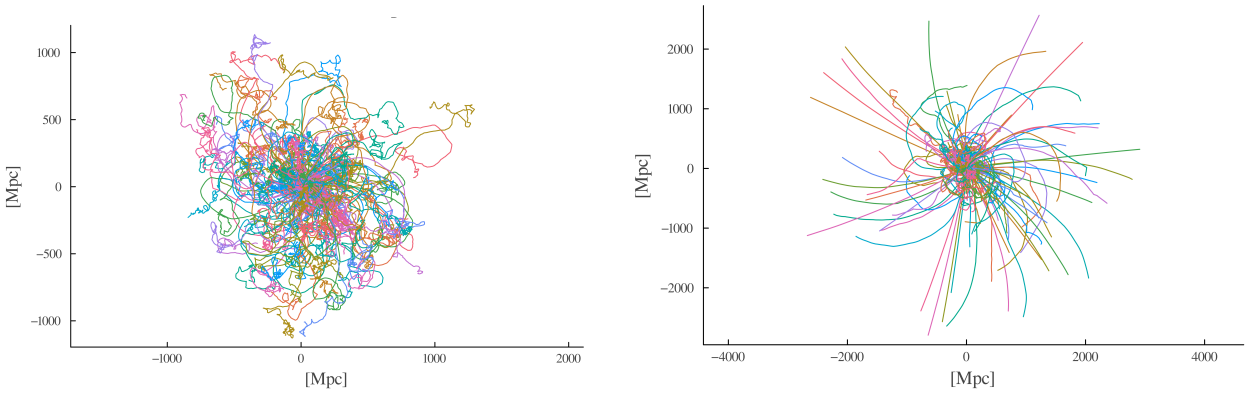

Figure 18: On the left the color map of protons affected by losses in a magnetized medium; on the right the color map of protons not affected by losses moving in a non-magnetized environment. Notice the different length scale covered

Similarly to the previous section, in order to better quantify the differences between the two models, I studied the length of the particles' trajectories. With the `mag_hor` code, I grouped the particles depending on their initial energies ($10^{18}, 10^{19}, 10^{20}$ eV) and computed the travelled distance with respect to the injection site. The plot below shows a comparison between the fiducial model (solid curves), which takes into account both the effect of the losses and the magnetic field, with the model without the losses (dotted curves).

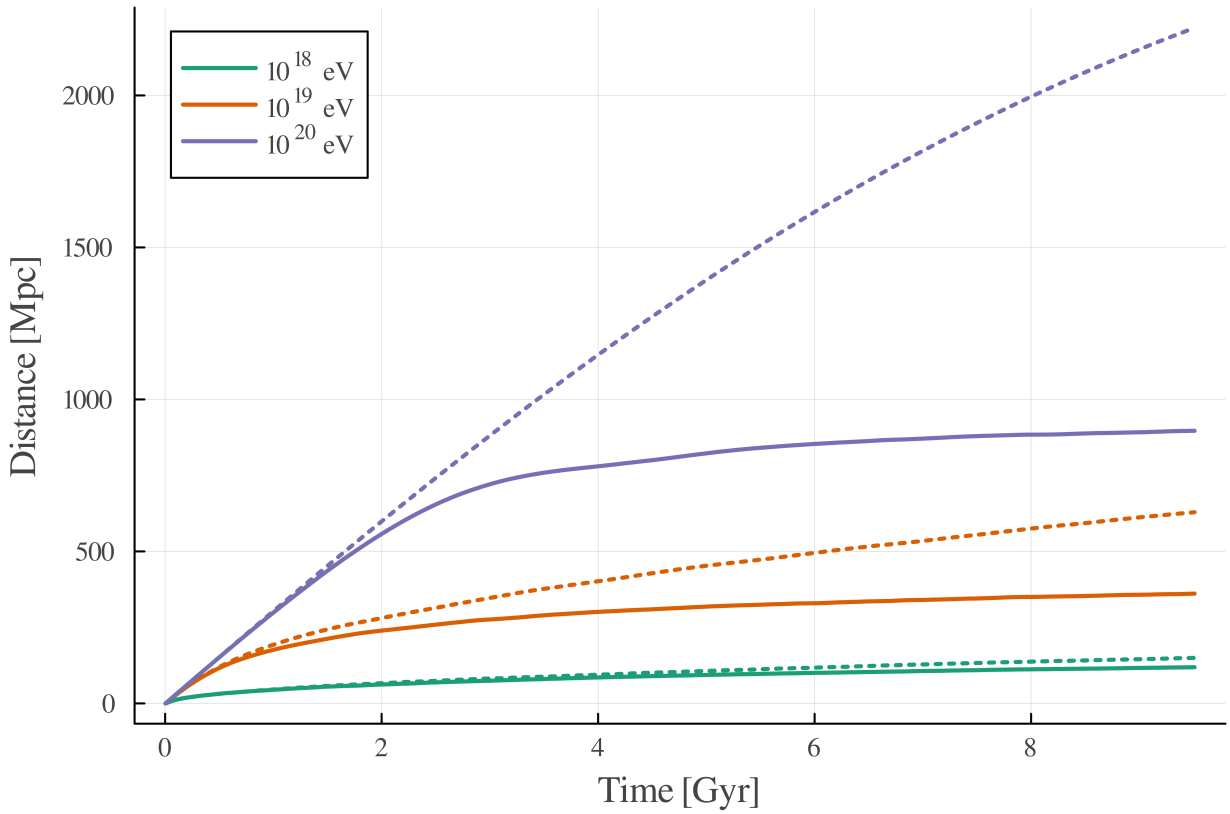

Figure 19: Average distance over time covered by UHECRs with an initial energy randomly chosen between $10^{18}, 10^{19}$ and 10^{20} eV at injection. The solid lines represent the propagation in the fiducial model, whereas the dotted ones the propagation in the no losses model

Fig. 19 demonstrates how the variation of energy can impact on the travelled distance: when a particle

is injected with low energies, such as 10^{17} eV the length of the path is not so different in the two models, whereas the discrepancy becomes more relevant at higher energies. In fact, as already show in Fig.11, the more energetic the particle the larger the amount of energy lost at a specific time step and viceversa for the low energy protons. This mechanism affects the already introduced capability of the particle in moving through a magnetised environment, the rigidity: this explains why ignoring the losses allows energetic particles to move further, whilst the less energetic ones manage to travel distances that are similar in the two models.

Also in this case we reproduce the detection event from Earth, employing the `arrival_energy` algorithm. This procedure allows us to track the evolution of each particle's energy throughout the simulation and to determine the specific moment at which the arrival energy is reached. Once having obtained the timestep at which the arrival energy is reached, I determined the corresponding distance travelled from the beginning of the simulation to the moment of detection. With these informations, I calculated the fraction of CRs arriving at a certain energy that could have covered a given distance before reaching the observer. This approach allows us to quantify how energy loss mechanism can impact on the maximum length covered by the particle. As shown in the previous analysis, the percentage of particles arriving at specific energies, progressively decreases with distance.
As reported in Fig. 20, the solid curves represent the possible distances travelled by a fraction of protons observed at certain energies, affected by losses, whereas the dotted ones represent the same population of particles without the influence of losses. For instance, the 50% of protons observed arriving with energy 10^{20} eV that have lost energy during their propagation, could have travelled few Mpc, but if they maintain their energy constant, then the covered distance increases of several thousands of Mpc.

On the other hand, if we detect a proton with energy of 10^{17} eV, the distances covered in the two models are comparable. This different behaviour is explained using Fig.11: suppose to observe a cosmic ray arriving with energy 10^{17} eV; if its injection energy was 10^{20} eV, then during the first phases of its propagation, the interactions with CMB and EBL photons would have caused significant energy losses, but as the energy decreased, the reduction of energy progressively becomes less ingent. This explains why the discrepancy in the two scenarios is less evident for low energy particles, whereas is striking in the high energy regimes.

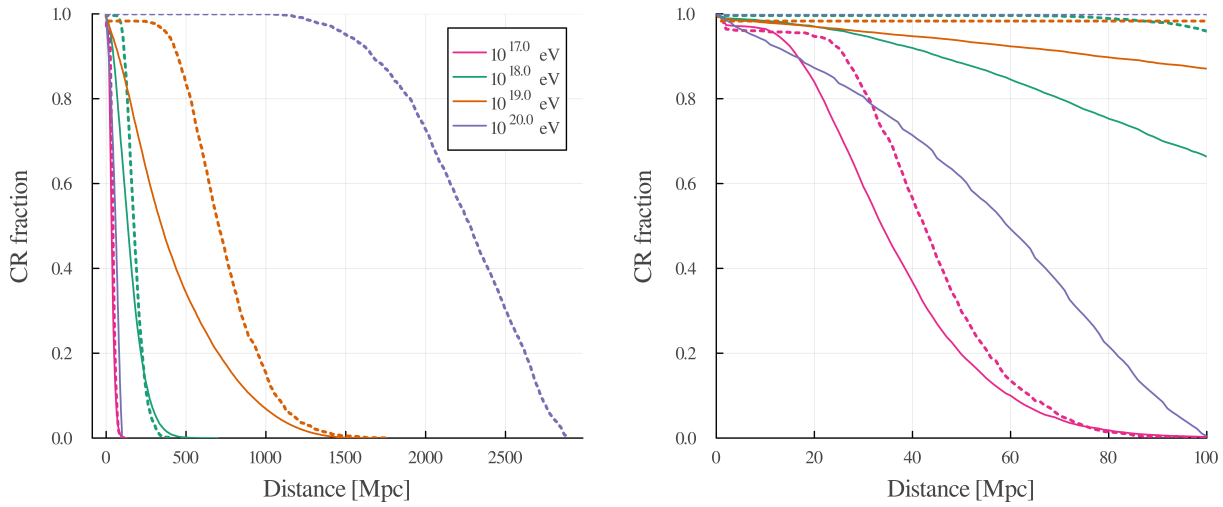

Figure 20: Comparison between the fraction of protons arriving with certain energies and their corresponding hypothetical travelled distance in the fiducial case (solid curves) and in the no loss model (dotted curves)

Since in this investigation the presence of the magnetic field is contemplated, it is important to highlight the link between the role of rigidity $R \propto E/Ze$ and the energy variation of the particle: when energy losses are taken into account, the particle's rigidity decreases over time, causing protons to become increasingly more confined in the magnetic field, whereas assuming a constant energy during the evolution allows high energy protons to maintain a high rigidity that permits to cover larger distances, whilst for low energy

particles the scale of propagation will be similar as in which losses are considered. Thus, including energy losses imposes a constraint on the propagation of high-energy particles, as they lose energy more rapidly than low-energy ones over a fixed time interval.

3 Results

3.1 Modelling the propagation of UHECRs with realistic simulations: the role of diffusion

As previously discussed, neglecting the presence of the magnetic field implies that the propagation of protons follows a ballistic regime, in which particles travel along straight-line trajectories without significant deflections. However, as presented in Sec.1.3, the latest studies demonstrate a growing evidence of the presence of magnetic fields on large scales: the diffuse synchrotron emission and RM observed along cosmic filaments and voids suggest their magnetisation which is also confirmed by the γ-ray observations of blazars possibly related to the detection of their corresponding GeV halos. All these recent revelations of the presence of magnetic fields in unexpected regions allowed to obtain more realistic simulations of these environments in which we can now inject UHECRs in order to study, for the first time, their propagation.

Thus, this section is devoted to the description of a further test which lets us analyze whether our simulated population of cosmic protons exhibits a propagation consistent with a *diffusive* propagation model. For this purpose we adopted, as a baseline reference model, the Bohm Diffusion Coefficient (section 1.4.2) as it represents the minimal estimate of the diffusion coefficient of charges moving in magnetized environment, in the assumption that the only important scattering scale is set by the particle gyration around the magnetic field. This model assumes that the length of the scattering is comparable with the Larmor radius of the particle ($D_{Bohm} = (1/3)\, r_L c$), meaning that the particles are already deviated on small scales. Thus, the Bohm scenario describes the slowest possible diffusion model, in which particles are confined in the magnetized region for long time: it gives the minimum possible diffusion coefficient, and the maximum possible diffusion time of a mono-energetic particle, under stationary conditions. This model is typically used to describe regions nearby shocks, where the turbulence is assumed to be strong (e.g. to describe the propagation of particles near SNR shocks), or in general is used for a first-order estimate of the minimum role of diffusion in the propagation of cosmic rays.
The Bohm coefficient for the propagation of relativistic particles is given by:

$$D_{Bohm} = 3 \times 10^{22} \frac{E\,[\mathrm{GeV}]}{B\,[\mu\mathrm{G}]} \quad [\frac{\mathrm{cm}^2}{s}] \quad = \quad 9.95 \times 10^{-11} \times \frac{E[\mathrm{GeV}]}{B[\mu\mathrm{G}]} \quad [\frac{\mathrm{Mpc}^2}{\mathrm{Gyr}}] \tag{36}$$

where B is the magnetic field in which the charge moves and E is the energy of the particle.

The first step in this analysis is to evaluate the magnetic field strength along the path of the particle. For this purpose, I studied the evolution of the field for each particle in order to characterize the amplitude of its fluctuations. Subsequently, I computed the median field strength over the entire population of protons at each timestep obtaining the general behaviour of the magnetic field during the 10 Gyrs evolution.
Fig. 21 shows that, in general, the median magnetic field crossed by the particles decreases in time, but the broad shaded region reproducing the magnetic fluctuations highlights that each particle, during its propagation, can in principle interact with regions more magnetized than others, where the field intensity spans from 10^{-13} up to 10^{-6} G.

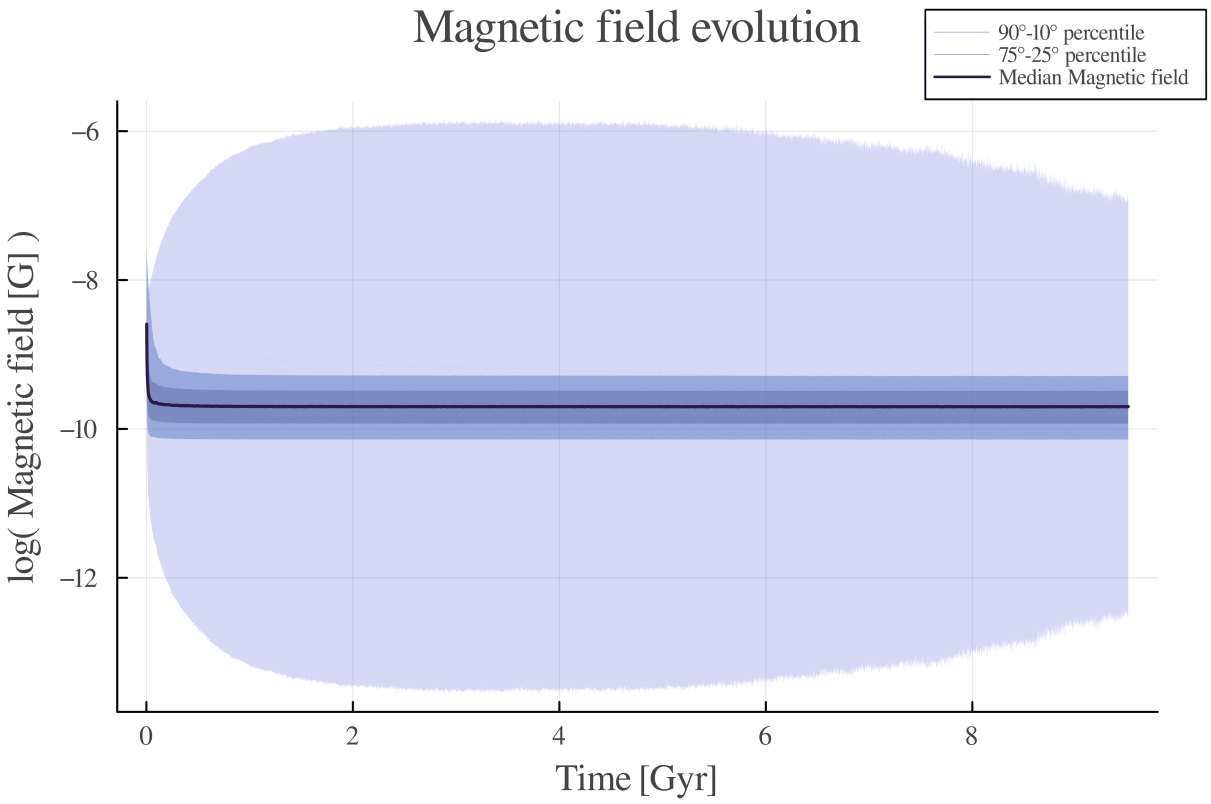

Figure 21: Magnetic field evolution: the purple curve represents the median value, the wide bubble the variance and the two shaded bands the $10° - 90°$ and the $25° - 75°$ percentiles

In order to compute the Bohm coefficient, I adopted a representative average field strength of $B = 0.37$ nG and used the energy of the particle at each timestep.

In this way, it is possible to obtain an estimate of the **temporal evolution of the Bohm coefficient** which is compared to an *effective* diffusion coefficient D derived from the true distance l travelled by the particle:

$$D \propto l^2/t \tag{37}$$

This reasoning has been applied in two scenarios: in the first case we neglect the energy losses component from which CRs suffer during their journey, assuming that each particle maintains its initial energy throughout the simulation, whereas in the latter we investigate the fiducial model, which takes into account the magnetic field and the typical losses that affect protons: the adiabatic expansion, pair and photo-pion production.

In both scenarios, the analysis has been carried out from two complementary perspectives: using the particle's *initial energy* at the injection, meaning that we are exploring the evolution from the first to the very last timestep of the evolution, and the *arrival energy*, i.e. the energy reached by the proton at the detection. For this purposes, I employed the `mag_hor` code to group the particles based on four energy bins: $10^{17}, 10^{18}, 10^{19}$ and 10^{20} eV which are going to be interpreted either as the *initial energy* or the *arrival energy*, depending on the specific analysis.

Then, for each energy bin, I computed the distance travelled by the protons using the data provided by UMAREL in order to estimate the effective coefficient $D \propto l^2/t$ which is compared with the Bohm coefficient (Eq. 36) calculated using the energy of the particle at each timestep and a magnetic field fixed at 0.37 nG, representing an average intensity.

Fig. 22 illustrates the evolution of the two diffusion coefficients in the case where energy losses are neglected

following the logic of tracking each particle from the moment of injection to the end of the simulation. The *dotted curves* represent the Bohm diffusion coefficient, calculated at each timestep with fixed field ($B = 0.37$ nG), averaged over protons grouped depending on their *initial energy*. Since the energy is kept constant in this scenario, the Bohm coefficient remains unchanged during the entire propagation. The *solid curves*, instead, show the true diffusion coefficient, estimated as $D \propto l^2/t$, also in this case averaged over protons within each group of initial energy, with error bands at $\pm 1\sigma$ indicating the statistical uncertainty.

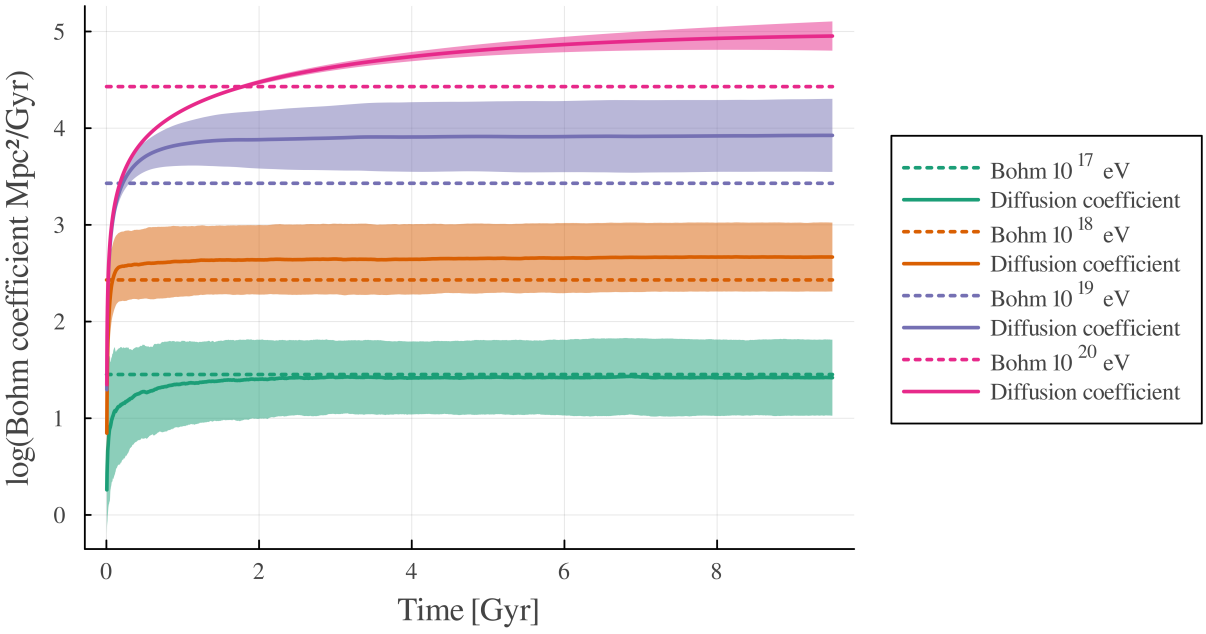

Figure 22: Evolution of coefficients from the first timestep to the end of the simulation for each energy bin *without* the energy loss effect. The dotted curves describe the Bohm coefficient, the solid ones the real coefficient with the error bands computed between $\pm 1\sigma$.

Instead, Fig.23 the `arrival_energy` mimics the detection event by selecting specific energy bins that resemble the energy at which the particle reaches the Earth ($10^{17}, 10^{18}, 10^{19}$ and 10^{20} eV), thus investigating the coefficients from the first instant until the detection time-step. Also in this case, the energy is kept constant and the Bohm diffusion coefficient is obtained according to Eq.36. Fig.23 shows the empirical coefficient (the solid line) compared with the theoretical one (dotted curve). In this case the error band, computed within $\pm 1\sigma$, are less visible as the requirement for selecting the proton arriving at certain energy is more strict than in the previous analysis.

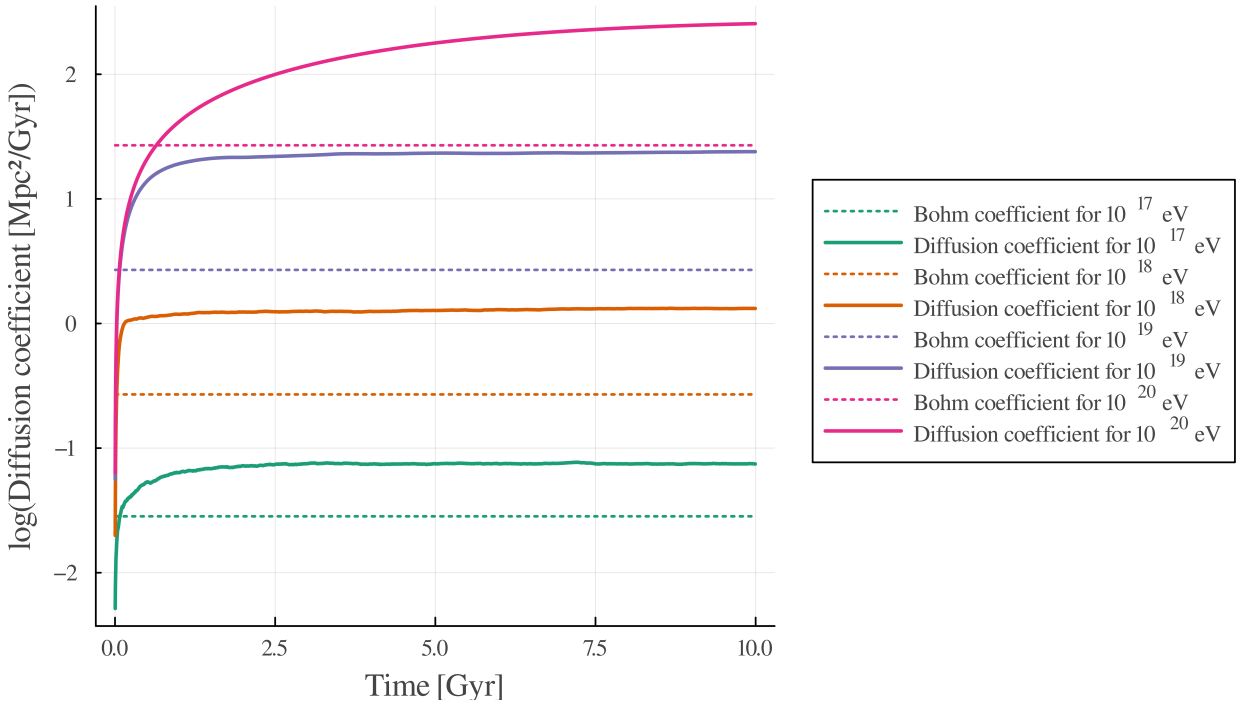

Figure 23: Evolution of coefficients from the first timestep to the time of detection for each energy bin *without* the energy loss effect. The dotted curves describe the Bohm coefficient, the solid ones the real coefficient with the error band computed between $\pm 1\sigma$.

In both panels, the Bohm coefficient remains constant due to the fixed magnetic field ($B = 0.37$ nG) and constant energy. However, the real coefficient shows a clear evolution in time: it starts from lower values and gradually increases as particles depart from their sources. This behaviour reflects the fact that, even if the energy is fixed, the coefficient depends on the real distance travelled by the particle, which, in turn, is determined by the strength of the magnetic field in that position at that timestep: in fact, the minimum value of the coefficient at the beginning of the simulation corresponds to when the particles are still in the proximity of the haloes that have originated them, in which the magnetic field is intense (see Fig.21). Then, as they diffuse into lower-density environments with weaker fields, the distance they can cover over a given time increases, thus enhancing the effective diffusion coefficient.

At this point, we add the energy loss effect, performing the same analysis previously done.
As shown in Fig. 24 and 25, respectively obtained with `mag_hor` and `arrival_energy`, the Bohm coefficient is no longer constant during the evolution due to the decrease of energy. Since $D_{Bohm} \propto E/B$, at the beginning of the simulation, the Bohm coefficient is at its maximum as the energy of the particle is high, in particular for particles injected with higher energies. In both cases we can visualise the amount of energy lost during the propagation: Fig. 24 shows that during the first million years of the simulation, the Bohm coefficient of particles with initial energy of 10^{20} eV rapidly declines during the early stages, in contrast to protons with initial energy of 10^{17} eV, as they experience less severe energy losses (see Fig.11). Then, as time goes by and the particles reach lower energy, the decrease of the Bohm coefficient becomes less dramatic, reflecting the slower rate of change at lower energies.

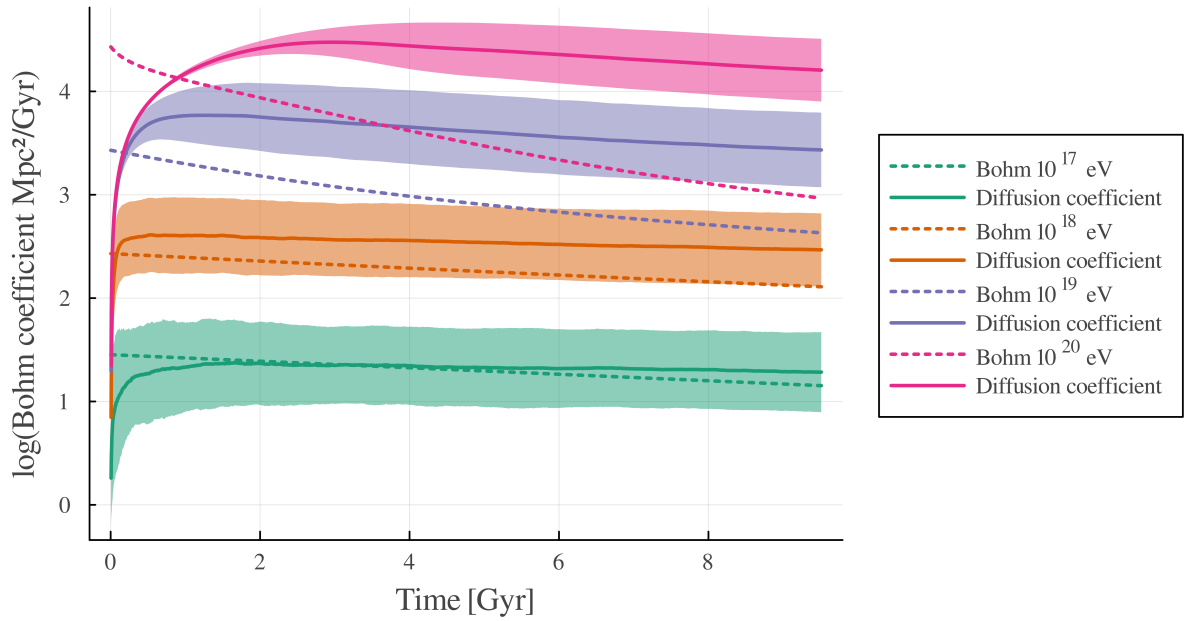

Figure 24: Evolution of coefficients from the first timestep to the end of the simulation for each energy bin *with* the energy loss effect. The dotted curves describe the Bohm coefficient, the solid ones the real coefficient with the error bands computed between $\pm 1\sigma$.

The result presented in Fig.25 is obtained by adopting the observational perspective, grouping particles by their *arrival energy*: each curve follows the coefficient's evolution from injection up to the time when the selected arrival energy is reached.
The first thing that we can notice is that the evolution is cut at some point of the simulation, depending on the selected energy bin. The coefficients computed for particles that reach us with energy of 10^{20} eV have a shorter evolution if compared with particles arriving with lower energies: this is a direct consequence of the initial conditions imposed by the simulation since the initial energy of those particles can be at most of 10^{21} eV. Thus, if a particle was injected with an energy of 10^{21} eV and detected at 10^{17} eV, then it had the possibility to evolve over longer time interval than the one with the same initial energy and observed at 10^{20} eV.
Also in this case, the importance of the magnetic field is tangible as it determines the contrast between the theoretical and the empirical diffusion coefficient: for each detected bin, in the theoretical model, having the field fixed at 0.37 nG, the Bohm coefficient is high at the beginning of the evolution and then decreases, following the behaviour of the energy evolution. In contrast, in the real scenario, which we remind being obtained according to $D \propto l^2/t$, the diffusion is at its lowest at the beginning since the particle is expected to be in a more magnetised site, then it increases reaching a stable value during the simulation since the proton is expected to propagate in less intense magnetic fields than the ones in proximity of the particle's source.

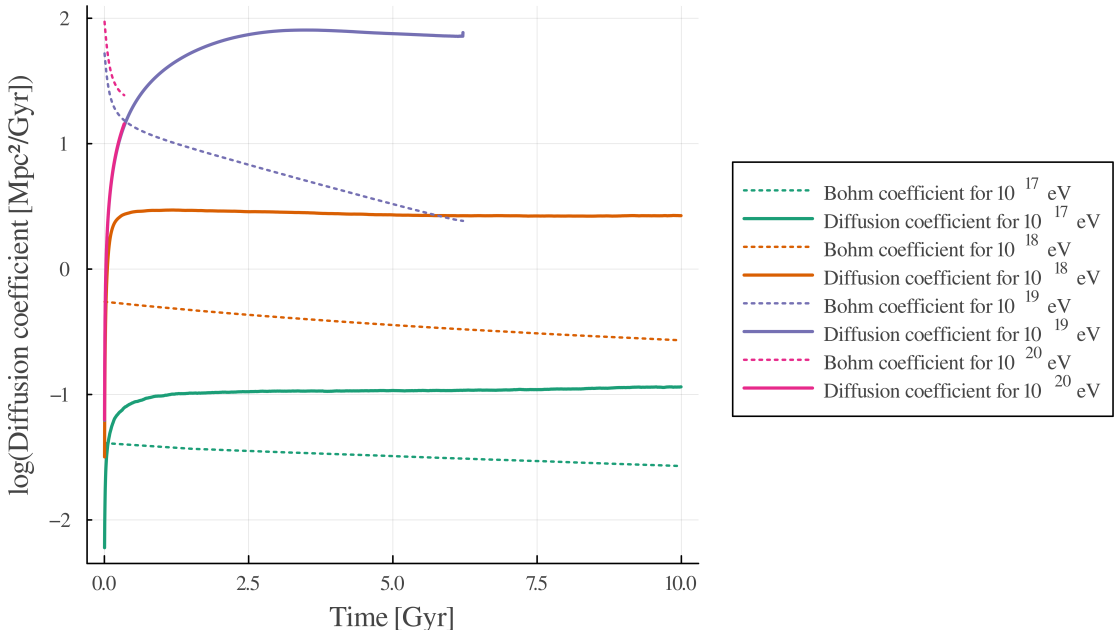

Figure 25: Evolution of coefficients from the first timestep to the time of detection for each energy bin *with* the energy loss effect. The dotted curves describe the Bohm coefficient, the solid ones the real coefficient with the error bands computed between $\pm 1\sigma$.

3.1.1 Comparison Between Realistic Proton Propagation and the Bohm Diffusion Model

Once the Bohm coefficient is determined, we can estimate the expected distance l travelled by the particle according to the Bohm model:

$$l = \sqrt{6 \times D_{Bohm} t} \tag{38}$$

and compare it with the true distance, computed with `mag_hor` and `arrival_energy` (Sec. 5). Again, we present the comparison under the two perspectives: the distance covered over the entire simulation and the distance travelled from the injection site up to the instant at which the particle has reached the Earth.
The aim of this investigation is to verify how the Bohm model computed in Sec.1.4.2 is consistent with a realistic propagation of protons.
For this purpose, we will investigate the simple scenario which neglects the energy loss term and compare it with the theoretical model, then the same approach will be adopted for the fiducial setup. The distances covered by protons will be also juxtaposed with some characteristic distances: the GZK cut-off of protons with energies $\sim 10^{19}$ eV at 30 Mpc and the Coma cluster, located at 100 Mpc from us.

The first case we examine is the one that follows the particle evolution from its injection timestep up to the end of the simulation, neglecting the energy loss effect.
To do so, using `mag_hor`, the population of protons was grouped depending on their initial energy and for each sample I derived the effective distance covered from the first timestep until the end of the simulation. The obtained results were compared, for each timestep, with the theoretical distance, given by Eq. 38 which uses the Bohm coefficient provided by the previous analysis, as displayed in Fig. 26. More precisely, the plot compares the distances effectively travelled (solid curves), averaged over the particles, for each energy bin with the ones obtained from the Bohm model (dotted curves) according to Eq. 38. Particles injected with energies of $\sim 10^{20}$ eV are able to reach thousands of Mpc, whereas the ones with initial energy 10^{17} eV can traverse at most few Mpc. This effect is due to the presence of the magnetic field, which, as shown in Fig. 21, presents wide fluctuations, against which protons have to resist in order to propagate. In fact, the cyan dashed curve, that describes the expected travelled distance without the presence of the magnetic field ($d = c \cdot t$), well represents the propagation of the 10^{20} eV particles, whose resistance is high, meaning that their regime is almost ballistic. For these protons, the Bohm model (dotted curve) overestimates the

travelled distance during the first million years of the evolution, but after ~ 2 Gyrs the prediction underestimate the actual situation. This effect is due to the fact that, in this analysis, the magnetic field used to compute the Bohm coefficient is fixed at 0.37 nG, which is too low to reflect the true magnetic strength in the haloes ($> 10^{-8}$ G), but can also be significantly higher to represent the typical values expected in the voids crossed by the particle ($< 10^{-10}$ G).
Conversely, protons with lower initial energies are more influenced by the presence of the magnetic field, which strongly deflects their trajectories, thus the ballistic regime is not appropriate to study their propagation. When applying the Bohm model to these low-energy particles, the expected distance (the dotted curve) given by Eq. 38 falls within the error bars computed for the effective ones, suggesting that the Bohm model can still provide a reasonable estimate of the propagation scale for particles in this regime. The discrepancies between the theoretical model and simulated distances can be ascribed to the fluctuations and inhomogenities of the magnetic field which are not captured in our definition of the Bohm coefficient.

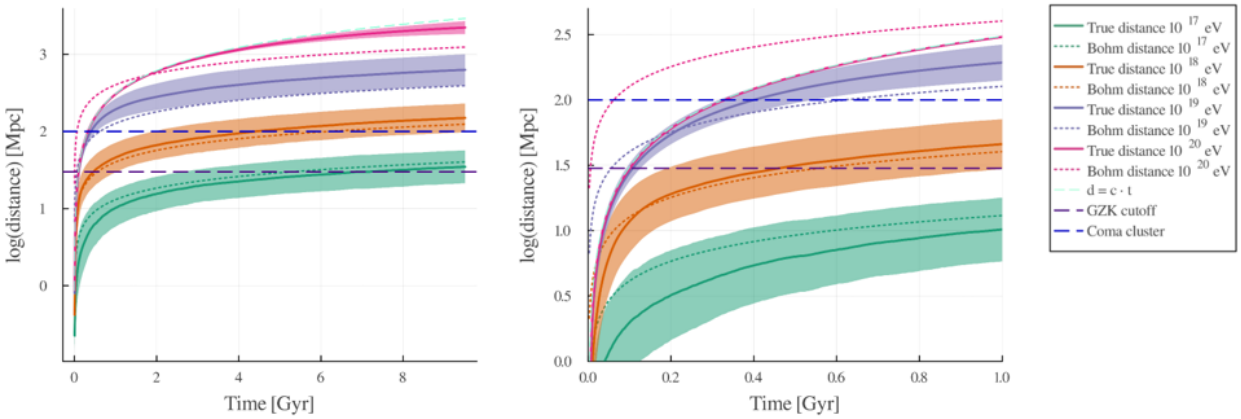

Figure 26: Distance covered from the beginning of the simulation until the very last timestep *without* the energy loss effect. The solid curves represent the true distance with the error band at $\pm 1\sigma$, the dotted ones the Bohm prediction. The cyan dashed curve the propagation in a non magnetised environment, the blue dashed curve is the Coma Cluster located at 100 Mpc and the indigo dashed curve represents the GZK cutoff at 30 Mpc. On the *left* a complete view over the entire 10 Gyr of evolution, on the *right* a zoomed version within 1 Gyr.

The same approach is adopted in the analysis for particles with *arrival energies* of $10^{17}, 10^{18}, 10^{19}$ and 10^{20} eV, still without considering the effect of the energy losses. Also in this case, the effective distance has been computed in `arrival_energy` from the injection timestep until the detection, whilst for the theoretical propagation the usual formula (Eq. 38) has been applied. The Bohm coefficient is calculated considering that the energy, under the current assumption, is constant, from the first timestep to the instant at which the particle is observed and the magnetic field strength still fixed to $B = 0.37$ nG.
Fig. 27 examines, for each arrival energy bin in the idealised case where energy losses are neglected, the assessment of the Bohm distances, the dotted curves, and the effective ones, the solid, with their error bands computed between $\pm 1\sigma$. Particles reaching us with energies of the order of 10^{20} eV tend to travel several thousands of Mpc following a ballistic propagation, as demonstrated by the overlapping with the cyan dashed curve, which describes how the motion would be without the magnetic field component, whereas a diffusive regime, as the Bohm model, is not adequate, since it would underestimate, almost by an order of magnitude, the actual covered distance.
Protons detected at 10^{18} and 10^{19} eV do not exhibit a ballistic pattern nor a diffusive one, which also in this case would underrate the propagation. When the particle arrives with an energy of 10^{17} eV, it could have travelled some tens of Mpc, and in this case the Bohm model could be used as an approximation.

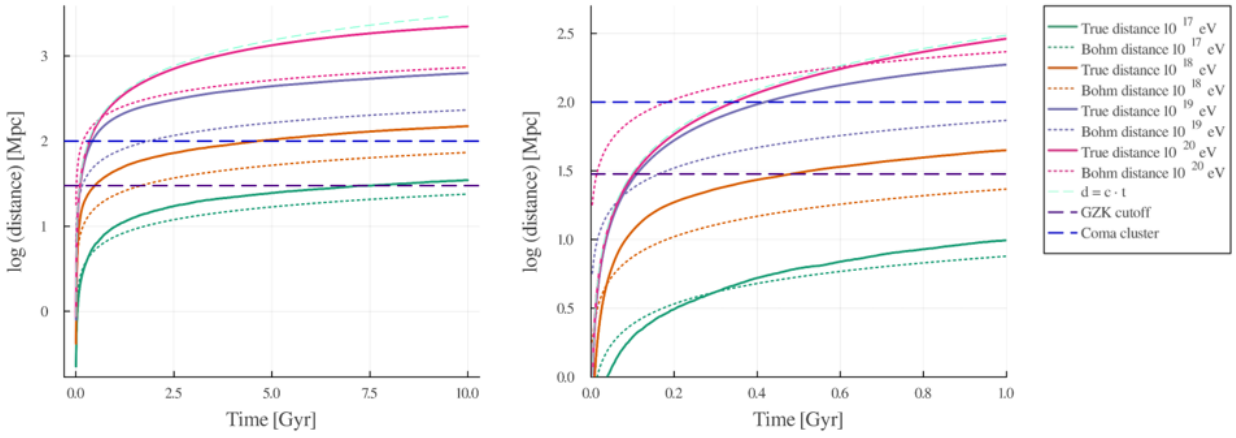

Figure 27: Distance covered from the beginning of the simulation until the detection *without* the energy loss effect. The solid curves represent the true distance with the error band at $\pm 1\sigma$, the dotted ones the Bohm prediction. The cyan dashed curve the propagation in a non magnetised environment, the blue dashed curve is the Coma Cluster located at 100 Mpc and the indigo dashed curve represents the GZK cutoff at 30 Mpc. On the *left* a complete view over the entire 10 Gyr of evolution, on the *right* a zoomed version within 1 Gyr.

At this point, we add the effect of the energy losses in order to see whether they can influence the agreement with the Bohm model, which is computed considering the change in energy at each timestep, still setting the magnetic field to 0.37 nG.

Again, we start by considering the case in which we follow the evolution of the particle from its injection until the very end of the simulation as shown in Fig. 28. This is done adopting the same approach as before: using `mag_hor` I collected the particles depending on their injection energy and for each group I computed the distance averaged over that sample from the injection instant to the end of the simulation, thus after 10 Gyr.
The propagation of particles with *initial energy* of 10^{20} eV can be described by the ballistic model ($d = c \cdot t$, the dotted cyan curve) during the first 1 Gyr of the evolution, but this approximation becomes inadequate after few Gyrs. In fact, as already explained in Sec. 1.5, particles with high energies are prone to lose a higher amount of energy, consequently resulting in a decrease of the rigidity which makes their propagation in the magnetic field difficult. This means that within 1 Gyr we can describe their motion using a ballistic approximation, which later would overestimate the actual distance. For these particles, the Bohm model is also inadequate, as it predicts a greater distance covered during the first Gyr than what is actually observed. This discrepancy arises because D_{Bohm} is calculated using a fixed value of $B = 0.37$ nG which is probably too weak to represent the actual strength. In contrast, after 1 Gyr the Bohm model underestimate the propagation as the true magnetic field crossed by the proton is weaker than the assumed value of 0.37 nG. For particles injected at 10^{19} eV, Bohm diffusion systematically underestimates the travelled distance by almost one order of magnitude. At lower energies (10^{18} and 10^{17} eV), the model still deviate from the actual propagation, although the discrepancy falls within the $\pm 1\sigma$ error band for both cases.

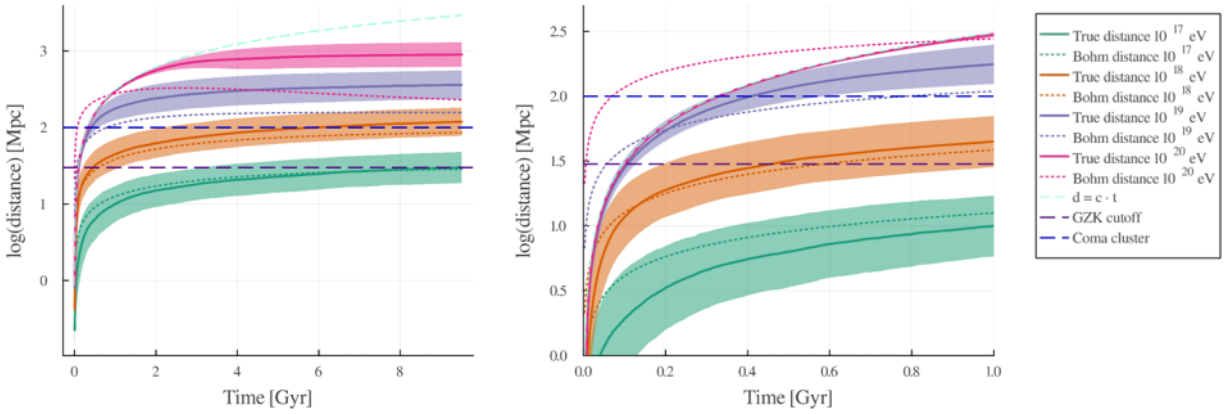

Figure 28: Distance covered from the beginning of the simulation until the very last timestep *considering* the energy loss effect. The solid curves represent the true distance with the error band at $\pm 1\sigma$, the dotted ones the Bohm prediction. The cyan dashed curve the propagation in a non magnetised environment, the blue dashed curve is the Coma Cluster located at 100 Mpc and the indigo dashed curve represents the GZK cutoff at 30 Mpc. On the *left* a complete view over the entire 10 Gyr of evolution, on the *right* a zoomed version within 1 Gyr.

Also for this investigation, the following step is to reproduce observations by selecting the *arrival energy* in order to compare the simulated distances according to our fiducial model with the ones predicted by the Bohm approach. As done previously, I selected the usual energy bins representative of observations, identified the corresponding timestep at which each bin is reached, and computed the distance travelled from injection up to that timestep. The obtained results were compared with the Bohm predictions according to which the expected distance is $l = \sqrt{6 D_{Bohm} t}$, for each timestep, from the injection until the time of detection.

Fig. 29 shows the outcome of this reasoning: differently from the previous results, some of the curves are truncated at specific timesteps that represent the instant at which the particles reach the energy corresponding to the detection. Since these particles would no longer be observable beyond that point, the evolution is not shown further.

Particles observed at 10^{20} eV follow an almost ballistic propagation regime (the cyan dotted curve) and can travel, at most, a few hundred Mpc before being detected. For these particles, as visible in the zoom version of Fig. 29 the Bohm model overestimates their propagation as it assumes a homogeneous magnetic field ($B \sim 0.37$ nG) which does not reflect the complex distribution assumed in the simulation. Particles with *arrival energy* of 10^{19} eV can be originated from sources located at nearly 1 Gpc. In this case, the Bohm model is not adequate to describe their motion: within some million years protons travel a shorter distance than the one predicted by Bohm diffusion, which, after ~ 4 million years, underestimates their propagation. Finally, particles detected with energies of 10^{17} and 10^{18} eV can cover at most some tens and hundreds Mpc respectively.

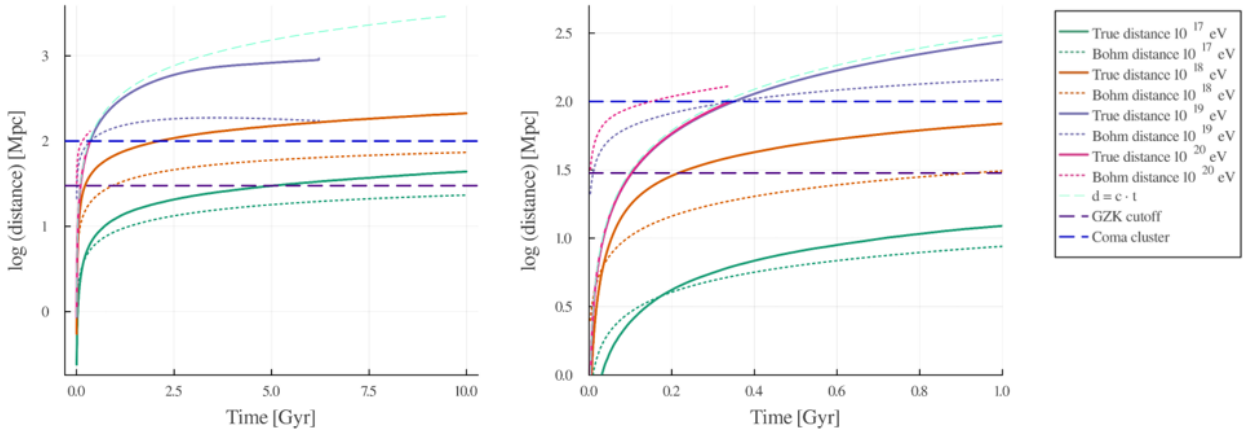

Figure 29: Distance covered from the beginning of the simulation until the detection *considering* the energy loss effect. The solid curves represent the true distance with the error band at $\pm 1\sigma$, the dotted ones the Bohm prediction. The cyan dashed curve the propagation in a non magnetised environment, the blue dashed curve is the Coma Cluster located at 100 Mpc and the indigo dashed curve represents the GZK cutoff at 30 Mpc. On the *left* a complete view over the entire 10 Gyr of evolution, on the *right* a zoomed version within 1 Gyr.

By comparing the two views, both in the fiducial and in the no loss scenario, we observe that the error bands associated to the effective distance travelled are significantly narrower in the case in which we are mimicing the detection with respect to when we follow the evolution from the injection up to the very end of the simulation. This arises from the way the data are sampled: when we choose the arrival energy bin, particles are selected at the specific timestep at which they reach a given energy and their travelled distance is computed from the injection up to that moment. This results in a more homogeneous subsets of particles, all reaching the same energy at comparable times and likely having expirienced similar energy loss mechanism and magnetic environments. As a consequence, the statistical dispersion in the propagation is reduced. In contrast, when we adopt the conmplementary perspective, particles grouped by their initial energy follow different propagation paths and reach various final energies, which increases the variability in the distance travelled, leading to broader error bands.

3.2 Constraining the Spatial Propagation of UHECRs

The results presented in Fig.17 and 20 show that the survival fraction for particles arriving at a certain energy bin decreases with propagation distance. This phenomenon can be approximately associated to an exponentially decreasing law:

$$N(x) = N_0\, e^{-\lambda/x} \tag{39}$$

where N_0 is the initial fraction of CRs, x the distance travelled by the particle and λ the attenuation scale. When $x = \lambda$, the surviving fraction of proton falls to roughly $1/e$ or $\sim 37\%$. This exponential reflects the effects of energy losses and deflections due to the magnetic fields during the particle's journey to reach Earth. Hence, in order to characterize the spatial propagation of protons, I constructed a summary table reporting the distance corresponding to the maximum radius within which $1 - 1/e$ ($\approx 63\%$) of particles detected at a certain energy bin could have covered in each scenario analysed in Sec.2.2.2.
For this purpose, I used the set of tables, one for each arrival energy bin, provided by `arrival_energy` that encode the information related to the fraction of protons arriving with a certain energy and the corresponding travelled distance. Thus, I selected the characteristic ratio of $1/e$ to obtain the typical propagation scale for each arrival energy bin and scenario, obtaining the table below (Tab.2).

Energy [eV]	Fiducial model [Mpc]	Only magnetic field [Mpc]	Only losses [Mpc]
10^{17}	40	47	2209
1.5×10^{17}	47	60	1995
3×10^{17}	72	93	1996
6×10^{17}	119	144	2070
10^{18}	165	193	2098
1.5×10^{18}	219	254	1848
3×10^{18}	298	392	1301
6×10^{18}	394	599	996
10^{19}	470	792	895
1.5×10^{19}	537	1027	816
3×10^{19}	549	1489	642
6×10^{19}	223	2015	226
10^{20}	70	2428	69
1.5×10^{20}	28	2690	28
3×10^{20}	11	2856	11
6×10^{20}	4	2902	4

Table 1: The table lists the maximum distances within which $\sim 63\%$ of cosmic ray protons, observed at a given energy, must have travelled, assuming three different scenarios: fiducial model (including energy losses and magnetic field effects), losses only (no magnetic field), and magnetic field only (no losses). These characteristic propagation lengths provide a quantitative comparison of the impact of magnetic diffusion and energy losses on cosmic ray transport

This approach enables us to compare the three different scenarios (fiducial model, no magnetic field and no losses) so that we can quantify the impact that energy losses and magnetic field can have on the propagation. Taking into account the fiducial scenario, which accounts for both energy losses and magnetic field effects, the 63% of the particles arriving with energy of 10^{17} eV originate from within a radius of ~ 40 Mpc. In contrast when magnetic fields are neglected, the same particles tend to propagate farther distances, as their motion is purely ballistic. Conversely, removing energy losses, but keeping the field, results in a propagation radius comparable with the fiducial model for low energy particle, but drastically different for protons at the highest energy regimes, as explained in Fig.11. This is particularly evident when particles are detected with high arrival energy, such as 6×10^{20} eV: in the fiducial model, they can cover few Mpc and similar distances are traversed if we neglect the magnetic field, but when we ignore the energy losses, then energetic protons can reach distances of thousands of Mpc, revealing how dominant energy degradation becomes at ultra-high energies (see Fig. 11) which, in turns, impacts on the rigidity of the proton.

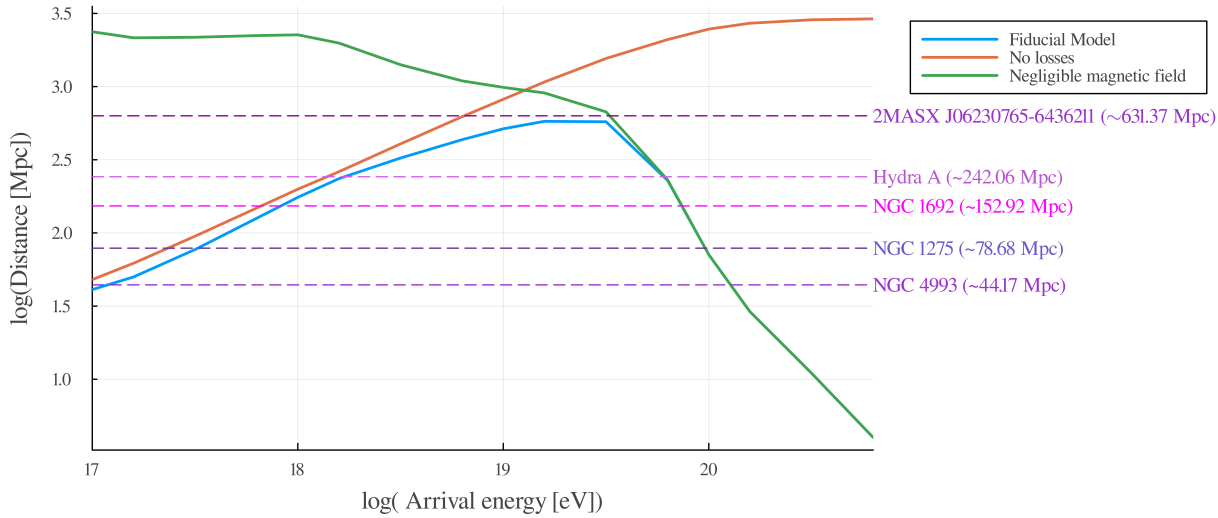

Figure 30: Maximum propagation distances within which $\sim$ 63% of cosmic ray protons are expected to originate, as a function of their arrival energy. The three curves represent different propagation scenarios: fiducial model (green), no energy losses (orange), and negligible magnetic field (blue). The horizontal dashed lines mark possible sources for UHECRs.

Fig. 30 provides a visual representation of the propagation distances corresponding to the $\sim$ 63% cosmic ray protons discussed in Table 2. The plot shows how the maximum distance travelled by the majority of particles varies with their arrival energy under the three usual scenarios: the fiducial model, the case without energy losses and the purely ballistic situation.
At low energies the inclusion of the magnetic field (blue and orange curves) causes a strong suppression in the propagation length which allows us to define the **magnetic horizon**, while ignoring the energy loss effect become evident in the high energy regimes. The horizontal lines marks the distances of specific radio galaxies in the Local Universe chosen from the catalogue described in Murgia, M. et al. [38] that have been selected according to their power ($L_{\rm Syn} > 10^{34}$ W) and distances ($d < 1000$ Mpc).

3.3 Varying the magnetic field

The previous sections have demonstrated the importance of considering the presence of a realistic distribution of magnetic fields in the study of the propagation of UHECRs.

At present, while the presence of magnetic fields outside of matter halos in the cosmic web is likely and supported by several observations (Ade et al. [3], Vazza et al. [54], Pshirkov et al. [45]), there still is quite some uncertainty in the actual level of magnetic fields in voids, whose value can at best be extrapolated from models who can successfully reproduce Faraday Rotation observations in filaments. In particular, the existing uncertain spectral energy distribution of the magnetic fields in the initial conditions makes the magnetisation of the Universe on $\sim 1 - 10$ Mpc scales quite uncertain.

At this point, we investigate two other scenarios in which protons are injected in an environment more and less magnetized than the reference fiducial case explored above.
Thus, the following step in this research is to inject the same sample of 93501 protons, with initial energy ranging from 10^{17} to 10^{21} eV in a magnetized environment in which the intensity of magnetic fields have been rigidly renormalised.
Firstly, I threw the usual UHECRs in a medium where the magnetic field is 10 times stronger than the one in the realistic setup used so far. Although being inconsistent with the latest radio observations, this magnetic field model would still in lined with the upper limits on the magnetisation of voids allowed by the modelling of the Cosmic Microwave Background (Paoletti and Finelli [42]).

Then, using the `arrival_energy` code, I computed the fraction of protons reaching Earth with the *arrival energy* bins of 10^{17}, 10^{18}, 10^{19} and 10^{20} eV in order to test how much the magnetic strength can impact on the travelled distance.

Below, Fig.31 displays the main result of this analysis: as expected, particles injected in a more magnetized medium (dotted curves) struggle to travel the same distance at a fixed arrival energy and this effect becomes more relevant for protons with low arrival energy (see the magenta lines).

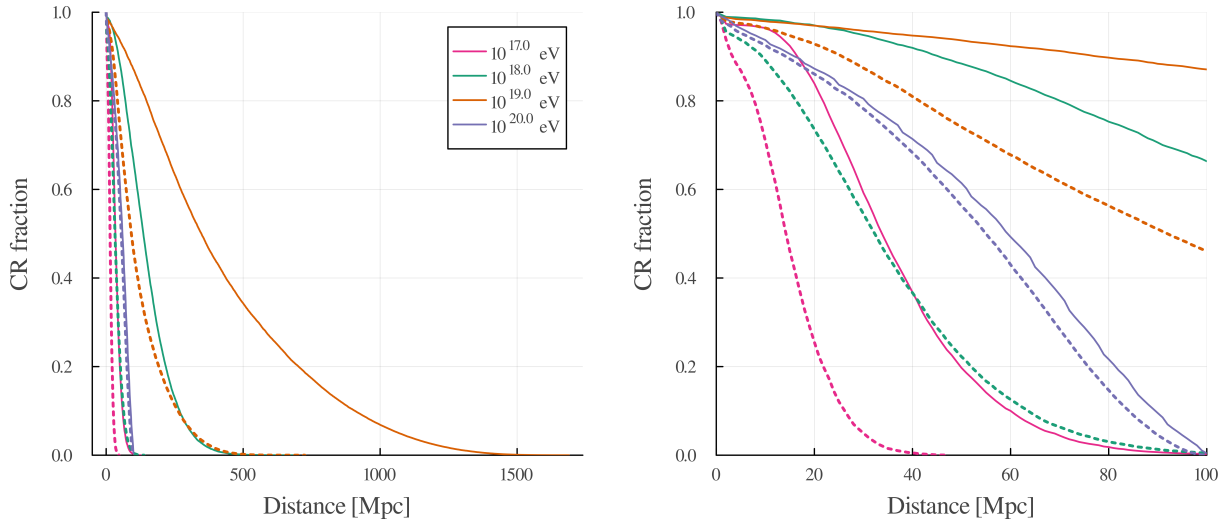

Figure 31: Comparison between the fraction of protons arriving with certain energies and their corresponding hypothetical travelled distance in the fiducial case (solid curves) and in a medium with a 10 times higher magnetic field

The same approach is adopted to compare the propagation of protons in an environment with a magnetic field 10 times lower than the fiducial case.

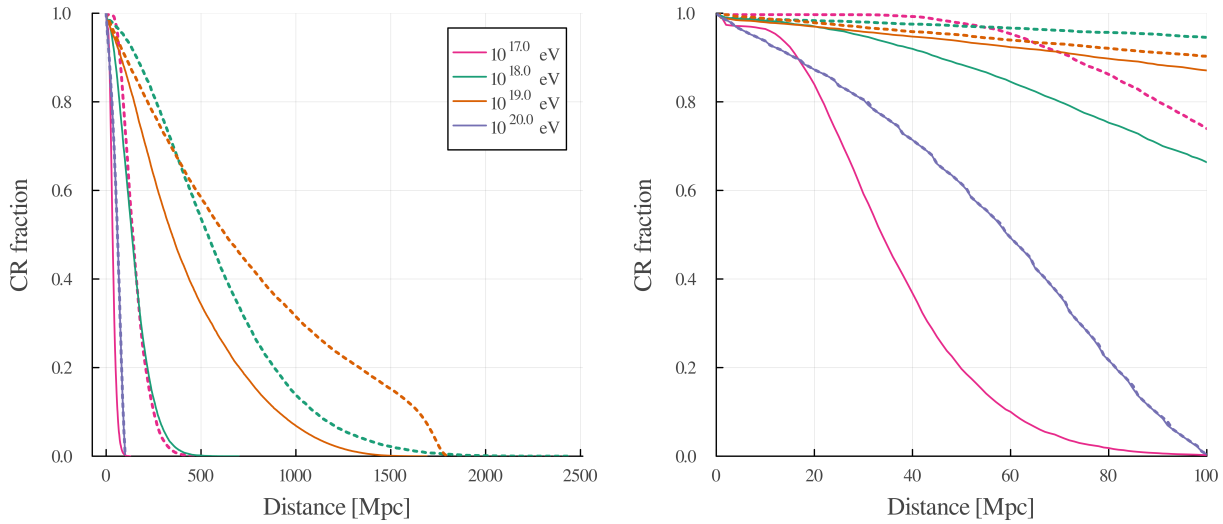

Figure 32: Comparison between the fraction of protons arriving with certain energies and their corresponding hypothetical travelled distance in the fiducial case (solid curves) and in medium with a 10 times less intense magnetic field (dotted curves).

Fig.32 shows that in a less magnetized medium (dotted curves) particles arriving with energies such as 10^{17} eV are able to cover some hundreds Mpc more than in the realistic case, whereas this effect is not relevant for energetic protons reaching us at 10^{20} eV.

Along the same lines of the previous section, I produced a summarizing table using the information of the CR fraction reaching Earth with a certain energy bin related to the corresponding travelled distance. More specifically, this table provides the maximum distances within which $\sim 63\%$ of cosmic ray protons, observed at a given energy, must have travelled.

Energy [eV]	Fiducial model [Mpc]	10× Magnetic Field [Mpc]	1/10× Magnetic Field
10^{17}	40	17	165
1.5×10^{17}	17	60	201
3×10^{17}	22	93	315
6×10^{17}	30	144	488
10^{18}	165	40	664
1.5×10^{18}	51	254	824
3×10^{18}	70	392	950
6×10^{18}	98	599	934
10^{19}	470	127	876
1.5×10^{19}	537	155	808
3×10^{19}	549	183	641
6×10^{19}	223	141	226
10^{20}	70	65	69
1.5×10^{20}	28	27	28
3×10^{20}	11	11	11
6×10^{20}	4	4	4

Table 2: The table lists the maximum distances within which $\sim 63\%$ of cosmic ray protons, observed at a given energy, must have travelled, according to the usual fiducial model (including energy losses and magnetic field effects), in a medium with a 10 times larger and smaller magnetic field.

In order to better visualize the impact of the magnetic field strength on the propagation length of protons, Fig.33 summarises the precedent analysis based on the comparison of the maximum distance travelled by the $\sim 63\%$ of CRs in the three usual cases, adding the study of the propagation in a medium with different magnetic intensities, increased and reduced of a factor of 10 (light blue and cyan curve respectively).

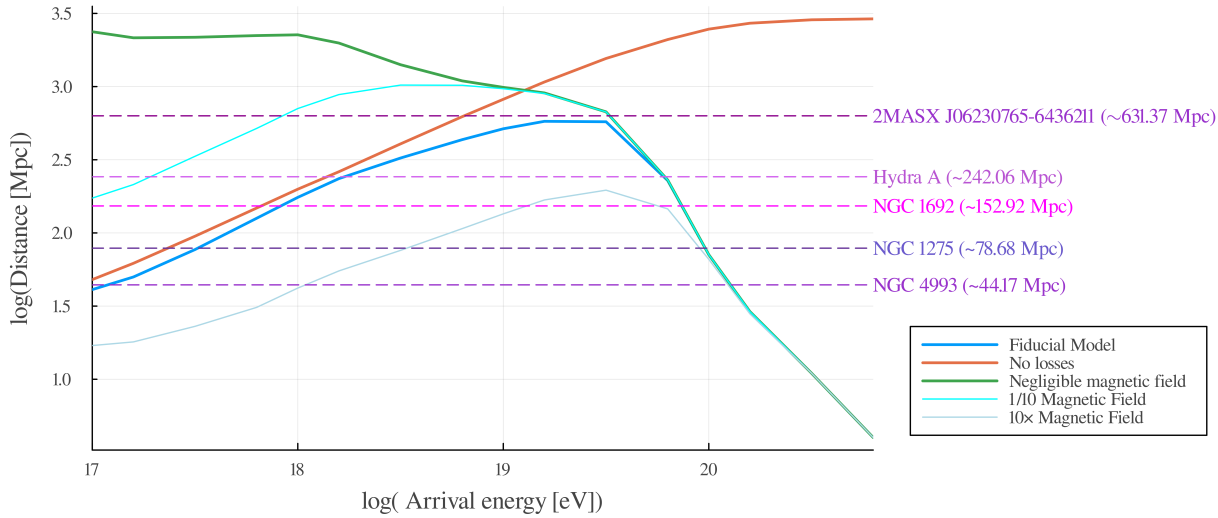

Figure 33: Maximum propagation distances within which $\sim$ 63% of cosmic ray protons are expected to originate, as a function of their arrival energy. The three curves represent different propagation scenarios: fiducial model (green), no energy losses (orange), and negligible magnetic field (blue). The cyan and lightblue lines represent the fiducial case where the magnetic field is, respectively, 10 times smaller and larger than the actual one. The horizontal lines mark possible sources for UHECRs

The first thing to notice is that the suppression of the covered distance becomes more evident with the increase of the magnetic field strength (light blue curve), whereas the curve representing the less intense field (cyan curve) is now closer to the one in which the propagation occurs in a non magnetized environment. This means that the lower the magnetic field crossed by the same sample of protons, the larger the covered distance. Although the covered distances in the three different magnetic field scenarios are clearly distinguishable for particles arriving with low energy, the results for the three different magnetic field strengths become more comparable as the arrival energy increases, being perfectly overimposed for energies higher than 10^{20} eV.
The fact that the covered distances in the two magnetic field cases are not a scaled up or down version of the fiducial scenario can be ascribe to the role of the particles' rigidity: low energy protons are more prone to follow a diffusive propagation regime in presence of an increasing magnetic field which induces stronger deflections; instead, when particles have high energies, especially larger than 10^{19} eV, the propagation becomes more ballistic, as the high rigidity facilitates the motion in the magnetized medium.

In future works, we plan to explore the impact of magnetic fields with a different initial power spectrum, allowed both by the comparison with radio observations and with the analysis of the Cosmic Microwave Background. This analysis is however expensive and it requires the usage of cosmological simulations which have not yet been produced for the same volume and resolution used in my Thesis.

3.4 Random injection

The results analysed in the previous Sections describe the propagation of a sample of nearly $\sim 10^5$ cosmic ray protons injected from the matter **haloes** identified in our simulation, meaning that their initial position is assumed to be related to the cells where the density is larger than a threshold value, mimicking a realistic scenario in which galaxies host the sources of UHECRs.

Now, for completeness we also want to investigate the relation between the maximum travelled distance by UHECRs and their initial location. To do so, I have injected in UMAREL the same amount of protons with the same initial energy, in the fiducial scenario but with the important difference that their starting positions were not chosen based on the density of cells, but were instead *randomly* chosen: thus they can start their propagation from a cosmic void as well as from a halo (and based on the volume filling factors of voids, this most often happens in the latter).

Below, a comparison of the starting positions of the 93501 protons in the two scenarios: on the left the injection occurs from the haloes, on the right the injection is random.

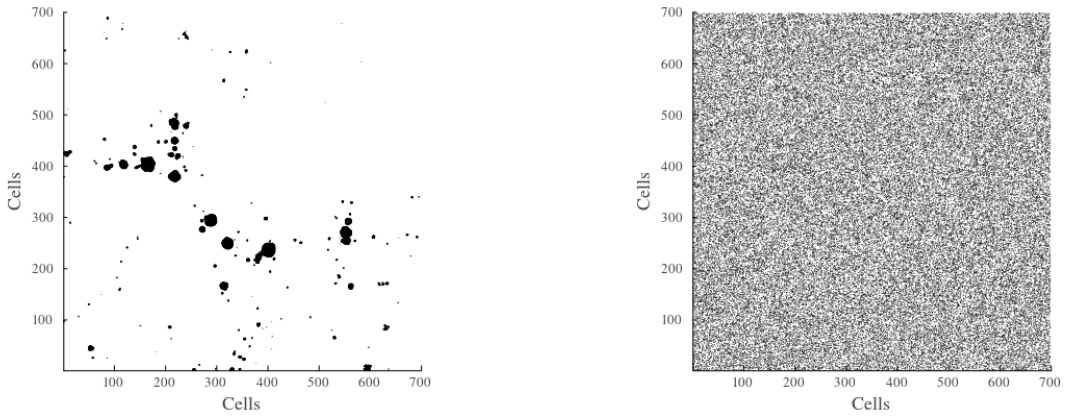

34a **34b**

Figure 34: Maps representing the (projected) initial location of CRs in terms of cells. The dark dots indicate the initial position of the UHECRs. On the left, the initial positions of protons correspond to the location of the haloes; on the right the initial position is randomly choosen, thus the distribution of CRs appears to be more homogeneous

In order to quantify the effect of the random injection, using the `mag_hor` and `arrial_energy` code, I computed the distance travelled in the two usual perspectives: from the first timestep until the last moment of the simulation, and from the first timestep until the time of the detection.
For the former analysis depicted in Fig.35, the four curves distinguish the four *initial energy* bins: the solid lines are related to the halo injection, the dotted ones to the new random injection. We can see that the two different scenarios are essentially identical, but if we focus on the distance travelled within less than 1 Gyr (right panel of Fig.35) protons with initial energy of 10^{17} and 10^{18} shows some relevant differences. This can be explained by their rigidity ($\propto E/B$): in fact, if the injection occurs in denser regions as in the first scenario, the particles start their trajectory always from an initial position which is biased towards a high magnetic field strength, and consequently the distance they initially cover is shorter than in the case in which the particle can depart from a cosmic void. On the other hand, protons with higher energy are not affected by this change of initial position, thanks to their higher rigidity.

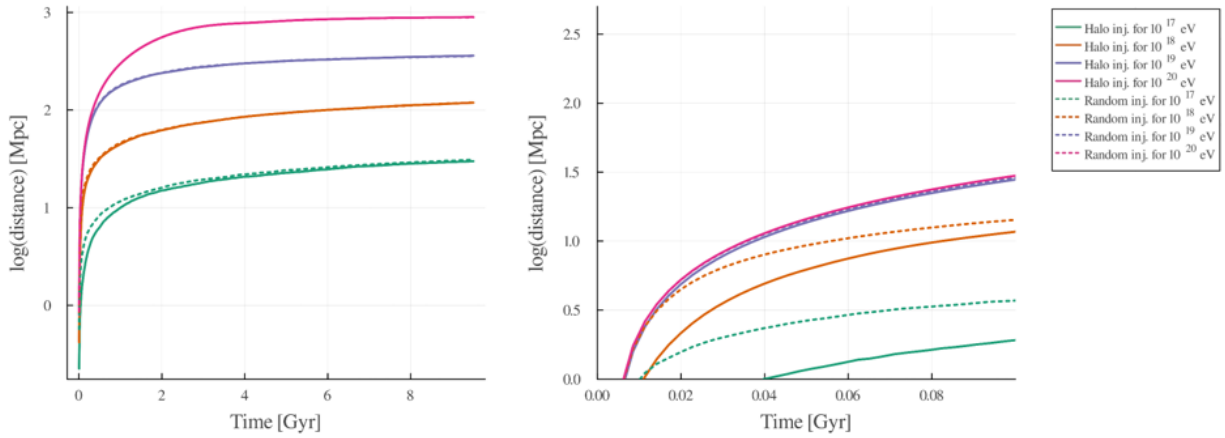

Figure 35: Comparison between the injection from haloes (solid curves) and the random injection case (dotted curves). The distance are computed from the first time step to the last instant of the simulation for the four usual *initial energy* bins.

The same reasoning is applied to the detection case, displayed in Fig.36: again, the solid curves depict the injection from haloes, whereas the dotted ones the random departure, for the four *arrival energy* bins.

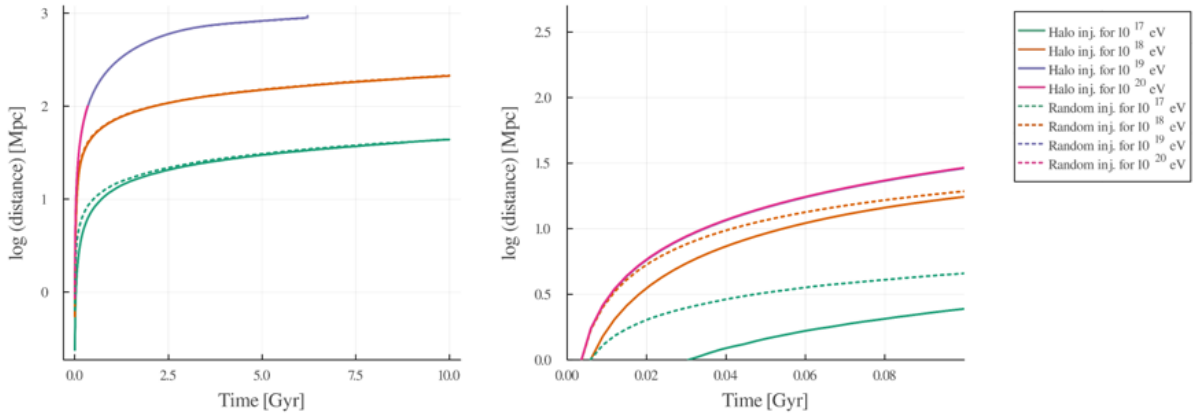

Figure 36: Comparison between the injection from haloes (solid curves) and the random injection case (dotted curves). The distance are computed from the first time step to the moment of the detection for the four usual *arrival energy* bins.

4 Discussion

As explained in Sec.1.4.2, diffusion is a type of propagation in which charges moving in a magnetic field follow a random walk. According to this process, the mean squared displacement is *linearly* related to time as $\langle r^2 \rangle \sim Dt$, where D is the diffusion coefficient.
It has been discovered that equations describing normal diffusion are not able to fully represent complex diffusion processes, such as the ones that take place in inhomogeneous environments. In fact, unlike typical diffusion, the *anomalous* diffusion follows a power-law behaviour:

$$\langle r^2 \rangle = D_\alpha t^\alpha \tag{40}$$

where D_α is the generalized diffusion coefficient and α is the anomalous diffusion exponent.
In this way, depending on the α value, it is possible to classify diffusion as follows:

- $\alpha < 1$: **subdiffusion**, which occurs when particles move more slowly than in a normal diffusion scheme. This situation is typical for inhomogeneous environments where particles can be easly trapped;
- $\alpha = 1$: **normal diffusion**
- $1 < \alpha < 2$: **superdiffusion**, according to which particles are able to move further in time than in a normal diffusion regime;
- $\alpha = 2$: **ballistic motion**

Therefore, at this point of the research, it is necessary to look for a regime that well describe the propagation of our UHECR protons. To do so, it is essential to find a value for α and D_α by fitting Eq.40 in a log-log scale:

$$\log(\langle r^2 \rangle) = \log(D) + \alpha \log(t) \tag{41}$$

Thus, I developed a julia-based algorithm which computes the mean squared distances travelled by the protons grouped depending on their injection energy. For simplicity, this analysis has been carried out without considering the energy loss mechanisms, thus the energy of the particle remains constant during the 10 Gyrs of the simulation. This is of course not what happens in reality, but it allows me a first cursory exploration of a more realistic way to parametrise the actual propagation of UHECRs as a function of their energy (and hence rigidity) in the realistic magnetic field model explored in this work.
The distance and time step information are then inserted in the `curve_fit` function provided by julia which brings the $\log(D)$ and the α values for each energy-based sample of protons.
With these two parameters, I defined the theoretical distance $y = \sqrt{D \times t^\alpha}$ which is compared with the actual travelled distance. Fig.37 reports the comparison between the theoretical model (dashed curve) and the data (solid curve) for each energy group with the corresponding α, D and the coherence length scale given by D/c that describes the length at which the CR is scattered of a certain angle.

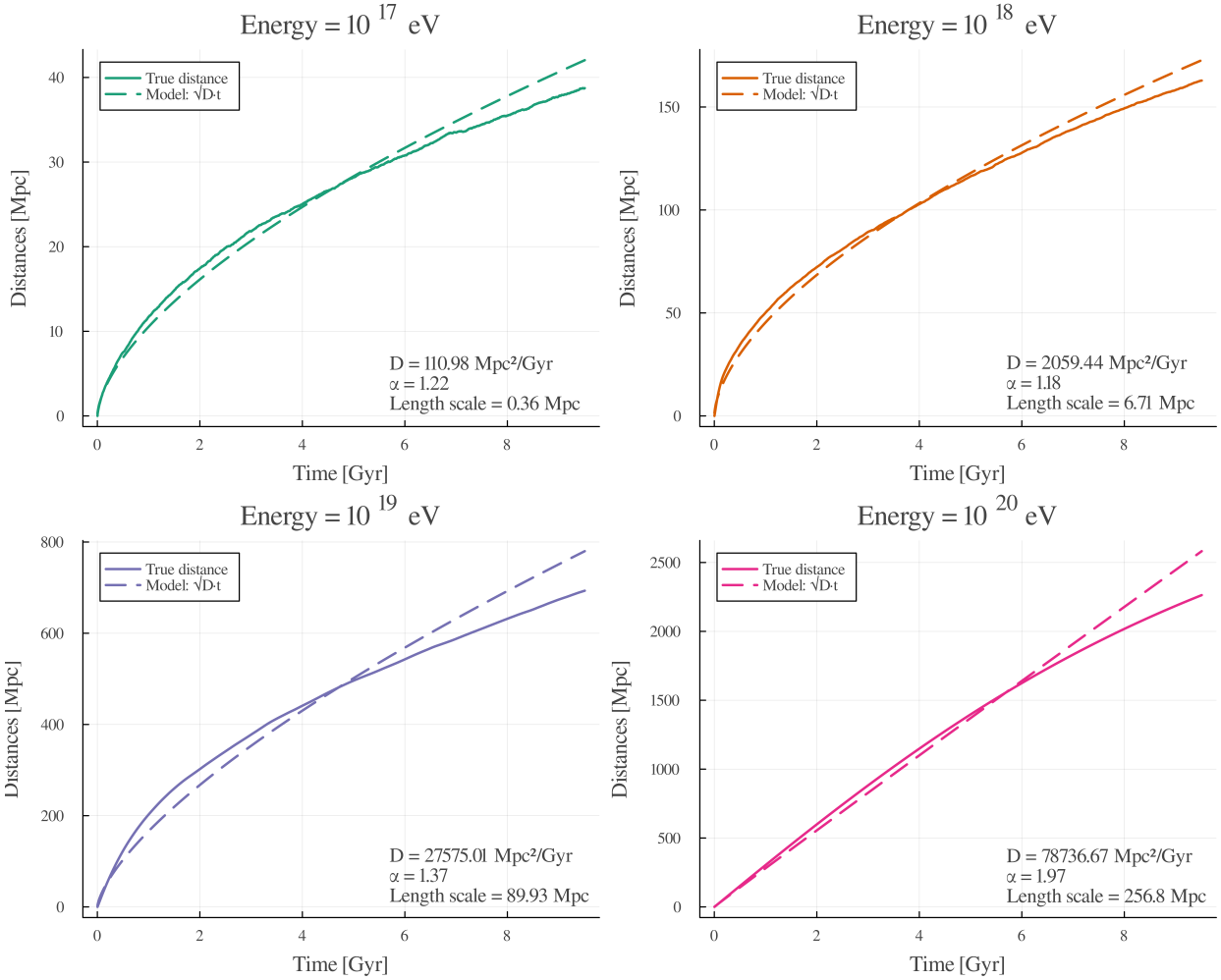

Figure 37: Comparison between the effective travelled path (solid curves) with the theoretical modelled distance (dashed curves) during 10 Gyrs of evolution neglecting the energy loss effects. Each plot focuses on a certain energy bin

Below, a table that summarizes the obtained values along with the error computed within 1σ and the corresponding D_{Bohm} coefficient.

Energy [eV]	α	D_α [Mpc^2/Gyr]	D_{Bohm} [Mpc^2/Gyr]	length scale [Mpc]
10^{17}	1.22 $\pm$ 0.01	110.98 $\pm$ 1.87	28.34	0.36 $\pm$0.01
10^{18}	1.18 $\pm$ 0.01	2059.44 $\pm$ 38.04	269.57	6.71 $\pm$ 0.12
10^{19}	1.37 $\pm$ 0.01	27575.01 $\pm$ 547.46	2692.11	89.93 $\pm$ 1.78
10^{20}	1.97 $\pm$ 0.01	78736.67 $\pm$ 1414.08	26911.68	256.78 $\pm$ 4.61

Table 3: Table encoding the values obtained from the fitting (α, D_α and the length scale) with their error computed within 1σ and the D_{Bohm} for a comparison

However, the recovered best fit relations are not reproducing the measured trend of D in a very accurate way. The reason appears to be related to the initial propagation stage, which is affected by the strong local magnetic field at the assumed source position (i.e. galactic haloes). To minimise this effect, I have also computed the best-fit relation by considering the propagation after 1 Gyr of evolution, in order to avoid the problem of the high magnetisation in proximity of the haloes. The outcome is depicted in Fig.38

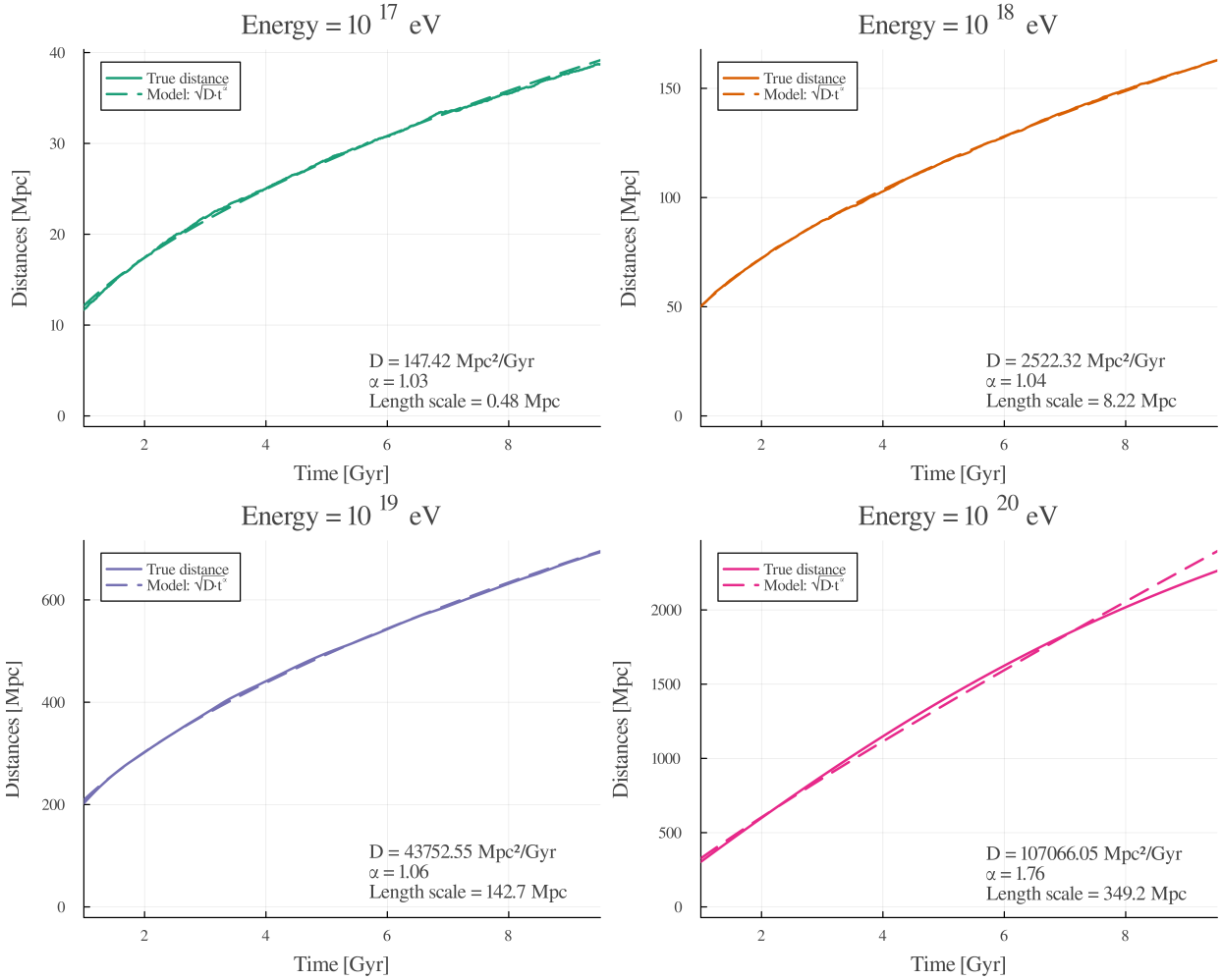

Figure 38: Comparison between the effective travelled path (solid curves) with the theoretical modelled distance (dashed curves) starting after 1 Gyrs from the injection moments neglecting the energy loss effects. Each plot focuses on a certain energy bin

Also in this case, I produced a table to better visualise the obtained values of α, D_α, the length scale along with their error within 1σ and the corresponding Bohm coefficient.

Energy [eV]	α	D_α [Mpc^2/Gyr]	D_{Bohm} [Mpc^2/Gyr]	length scale [Mpc]
10^{17}	1.0398 $\pm$ 0.0006	147.42 $\pm$ 0.15	28.34	0.4808 $\pm$ 0.0004
10^{18}	1.0448 $\pm$ 0.0002	2552.32 $\pm$ 0.97	269.57	8.226 $\pm$ 0.003
10^{19}	1.0665 $\pm$ 0.0003	43752.55 $\pm$ 26.88	2692.11	142.70 $\pm$ 0.08
10^{20}	1.767 $\pm$ 0.001	107066.05 $\pm$ 306.26	26911.68	349.20 $\pm$ 0.99

Table 4: Table encoding the values obtained from the fitting from 1 Gyr after the injection (α, D_α and the length scale) with their error computed within 1σ and the D_{Bohm} for a comparison

The values obtained for the α value allow us to distinguish in which regime the UHECR protons are located and to compare the results with the expected values derived from the Bohm model in Sec.3.1 which states $\alpha = 1$.

When considering the entire simulation duration, the α values are larger than the unity, meaning that a model inspired by superdiffusion would do better, compared to normal diffusion, in predicting the actual propagation of UHECRs in the regimes explored here. Furthermore, the α obtained for the 10^{20} eV protons is close to 2, suggesting that the high energy of these particles allows them to follow a ballistic regime, as indeed is observed by looking at the trajectories of particles.
For what concerns the diffusion coefficients, we can see that in all the energy bin cases the fitted values differ by an order of magnitude with respect the Bohm ones, meaning that the protons injected in the simulated environment tend to move faster than what predicted by the Bohm theory. Given the fitted values for the diffusive coefficients, it is now possible to estimate the **length scale** after which the protons are scattered of a certain angle: as expected, this value increases with the energy, meaning that the high rigidity permits the particle to cover a longer path that for the 10^{20} eV CRs can be of the order of hundreds of Mpc, before being scattered. On the contrary, the low energy ones, such as 10^{17} eV are not even able to reach the Mpc order of magnitude.

When we neglect the first Gyr of the simulation, in order to avoid the problem of the high magnetisation, we can see that the fitting procedure is greatly improved. We can see that the α values for particles with energy lower than 10^{20} significantly decrease and remain close to the unity, suggesting that a normal diffusion regime is now appropriate in the description of their propagation. Again, also in this case the Bohm model is not able to represent this scheme, as, due to the one order of magnitude lower values, it would underpredict the distance covered by those particles.
Contrarily, the 10^{20} eV protons still present a value for $\alpha > 1$ but not close enough to 2, thus these conditions are better described with a superdiffusion model rather than a ballistic one.
Also in this case, the Bohm model exhibits too low values for the coefficient if compared with the fitted one, thus it is not able to properly describe the motion of the particles.
The scale lengths value still represent the rigidity role in the magnetised environment: low energetic particles are able travel less than 1 Mpc before being deflected, but as their energy increases, they succeed in reaching tens and hundreds of Mpc, before being scattered.

Thus, particles with energies of $10^{17}, 10^{18}$ and 10^{19} eV can be modelled with a normal diffusion model different than the Bohm one, but the 10^{20} eV are in agreement with a superdiffusive scenario.
We have to remark that the discrepancy with the Bohm theory can be also ascribed to the way in which we have defined it by using the energy at each time step and a fixed value for the magnetic field (0.37 nG) which is not representative of the actual magnetic topology of the environment.
For what concerns the energetic protons, the superdiffusive theory states that these particles manage to travel longer distances than in a normal diffusion model. A possible physical scenario that can describe this situation is that the motion of these UHECRs can be pictured through a **Lèvy flight** model with a heavy tailed distribution, based on which the majority of the steps presents the same length, but, rarely, a longer pace occurs.
Similarly, a **patchy model** compatible with an intermittent superdiffusivity. According to this scenario, cosmic rays are mainly scattered in some intermittent turbulent structures of magnetic fields, where they follow a normal diffusive behaviour, but once they succeed in escaping these patchy regions, they are allowed to travel more easily. For instance, this "patchy model" has been tested by Butsky et al. [13] on galactic Cosmic Rays for which plausible candidates for the patchy structures has been attributed to "macroscopic" quasi-static ISM structures (e.g. GMCs, SNRs, PNe, stellar magnetospheres, HII regions, PWN). In the cosmic web environment represented here, such magnetic patches are represented by the localised increase of magnetic fields found in filaments, or the even larger spikes of magnetic fields found in matter haloes, and/or around active feedback sources. Based on the number reported in Table 4 found in the propagation of 10^{18} eV protons is of the order of the typical interseparation between strongly magnetised (≥ 10 nG) filaments in the cosmic web. At larger energies the much larger scales of $\geq 10^2$ Mpc plausibly represent the typical scale that a proton has to travel (in this case several times across the same periodic volume) before intercepting the strongly magnetised ($\geq 1 - 10\,\mu$G) volume of massive halos in the simulation.

In closing, my work can be compared to previous work obtained with the same ENZO cosmological code, to study the propagation of UHECRs, as in Hackstein et al. [26] and Hackstein et al. [27]. On one hand, the

representation of cosmic structures was more realistic in Hackstein et al. [27], in the sense that this paper used "constrained" simulations of the Local Universe, in which realistic twins of real structures (like the clusters of galaxies of Coma, Perseus, Virgo etc) formed and evolved in approximately their real 3-dimensional location. This is important in the study of specific observational patterns, like the (small) anisotropy of the arrival direction of UHECRs, and their possible relation with specific nearby cosmic structures. However, and estimate of the Magnetic Horizon does not appear to require the usage of constrained simulation as its properties can be inferred in a statistical sense, for any large enough cosmic volume. On the other hand, the simulations I have used are more advanced and realistic than the one use in Hackstein et al. [27] as they have a better spatial resolution, and more updated recipes for the injection of magnetic fields by galaxy feedback events, as well as for the initialisation of primordial magnetic fields, which is based on recent indications by radio observations [52, 14].

5 Conclusions

Magnetic fields are ubiquitous elements in the Universe, permeating regions across different scales with varying strengths which depend on the mechanism producing them. They could arise from the amplification of a primordial seed field and dynamo amplification, or they could come from outflows of galactic fields that were amplified by additional dynamo process. Moreover, the latest observations revealed their presence even in unexpected regions, far from obvious magnetic seed sources, as in cosmic voids and filaments. This means that understanding how observed magnetic fields emerged in the largest structures in the Universe still represents an open issue in modern astrophysics with several important ramifications in different lines of research.

For example (and at the very core of my Thesis), magnetic fields play a crucial role in the propagation of Cosmic Rays, since they bend the trajectories of charged particles under the Lorenz force action. This deflection limits the distance they can travel and introduces the so-called *magnetic horizon* that can modify the observed CRs spectrum, in particular for low rigidity particles.

Therefore, the aim of this Thesis was to evaluate the impact of the Extragalactic Magnetic Fields on the propagation of Ultra High Energy Cosmic Rays, thus for energies $\gtrsim 10^{17}$ eV, and to quantify how significantly their path can be affected by its presence.

This topic has recently become even more interesting, due to the puzzling distribution of arrival compositions of UHECRs measured by the PAO (see Abdul Halim et al. [1]), which might signal a selection effect played by extragalactic magnetic fields on the propagation of particles with different rigidities: their *observed composition*, in fact, implies that some effect should prevent particles with rigidity lower than 10^{18} V from reaching us.

For this purpose, I used the **ENZO cosmological simulation** which reproduces a portion of the Universe with a comoving volume of $(42.5 \text{ Mpc})^3$ exploiting the *newest* informations of magnetic fields strengths obtained from the studies of RMs (see Carretti et al. [15]). This is the fulcrum of this research, as it constitutes a realistic scenario in which it is possible to study and hypothesize the behaviour of energetic particles under realistic distributions of extragalactic magnetic fields, and to work under the assumption that the possible UHECRs sources correspond to the peaks of the density distribution.

To achieve this, I worked on the implementation of the julia-based code UMAREL which reconstructs potential CR trajectories according to the environmental setup and energy loss mechanisms, making use of the Boris Pusher method.

More specifically, for this investigation, I focused on ultra high energy cosmic ray *protons*, injected from dense regions, the **haloes**, with initial energies chosen in the range $10^{17} - 10^{21}$ eV and moving at the speed of light.

Then, I tracked their evolution over 10 Gyrs considering the magnetic field topology given by the ENZO simulation, and their typical loss energy processes: photo-pion production, pair production and the cosmological expansion. With these ingredients, I first tested the exact effect of losses and magnetic fields in the propagation of UHECRs, by alternatively including only one of the two: the fiducial case which considers both the energy losses and the influence of a real magnetic field, the scenario with a negligible magnetic field ($\sim 10^{-20}$ G), where particles are only affected by energy losses and the situation where energy losses are switched off and protons maintain their energy constant.

I developed two algorithms, `mag_hor` and `arrival_energy`, to compute the distance covered by the protons depending on their energy: the first code distinguishes the protons depending on their *initial energy* and it follows their propagation from the beginning to the end of the simulation, thus during 10 Gyrs. The second, on the other hand, mimics a detection event, by grouping the particles based on their *arrival energy* on Earth and tabulates, for each arrival energy bin, the fraction of protons that has travelled a certain distance from the injection site to Earth.

With the insights given by the `arrival_energy` code, it has been possible to measure the exponential decrease of the survival fraction of particles as a function of their energy and propagation distance (see

Fig.17 and 19) for each of the above mentioned scenario, and to emphasize the impact of the environmental conditions on the motion of CRs.

In particular, in this way I could measure the specific fraction of 1/e ($\approx 37\%$) of arrival protons to obtain the maximum distances within which $\approx 63\%$ of cosmic ray protons, observed at a given energy, has travelled. This analysis allows me to see the effect of the magnetic horizon on the propagation, especially for low energy particles which, due to their low rigidity, remain confined to shorter distances from their sources with respect to the higher energy ones.

This study showed that protons with arrival energies higher than 10^{20} eV are allowed to travel comparable distances independently of the selected scenario; therefore, it is reasonable to adopt, as a first order approximation, a ballistic approach. Conversely, the low energetic particles' propagation strongly depends on the chosen scheme: the presence of the magnetic field leads to a diffusive behaviour, where the proton path is continuously scattered as its rigidity is not high enough to resist against the magnetic field, whereas neglecting the magnetic field allows the same protons to cover larger distances. This suppression effect is of course enhanced when the field intensity is increased of a factor of ten.

A further step in this study was to determine which diffusive model was able to best reproduce our results, and to do so, the Bohm diffusion model has been chosen as a reference.
Thus, knowing that the Bohm coefficient can be defined according to Eq.36, I have computed for each particle population this quantity, exploiting the energy information that I had at my disposal at each timestep and fixing the magnetic field to an average value of 0.37 nG. This result has been compared with the empirical coefficient defined as $D \propto l^2/t$ where the l stands for the actual distance travelled by the particle, thus the one affected by the crossed magnetic field. At this point, exploiting the Bohm coefficient and the empirical distances already computed, I computed the expected distances according to the Bohm model, as shown in Fig.28 and 29 that have been compared with the true ones.
However, it is known that the Bohm approximation is extremely idealised, and in a complex multi-scale magnetic field distribution as the one in the simulated cosmic web, more realistic models should better describe the propagation of UHECRs. To improve on this, I experimented more suitable parametrisations of the collective propagation of UHECRs, within the framework of anomalous diffusion.
Hence, I applied a fitting to the general formula for diffusion $\langle r^2 \rangle = D_\alpha t^\alpha$ to find the diffusion exponent α and the coefficient D, allowing me to distinguish which regime among the normal diffusion, sub and super diffusion best reproduces the data.

Therefore, the key results achieved in this work can be summarized as follows:

- as expected, when UHECR protons propagate through extragalactic magnetic fields, their trajectories are deflected depending on their rigidity: the higher the rigidity, the smaller the bending effect (see Fig.34). This result, as shown in Sec.3.3, becomes more relevant as the magnetic field strength increases (see Fig.33): under equal arrival energies, particles injected in a more magnetized medium struggle to travel the same distance as the ones propagating in a less magnetized environment. In particular, protons arriving with a lower energy are more prone to follow a diffusive propagation regime, whereas particles detected with higher energies show a quasi-ballistic behaviour, as their high rigidity facilitates the motion in the magnetized field. In this latter case, protons moving in a magnetized medium follow the same pattern as the ones propagating in a non-magnetized environment;

- for the realistic model of extragalactic magnetic fields used here (which is derived from recent radio observations and numerical simulations), I could model the diffusion coefficient of UHECR protons in detail: assuming a Bohm diffusion model, the corresponding coefficient is computed at a fixed magnetic field value ($\sim$ 0.37 nG, which is the average magnetic field imposed in the initial conditions, under the assumption that it was generated by primordial mechanisms long before the structure formation began) whereas the empirical one, defined as $\propto l^2/t$, accounts for the true magnetic field crossed by the particle, which varies depending on the cell in which the proton is located (see Fig.21). This explains the discrepancy between the Bohm and the empirical coefficients found in this research (see Fig.22, 23, 24, 25), particularly relevant at the beginning of the simulation, when the proton is located in dense regions, where the magnetic field is typically more intense than the mean reference value of 0.37 nG. For the specific case in which the energy losses have been neglected, the Bohm coefficient is constant

during the entire simulation, whereas the empirical one is still affected by the variation of the magnetic field crossed by the proton;

- the comparison between the true travelled distances with the ones predicted by the Bohm model confirms that high energetic particles follow a ballistic regime, which can be described with $d = c \cdot t$, thus the simple diffusive theoretical model is not adequate to study their motion as it would underpredict the covered distance. The Bohm model seems to be sufficient in probing the trajectories of protons with lower energies, still presenting some divergences in the last timesteps of the simulation;

- when considering the entire simulation a normal diffusion scheme is not adequate for this analysis as the α values are far from the unity, meaning that the superdiffusion and the ballistic model are more suitable to study, respectively, protons with energy 10^{17-19} and 10^{20} eV. Conversely, when the fitting starts after 1 Gyr from the beginning of the simulation (which allows us to neglect the strong impact of the magnetic field in halos), the normal diffusion is appropriate in case of protons with energies below 10^{20} eV, while for higher energies the superdiffusion is better suited to describe their propagation rather than a ballistic regime (see Table3 and 4). Thus, a possible scenario can be described by a Lèvy flight-like model, where particles are able to cover, once in a while, longer paths;

- the previous results refer to the realistic scenario in which UHECR protons are injected from the haloes, where the magnetic field is expected to be intense. In Sec.3.4, it is shown that the initial position of the proton *does not affect* the travelled distance. In fact, this result assumes that choosing a **random site** for the injection, far from magnetised structures, leads to the same path length. Yet, some differences can be pinpointed for low energetic protons which are more affected by the magnetic field influence;

In concluding, my Thesis has highlighted the importance that realistic magnetic field models have on the propagation of UHECRs and, in particular, I have demonstrated the emergence of a magnetic horizon effect, that strongly limits the propagation of those particles, especially the low rigidity ones, causing a suppression of the incoming UHECRs flux detected on Earth.

This is why the most recent results of the magnetic field strengths play a crucial role in these analysis, as they allow to construct a realistic stage to perform more and more accurate simulations of the possible trajectories of UHECRs.

Hence, in future studies, we aim to investigate the effects of magnetic fields characterized by a different initial power spectrum, based on both radio observations and Cosmic Microwave Background analyses. However, this kind of analysis is computationally demanding and requires cosmological simulations that have not yet been generated with the same volume and resolution adopted in this Thesis, and it will be deferred to future work. Moreover, a natural extension of this study is to involve the analysis of heavier nuclei since it could provide deeper insights into the role of the magnetic field in the propagation of UHECRs and help to constrain their origin and composition.

Appendix

This section is dedicated to the description of the algorithms used to obtain the results for this Thesis: *arrival_energy* and *mag_hor*.

`arrival_energy.jl`

The UMAREL code provides a file containing the information of energy and positions for each proton during the entire simulation. Thus, I developed a julia-based code that simulates the detection of protons, following a realistic energy distribution E^{-1}.
At these energy ranges, the observed CRs spectrum follows $E^{-3.1}$, which is compatible to an injection spectrum with a E^{-2} trend. Since the high steepness would require extremely low statistic at high energies, the injection spectrum is structured to behave as E^{-1}, so that 1000 protons with initial energy 10^{17} eV corresponds to 1 particle with initial energy of 10^{20} eV. Then, a further weighing of E^{-1} is applied to the energy data allowing us to obtain realistic weighed averages for the cosmic rays sample and to avoid the low number statistic problem for the high energy protons.
For this purpose, I selected some relevant energy bins from the UMAREL file, representing the energy at which the CR is detected on Earth and the corresponding time-step at which the energy is reached. Then, I created an array called `distances` encoding the distance travelled by each particle from the beginning of the simulation to the moment of the detection, where the rows represents the protons and the columns the time-steps.
At this point, I have extracted the maximum distance travelled by the sample of CRs in order to compute the fraction of protons, with respect to the total amount of particles observed with a certain arrival energy, able to travel a given distance.
These informations are organized in tables, one for each energy bin describing how many protons arriving with that energy have travelled a certain distance.

```
filep1 = string(root_out, filename)

#Reading the file

px = h5read(filep1,"px")  #...X position without periodic BC
py = h5read(filep1,"py")  #...Y position without periodic BC
pz = h5read(filep1,"pz")  #...Z position without periodic BC
energy = h5read(filep1,"E[eV]")  #...energy
t = h5read(filep1,"time")         #...list of simulated timestep


initial_energy = energy[:, 1] #Vector with the initial energies of each particle
weights = 1.0 ./ initial_energy #Structuring the weighted initial energy distribution

for n in [17, 17.2, 17.5, 17.8, 18, 18.2, 18.5, 18.8, 19, 19.2, 19.5, 19.8, 20, 20.2, 20.5,
    20.8, 21]

    initial_cr, time_step = size(energy)

    distances = Array{Float64}(undef,initial_cr, time_step) #Initializing the array with the
         distance travelled at each timestep
    valid_particles = Int[] #All the particles reaching 10^{n} eV goes in this vector

   @inbounds for i in 1: initial_cr

        id = findall(x -> isapprox(x, 10.0^ n, rtol=0.1), energy[i, :]) #Looking for the
            timestep at which the particle reaches a certain energy 10^{n} eV

        ###################################################################
        if isempty(id)
            distances[i, :] .= 0.0
            #particle $i does not reach 10^$n eV
            continue
        end
```

```
        append!(valid_particles, i)

        #Initial position of the particle
        px0 = px[i, 1]
        py0 = py[i, 1]
        pz0 = pz[i, 1]

        @simd for j in 1 : id[end] - 1 #Computing the distance
            dx = px[i, j] - px0
            dy = py[i, j] - py0
            dz = pz[i, j] - pz0

            distance =  sqrt(dx^2 + dy^2 + dz^2) * 0.0415 #in Mpc
            distances[i, j] = distance

        end


    end

    abs_max_d = round.(Int64, maximum(distances))

    rounded_d = map(x->round(Int64, x),distances)

    #Computing the fraction of CRs arriving on Earth that has travelled a certain distance
        in Mpc
    dist = Float64[]
    frac_cr = Float64[]
    frac_cr_w = Float64[]
    total_weight = sum(weights[i] for i in valid_particles)
    @inbounds for d in 0 : abs_max_d

        append!(dist, d)

        #Applying the weighted initial energy
        selected_indeces = filter(i -> any(rounded_d[i, :] .>= d), valid_particles)
                                                                    #che percorrono la
            distanza d
        weighted_count = sum(weights[i] for i in selected_indeces)
        append!(frac_cr_w, weighted_count/total_weight)
    end


#Creating the tables with Fraction vs Distance
tab_dir_w = joinpath(root0, file*"_tables_10^$n.dat")
df_w = DataFrame(x = dist, y = frac_cr_w)
CSV.write(tab_dir_w, df_w)


ev_bohm = Float64[] #Vector with Bohm coefficient at each timestep
bohm_arr = Float64[] #Vector with the theoretical distance
coeff = Float64[] #Vector with the empirical coefficient

    #Statistics

    std_d_ar = Float64[]
    error_d = Float64[]
    error_b = Float64[]

    for t in 1:time_step
      vals = distances_arr[:,t]

      #filtering needed when the particle does not reach the energy 10^n eV
      filtered_dist = filter(x-> x !== missing && x > 0.0, vals)
      active_ids = findall(x -> x !== missing && x > 0.0, vals)
      e_val = energy[active_ids, t]
```

```
    bohm_a = 9.95e-11 .* (e_val .* 1e-9) ./ 0.37 #Computing Bohm coefficient given the
        arrival energy
    bohm_d =sqrt.(6 * ( 9.95e-11 * (e_val * 1e-9) / 0.37)*t) #Computing the theoretical
        distance at each time step
    coeff_d_ar = filtered_dist.^2/(6*t) #Computing the empirical coefficient

    if isempty(filtered_dist)
      append!(dist, NaN)
      append!(coeff, NaN)
      append!(bohm_arr, NaN)
      append!(ev_bohm, NaN)
      append!(std_d_ar, NaN)
      append!(error_d, NaN)
      append!(error_b, NaN)
      continue
    else
      append!(dist, mean(filtered_dist))
      append!(coeff, mean(coeff_d_ar))
      append!(bohm_arr, mean(bohm_d))
      append!(ev_bohm, mean(bohm_a))
      append!(std_d_ar, std(filtered_dist))
      append!(error_d, std(filtered_dist)/(filtered_dist*log(10)))
      append!(error_b, std(coeff_d_ar)/(coeff_d_ar*log(10)))

    end

  end

end
################################################################################
```

As an example, the main output is Fig.39: this plot has been obtained under the fiducial case and describes the detection events for different arrival energies. It is visible that for each bin, 100% of protons have travelled 0 Mpc and the fraction progressively decreases with increasing distances.

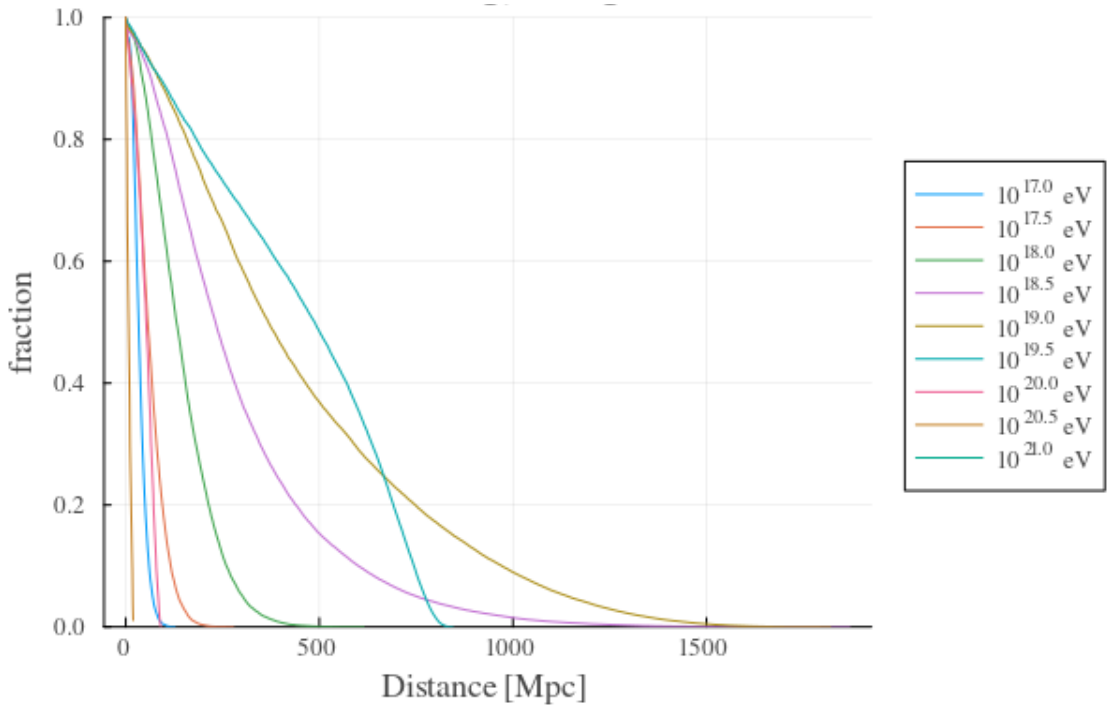

Figure 39: Fraction of CRs able to travel a certain distance: each curve represents the percentage of protons arriving with a given energy and the corresponding travelled distance.

With this routine it is possible to compute the Bohm coefficient, defined as Eq.36, and compare it with the empirical one which behave as $\propto l^2/t$. In the first case, the magnetic field is fixed to an average value of 0.37 nG, whereas in the second one, the coefficient takes into account the real distance travelled by the particle which depends on the crossed magnetic field.
Since some protons are not able to reach the required energy, it is necessary to apply a filtering in order to exclude from the analysis all those particles. This procedure allows us to compare the normal diffusive model with measurements.

mag_hor.jl

I implemented the `mag_hor.jl` routine to compute the distance covered by the protons over 10 Gyrs, using the data obtained in `UMAREL.jl` code. More precisely, it selects the initial energy of each cosmic ray and computes the distance travelled with respect to the injection site and adds to the `mean_distances` vector the distance averaged over the particles, at each timestep.

The main output of the algorithm is the one presented in Fig.40 which shows the distances travelled by protons under the fiducial scheme, grouped according to the injection energy, compared with the distances travelled by the same sample of proton in the case with a negligible magnetic field.

```
filep1=string(root_out, name)

#Reading the file
px = h5read(filep1,"px")  #...X position without periodic BC
py = h5read(filep1,"py")  #...Y position without periodic BC
pz = h5read(filep1,"pz")  #...Z position without periodic BC
energy = h5read(filep1,"E[eV]")  #...energy
t = h5read(filep1,"time")         #...list of simulated timesteps
B = h5read(filep1, "B[G]")


c =  306.6 #speed of light [Mpc/Gyr]



  for n in [17, 18, 19, 20]
  #
    id = findall(x ->  isapprox(x, 10.0^n, rtol = 0.1), energy[:, 1]) #Searching for the
        particles with initial energy 10^n eV

    mean_distances = Float64[] #Initializing the vector with the empirical distances
        averaged over the population of particle with initial energy 10^n
    bohm_distances = Float64[] #Initializing the vector with the theoretical distances
        according to the Bohm model l =    (6*bohm * t)

    bohms =Float64[] #Initializing the vector with the Bohm coefficient computed at each
        time step

    diff_coeff = Float64[] #diffusion coefficient obtained from true distances (D = l^2/t)

    std_dist = Float64[]
    std_coeff = Float64[]
    std_bohm=Float64[]

    #Initial position of protons
    x0 = px[id, 1]
    y0 = py[id, 1]
    z0 = pz[id, 1]


   meanB = 0.37*1e-3 #averaged magnetic field

  for i in 1:length(t) #Computing the distances
```

```
        dx = px[id, i] - x0

        dy = py[id, i] - y0

        dz = pz[id, i] - z0


        distance = sqrt.(dx.^2 + dy.^2 + dz.^2) * 0.0415


        append!(mean_distances, mean(distance)) #Averaging the distances over the particles
            with initial energy 10^{n} eV at each timestep
        append!(std_dist, std(distance))

        #Bohm coefficient
        bohm = 9.95*10^(-11) * (energy[id, i] * 10^(-9))/(meanB) #[cm^2/s] E in GeV, B =0.3
            nG-->3*10^(-4)in microgauss
        l = sqrt.(6*bohm * t[i]) #theoretical distance (BOHM) *3.15 *10^(16)) /(3.08 *
            10^(24))#[cm->Mpc]

        coeff_d = distance.^2/(6*t[i]) #empirical diffusion coefficient

        append!(diff_coeff, mean(coeff_d))
        append!(std_coeff, std(coeff_d)) #band around the diffusion coefficient
        append!(std_bohm, std(bohm)) #band around the Bohm coefficient
        append!(bohm_distances, mean(l) )

        append!(bohms, mean(bohm))



    end
#
    ##########################################################################################################
```

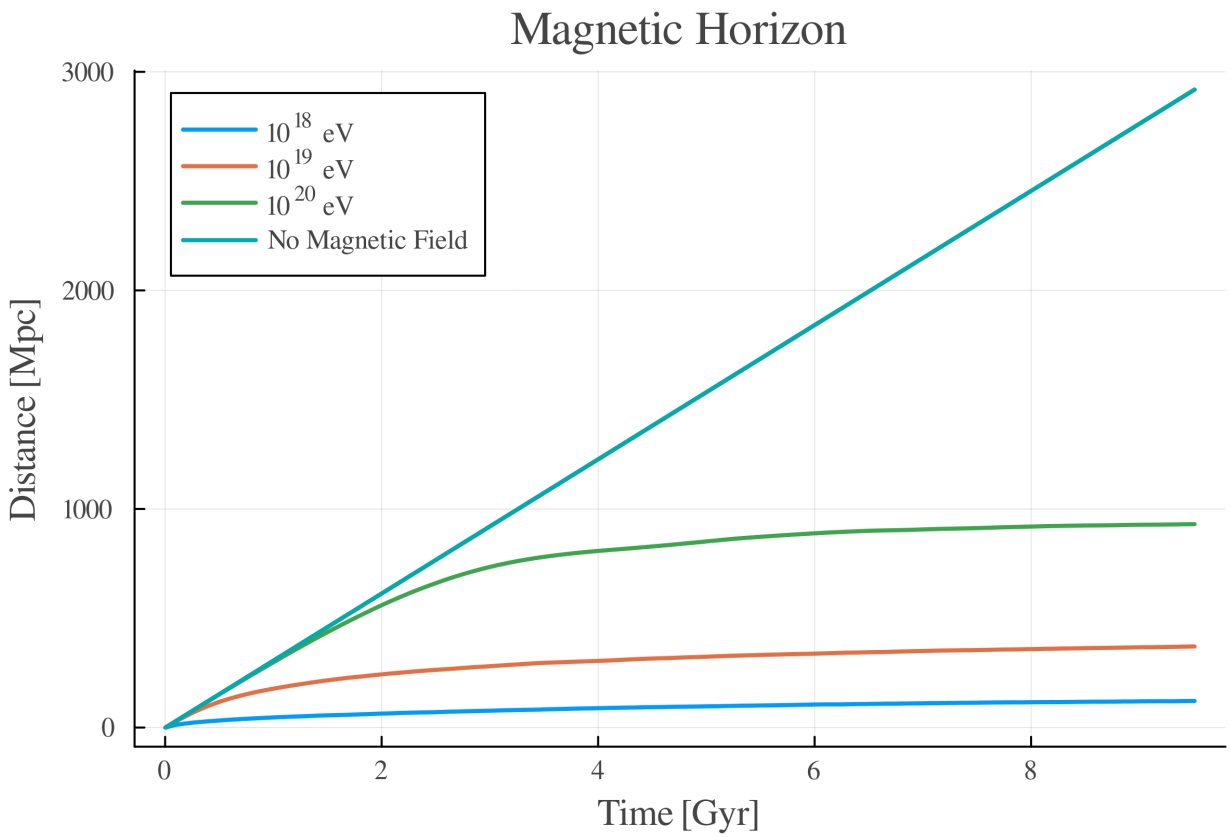

Figure 40: Average distance over time covered by UHECRs with an initial energy randomly chosen between 10^{18}, 10^{19} and 10^{20} eV at the injection.

This code computes the Bohm coefficient according to:

$$D_{Bohm} = 9.95 \times 10^{-11} \times \frac{E\,[\mathrm{GeV}]}{B\,[\mu\mathrm{G}]} \tag{42}$$

and the empirical one $D = l^2/6t$ at each timestep, from the beginning of the simulation to the last timestep, thus during 10 Gyrs. With these information, the corresponding distances are computed and compared with the theoretical ones depending on the initial energy.

References

[1] A. Abdul Halim, P. Abreu, M. Aglietta, I. Allekotte, K. Almeida Cheminant, A. Almela, R. Aloisio, J. Alvarez-Muñiz, J. Ammerman Yebra, G.A. Anastasi, L. Anchordoqui, B. Andrada, S. Andringa, L. Apollonio, C. Aramo, P.R. Araújo Ferreira, E. Arnone, J.C. Arteaga Velázquez, P. Assis, G. Avila, E. Avocone, A. Bakalova, F. Barbato, A. Bartz Mocellin, J.A. Bellido, C. Berat, M.E. Bertaina, G. Bhatta, M. Bianciotto, P.L. Biermann, V. Binet, K. Bismark, T. Bister, J. Biteau, J. Blazek, C. Bleve, J. Blümer, M. Boháčová, D. Boncioli, C. Bonifazi, L. Bonneau Arbeletche, N. Borodai, J. Brack, P.G. Brichetto Orchera, F.L. Briechle, A. Bueno, S. Buitink, M. Buscemi, M. Büsken, A. Bwembya, K.S. Caballero-Mora, S. Cabana-Freire, L. Caccianiga, F. Campuzano, R. Caruso, A. Castellina, F. Catalani, G. Cataldi, L. Cazon, M. Cerda, A. Cermenati, J.A. Chinellato, J. Chudoba, L. Chytka, R.W. Clay, A.C. Cobos Cerutti, R. Colalillo, M.R. Coluccia, R. Conceição, A. Condorelli, G. Consolati, M. Conte, F. Convenga, D. Correia dos Santos, P.J. Costa, C.E. Covault, M. Cristinziani, C.S. Cruz Sanchez, S. Dasso, K. Daumiller, B.R. Dawson, R.M. de Almeida, J. de Jesús, S.J. de Jong, J.R.T. de Mello Neto, I. De Mitri, J. de Oliveira, D. de Oliveira Franco, F. de Palma, V. de Souza, B.P. de Souza de Errico, E. De Vito, A. Del Popolo, O. Deligny, N. Denner, L. Deval, A. di Matteo, M. Dobre, C. Dobrigkeit, J.C. D'Olivo, L.M. Domingues Mendes, Q. Dorosti, J.C. dos Anjos, R.C. dos Anjos, J. Ebr, F. Ellwanger, M. Emam, R. Engel, I. Epicoco, M. Erdmann, A. Etchegoyen, C. Evoli, H. Falcke, G. Farrar, A.C. Fauth, F. Feldbusch, F. Fenu, A. Fernandes, B. Fick, J.M. Figueira, A. Filipčič, T. Fitoussi, B. Flaggs, T. Fodran, T. Fujii, A. Fuster, C. Galea, B. García, C. Gaudu, A. Gherghel-Lascu, U. Giaccari, J. Glombitza, F. Gobbi, F. Gollan, G. Golup, M. Gómez Berisso, P.F. Gómez Vitale, J.P. Gongora, J.M. González, N. González, D. Góra, A. Gorgi, M. Gottowik, F. Guarino, G.P. Guedes, E. Guido, L. Gülzow, S. Hahn, P. Hamal, M.R. Hampel, P. Hansen, D. Harari, V.M. Harvey, A. Haungs, T. Hebbeker, C. Hojvat, J.R. Hörandel, P. Horvath, M. Hrabovský, T. Huege, A. Insolia, P.G. Isar, V. Janardhana, P. Janecek, V. Jilek, J.A. Johnsen, J. Jurysek, K.-H. Kampert, B. Keilhauer, A. Khakurdikar, V.V. Kizakke Covilakam, H.O. Klages, M. Kleifges, F. Knapp, J. Köhler, F. Krieger, N. Kunka, B.L. Lago, N. Langner, M.A. Leigui de Oliveira, Y. Lema-Capeans, A. Letessier-Selvon, I. Lhenry-Yvon, L. Lopes, L. Lu, Q. Luce, J.P. Lundquist, A. Machado Payeras, M. Majercakova, D. Mandat, B.C. Manning, P. Mantsch, F.M. Mariani, A.G. Mariazzi, I.C. Mariş, G. Marsella, D. Martello, S. Martinelli, O. Martínez Bravo, M.A. Martins, H.-J. Mathes, J. Matthews, G. Matthiae, E. Mayotte, S. Mayotte, P.O. Mazur, G. Medina-Tanco, J. Meinert, D. Melo, A. Menshikov, C. Merx, S. Michal, M.I. Micheletti, L. Miramonti, S. Mollerach, F. Montanet, L. Morejon, K. Mulrey, R. Mussa, W.M. Namasaka, S. Negi, L. Nellen, K. Nguyen, G. Nicora, M. Niechciol, D. Nitz, D. Nosek, V. Novotny, L. Nožka, A. Nucita, L.A. Núñez, C. Oliveira, M. Palatka, J. Pallotta, S. Panja, G. Parente, T. Paulsen, J. Pawlowsky, M. Pech, J. Pkala, R. Pelayo, V. Pelgrims, L.A.S. Pereira, E.E. Pereira Martins, J. Perez Armand, C. Pérez Bertolli, L. Perrone, S. Petrera, C. Petrucci, T. Pierog, M. Pimenta, M. Platino, B. Pont, M. Pothast, M. Pourmohammad Shahvar, P. Privitera, M. Prouza, S. Querchfeld, J. Rautenberg, D. Ravignani, J.V. Reginatto Akim, M. Reininghaus, A. Reuzki, J. Ridky, F. Riehn, M. Risse, V. Rizi, W. Rodrigues de Carvalho, E. Rodriguez, J. Rodriguez Rojo, M.J. Roncoroni, S. Rossoni, M. Roth, E. Roulet, A.C. Rovero, P. Ruehl, A. Saftoiu, M. Saharan, F. Salamida, H. Salazar, G. Salina, J.D. Sanabria Gomez, F. Sánchez, E.M. Santos, E. Santos, F. Sarazin, R. Sarmento, R. Sato, P. Savina, C.M. Schäfer, V. Scherini, H. Schieler, M. Schimassek, M. Schimp, D. Schmidt, O. Scholten, H. Schoorlemmer, P. Schovánek, F.G. Schröder, J. Schulte, T. Schulz, S.J. Sciutto, M. Scornavacche, A. Sedoski, A. Segreto, S. Sehgal, S.U. Shivashankara, G. Sigl, G. Silli, O. Sima, K. Simkova, F. Simon, R. Smau, R. Šmída, P. Sommers, J.F. Soriano, R. Squartini, M. Stadelmaier, S. Stanič, J. Stasielak, P. Stassi, S. Strähnz, M. Straub, T. Suomijärvi, A.D. Supanitsky, Z. Svozilikova, Z. Szadkowski, F. Tairli, A. Tapia, C. Taricco, C. Timmermans, O. Tkachenko, P. Tobiska, C.J. Todero Peixoto, B. Tomé, Z. Torrès, A. Travaini, P. Travnicek, M. Tueros, M. Unger, R. Uzeiroska, L. Vaclavek, M. Vacula, J.F. Valdés Galicia, L. Valore, E. Varela, V. Vašíčková, A. Vásquez-Ramírez, D. Veberič, I.D. Vergara Quispe, V. Verzi, J. Vicha, J. Vink, S. Vorobiov, C. Watanabe, A. Weindl, L. Wiencke, H. Wilczyński, D. Wittkowski, B. Wundheiler, B. Yue, A. Yushkov, O. Zapparrata, E. Zas, D. Zavrtanik, and M. Zavrtanik. Impact of the magnetic horizon on the interpretation of the pierre auger observatory spectrum and composition data. *Journal of Cosmology and Astroparticle Physics*, 2024(07):094, July 2024. ISSN 1475-7516. doi: 10.1088/1475-7516/2024/07/094. URL http://dx.doi.org/10.1088/1475-7516/2024/07/094.

[2] Martina Adamo, Silvia Pietroni, and Maurizio Spurio. Astrophysical sources and acceleration mechanisms, 2022. URL https://arxiv.org/abs/2202.09170.

[3] P. A. R. Ade, N. Aghanim, M. Arnaud, M. Ashdown, J. Aumont, C. Baccigalupi, A. J. Banday, R. B. Barreiro, J. G. Bartlett, N. Bartolo, E. Battaner, R. Battye, K. Benabed, A. Benoît, A. Benoit-Lévy, J.-P. Bernard, M. Bersanelli, P. Bielewicz, J. J. Bock, A. Bonaldi, L. Bonavera, J. R. Bond, J. Borrill, F. R. Bouchet, F. Boulanger, M. Bucher, C. Burigana, R. C. Butler, E. Calabrese, J.-F. Cardoso, A. Catalano, A. Challinor, A. Chamballu, R.-R. Chary, H. C. Chiang, J. Chluba, P. R. Christensen, S. Church, D. L. Clements, S. Colombi, L. P. L. Colombo, C. Combet, A. Coulais, B. P. Crill, A. Curto, F. Cuttaia, L. Danese, R. D. Davies, R. J. Davis, P. de Bernardis, A. de Rosa, G. de Zotti, J. Delabrouille, F.-X. Désert, E. Di Valentino, C. Dickinson, J. M. Diego, K. Dolag, H. Dole, S. Donzelli, O. Doré, M. Douspis, A. Ducout, J. Dunkley, X. Dupac, G. Efstathiou, F. Elsner, T. A. Enßlin, H. K. Eriksen, M. Farhang, J. Fergusson, F. Finelli, O. Forni, M. Frailis, A. A. Fraisse, E. Franceschi, A. Frejsel, S. Galeotta, S. Galli, K. Ganga, C. Gauthier, M. Gerbino, T. Ghosh, M. Giard, Y. Giraud-Héraud, E. Giusarma, E. Gjerløw, J. González-Nuevo, K. M. Górski, S. Gratton, A. Gregorio, A. Gruppuso, J. E. Gudmundsson, J. Hamann, F. K. Hansen, D. Hanson, D. L. Harrison, G. Helou, S. Henrot-Versillé, C. Hernández-Monteagudo, D. Herranz, S. R. Hildebrandt, E. Hivon, M. Hobson, W. A. Holmes, A. Hornstrup, W. Hovest, Z. Huang, K. M. Huffenberger, G. Hurier, A. H. Jaffe, T. R. Jaffe, W. C. Jones, M. Juvela, E. Keihänen, R. Keskitalo, T. S. Kisner, R. Kneissl, J. Knoche, L. Knox, M. Kunz, H. Kurki-Suonio, G. Lagache, A. Lähteenmäki, J.-M. Lamarre, A. Lasenby, M. Lattanzi, C. R. Lawrence, J. P. Leahy, R. Leonardi, J. Lesgourgues, F. Levrier, A. Lewis, M. Liguori, P. B. Lilje, M. Linden-Vørnle, M. López-Caniego, P. M. Lubin, J. F. Macías-Pérez, G. Maggio, D. Maino, N. Mandolesi, A. Mangilli, A. Marchini, M. Maris, P. G. Martin, M. Martinelli, E. Martínez-González, S. Masi, S. Matarrese, P. McGehee, P. R. Meinhold, A. Melchiorri, J.-B. Melin, L. Mendes, A. Mennella, M. Migliaccio, M. Millea, S. Mitra, M.-A. Miville-Deschênes, A. Moneti, L. Montier, G. Morgante, D. Mortlock, A. Moss, D. Munshi, J. A. Murphy, P. Naselsky, F. Nati, P. Natoli, C. B. Netterfield, H. U. Nørgaard-Nielsen, F. Noviello, D. Novikov, I. Novikov, C. A. Oxborrow, F. Paci, L. Pagano, F. Pajot, R. Paladini, D. Paoletti, B. Partridge, F. Pasian, G. Patanchon, T. J. Pearson, O. Perdereau, L. Perotto, F. Perrotta, V. Pettorino, F. Piacentini, M. Piat, E. Pierpaoli, D. Pietrobon, S. Plaszczynski, E. Pointecouteau, G. Polenta, L. Popa, G. W. Pratt, G. Prézeau, S. Prunet, J.-L. Puget, J. P. Rachen, W. T. Reach, R. Rebolo, M. Reinecke, M. Remazeilles, C. Renault, A. Renzi, I. Ristorcelli, G. Rocha, C. Rosset, M. Rossetti, G. Roudier, B. Rouillé d'Orfeuil, M. Rowan-Robinson, J. A. Rubiño-Martín, B. Rusholme, N. Said, V. Salvatelli, L. Salvati, M. Sandri, D. Santos, M. Savelainen, G. Savini, D. Scott, M. D. Seiffert, P. Serra, E. P. S. Shellard, L. D. Spencer, M. Spinelli, V. Stolyarov, R. Stompor, R. Sudiwala, R. Sunyaev, D. Sutton, A.-S. Suur-Uski, J.-F. Sygnet, J. A. Tauber, L. Terenzi, L. Toffolatti, M. Tomasi, M. Tristram, T. Trombetti, M. Tucci, J. Tuovinen, M. Türler, G. Umana, L. Valenziano, J. Valiviita, F. Van Tent, P. Vielva, F. Villa, L. A. Wade, B. D. Wandelt, I. K. Wehus, M. White, S. D. M. White, A. Wilkinson, D. Yvon, A. Zacchei, and A. Zonca. Planck2015 results: Xiii. cosmological parameters. *A&A*, 594:A13, September 2016. ISSN 1432-0746. doi: 10.1051/0004-6361/201525830. URL http://dx.doi.org/10.1051/0004-6361/201525830.

[4] Takuya Akahori, B. M. Gaensler, and Dongsu Ryu. Statistical techniques for detecting the intergalactic magnetic field from large samples of extragalactic faraday rotation data. *The Astrophysical Journal*, 790 (2):123, July 2014. ISSN 1538-4357. doi: 10.1088/0004-637x/790/2/123. URL http://dx.doi.org/10.1088/0004-637X/790/2/123.

[5] A D Amaral, T Vernstrom, and B M Gaensler. Constraints on large-scale magnetic fields in the intergalactic medium using cross-correlation methods. *Monthly Notices of the Royal Astronomical Society*, 503(2):2913–2926, February 2021. ISSN 1365-2966. doi: 10.1093/mnras/stab564. URL http://dx.doi.org/10.1093/mnras/stab564.

[6] Luan B. Arbeletche and Vitor de Souza. Parametrization of the angular distribution of cherenkov light in air showers. *The European Physical Journal C*, 81(2):195, 2021. ISSN 1434-6052. doi: 10.1140/epjc/s10052-021-08971-7. URL https://doi.org/10.1140/epjc/s10052-021-08971-7.

[7] S. Bertone, C. Vogt, and T. Ensslin. Magnetic field seeding by galactic winds. *Monthly Notices of*

the Royal Astronomical Society, 370(1):319–330, July 2006. ISSN 1365-2966. doi: 10.1111/j.1365-2966.2006.10474.x. URL http://dx.doi.org/10.1111/j.1365-2966.2006.10474.x.

[8] Jonathan Biteau. What do we know about cosmic rays with energies above 5 eev?, 2024. URL https://arxiv.org/abs/2412.13077.

[9] A. Bonafede, L. Feretti, M. Murgia, F. Govoni, G. Giovannini, D. Dallacasa, K. Dolag, and G. B. Taylor. The Coma cluster magnetic field from Faraday rotation measures. *A&A*, 513:A30+, April 2010. doi: 10.1051/0004-6361/200913696.

[10] K. Bondarenko, A. Boyarsky, A. Korochkin, A. Neronov, D. Semikoz, and A. Sokolenko. Account of the baryonic feedback effect in γ-ray measurements of intergalactic magnetic fields. *A&A*, 660:A80, April 2022. doi: 10.1051/0004-6361/202141595.

[11] S. Brown, T. Vernstrom, E. Carretti, K. Dolag, B. M. Gaensler, L. Staveley-Smith, G. Bernardi, M. Haverkorn, M. Kesteven, and S. Poppi. Limiting magnetic fields in the cosmic web with diffuse radio emission. *Monthly Notices of the Royal Astronomical Society*, 468(4):4246–4253, 03 2017. ISSN 0035-8711. doi: 10.1093/mnras/stx746. URL https://doi.org/10.1093/mnras/stx746.

[12] Gianfranco Brunetti and Franco Vazza. Second-order fermi reacceleration mechanisms and large-scale synchrotron radio emission in intracluster bridges. *Phys. Rev. Lett.*, 124:051101, Feb 2020. doi: 10.1103/PhysRevLett.124.051101. URL https://link.aps.org/doi/10.1103/PhysRevLett.124.051101.

[13] Iryna S. Butsky, Philip F. Hopkins, Philipp Kempski, Sam B. Ponnada, Eliot Quataert, and Jonathan Squire. Galactic cosmic-ray scattering due to intermittent structures, 2024. URL https://arxiv.org/abs/2308.06316.

[14] E. Carretti, F. Vazza, S. P. O'Sullivan, V. Vacca, A. Bonafede, G. Heald, C. Horellou, S. Mtchedlidze, and T. Vernstrom. On the nature of LOFAR RMs and new constraints on magnetic fields in cosmic filaments and on magnetogenesis scenarios. *arXiv e-prints*, art. arXiv:2411.13499, November 2024. doi: 10.48550/arXiv.2411.13499.

[15] E. Carretti, F. Vazza, S. P. O'Sullivan, V. Vacca, A. Bonafede, G. Heald, C. Horellou, S. Mtchedlidze, and T. Vernstrom. The nature of LOFAR rotation measures and new constraints on magnetic fields in cosmic filaments and on magnetogenesis scenarios. *A&A*, 693:A208, January 2025. doi: 10.1051/0004-6361/202451333.

[16] Ettore Carretti and Franco Vazza. Radio Observations as a Probe of Cosmic Web Magnetism. *Universe*, 11(5):164, May 2025. doi: 10.3390/universe11050164.

[17] The Pierre Auger Collaboration, A. Aab, P. Abreu, M. Aglietta, I. Al Samarai, I. F. M. Albuquerque, I. Allekotte, A. Almela, J. Alvarez Castillo, J. Alvarez-Muñiz, G. A. Anastasi, L. Anchordoqui, B. Andrada, S. Andringa, C. Aramo, F. Arqueros, N. Arsene, H. Asorey, P. Assis, J. Aublin, G. Avila, A. M. Badescu, A. Balaceanu, F. Barbato, R. J. Barreira Luz, J. J. Beatty, K. H. Becker, J. A. Bellido, C. Berat, M. E. Bertaina, X. Bertou, P. L. Biermann, P. Billoir, J. Biteau, S. G. Blaess, A. Blanco, J. Blazek, C. Bleve, M. Boháčová, D. Boncioli, C. Bonifazi, N. Borodai, A. M. Botti, J. Brack, I. Brancus, T. Bretz, A. Bridgeman, F. L. Briechle, P. Buchholz, A. Bueno, S. Buitink, M. Buscemi, K. S. Caballero-Mora, L. Caccianiga, A. Cancio, F. Canfora, L. Caramete, R. Caruso, A. Castellina, G. Cataldi, L. Cazon, A. G. Chavez, J. A. Chinellato, J. Chudoba, R. W. Clay, A. Cobos, R. Colalillo, A. Coleman, L. Collica, M. R. Coluccia, R. Conceição, G. Consolati, F. Contreras, M. J. Cooper, S. Coutu, C. E. Covault, J. Cronin, S. D'Amico, B. Daniel, S. Dasso, K. Daumiller, B. R. Dawson, R. M. de Almeida, S. J. de Jong, G. De Mauro, J. R. T. de Mello Neto, I. De Mitri, J. de Oliveira, V. de Souza, J. Debatin, O. Deligny, C. Di Giulio, A. Di Matteo, M. L. Díaz Castro, F. Diogo, C. Dobrigkeit, J. C. D'Olivo, Q. Dorosti, R. C. dos Anjos, M. T. Dova, A. Dundovic, J. Ebr, R. Engel, M. Erdmann, M. Erfani, C. O. Escobar, J. Espadanal, A. Etchegoyen, H. Falcke, G. Farrar, A. C. Fauth, N. Fazzini, F. Fenu, B. Fick, J. M. Figueira, A. Filipčič, O. Fratu, M. M. Freire, T. Fujii, A. Fuster, R. Gaior, B. García, D. Garcia-Pinto, F. Gaté, H. Gemmeke, A. Gherghel-Lascu, P. L. Ghia, U. Giaccari, M. Giammarchi, M. Giller, D. Głas, C. Glaser, G. Golup, M. Gómez Berisso, P. F. Gómez Vitale, N. González, A. Gorgi, P. Gorham,

A. F. Grillo, T. D. Grubb, F. Guarino, G. P. Guedes, M. R. Hampel, P. Hansen, D. Harari, T. A. Harrison, J. L. Harton, A. Haungs, T. Hebbeker, D. Heck, P. Heimann, A. E. Herve, G. C. Hill, C. Hojvat, E. Holt, P. Homola, J. R. Hörandel, P. Horvath, M. Hrabovský, T. Huege, J. Hulsman, A. Insolia, P. G. Isar, I. Jandt, S. Jansen, J. A. Johnsen, M. Josebachuili, J. Jurysek, A. Kääpä, O. Kambeitz, K. H. Kampert, I. Katkov, B. Keilhauer, N. Kemmerich, E. Kemp, J. Kemp, R. M. Kieckhafer, H. O. Klages, M. Kleifges, J. Kleinfeller, R. Krause, N. Krohm, D. Kuempel, G. Kukec Mezek, N. Kunka, A. Kuotb Awad, D. LaHurd, M. Lauscher, R. Legumina, M. A. Leigui de Oliveira, A. Letessier-Selvon, I. Lhenry-Yvon, K. Link, D. Lo Presti, L. Lopes, R. López, A. López Casado, Q. Luce, A. Lucero, M. Malacari, M. Mallamaci, D. Mandat, P. Mantsch, A. G. Mariazzi, I. C. Mariş, G. Marsella, D. Martello, H. Martinez, O. Martínez Bravo, J. J. Masías Meza, H. J. Mathes, S. Mathys, J. Matthews, J. A. J. Matthews, G. Matthiae, E. Mayotte, P. O. Mazur, C. Medina, G. Medina-Tanco, D. Melo, A. Menshikov, K.-D. Merenda, S. Michal, M. I. Micheletti, L. Middendorf, L. Miramonti, B. Mitrica, D. Mockler, S. Mollerach, F. Montanet, C. Morello, M. Mostafá, A. L. Müller, G. Müller, M. A. Muller, S. Müller, R. Mussa, I. Naranjo, L. Nellen, P. H. Nguyen, M. Niculescu-Oglinzanu, M. Niechciol, L. Niemietz, T. Niggemann, D. Nitz, D. Nosek, V. Novotny, L. Nožka, L. A. Núñez, L. Ochilo, F. Oikonomou, A. Olinto, M. Palatka, J. Pallotta, P. Papenbreer, G. Parente, A. Parra, T. Paul, M. Pech, F. Pedreira, J. Pkala, R. Pelayo, J. Peña-Rodriguez, L. A. S. Pereira, M. Perlín, L. Perrone, C. Peters, S. Petrera, J. Phuntsok, R. Piegaia, T. Pierog, P. Pieroni, M. Pimenta, V. Pirronello, M. Platino, M. Plum, C. Porowski, R. R. Prado, P. Privitera, M. Prouza, E. J. Quel, S. Querchfeld, S. Quinn, R. Ramos-Pollan, J. Rautenberg, D. Ravignani, B. Revenu, J. Ridky, F. Riehn, M. Risse, P. Ristori, V. Rizi, W. Rodrigues de Carvalho, G. Rodriguez Fernandez, J. Rodriguez Rojo, D. Rogozin, M. J. Roncoroni, M. Roth, E. Roulet, A. C. Rovero, P. Ruehl, S. J. Saffi, A. Saftoiu, F. Salamida, H. Salazar, A. Saleh, F. Salesa Greus, G. Salina, F. Sánchez, P. Sanchez-Lucas, E. M. Santos, E. Santos, F. Sarazin, R. Sarmento, C. A. Sarmiento, R. Sato, M. Schauer, V. Scherini, H. Schieler, M. Schimp, D. Schmidt, O. Scholten, P. Schovánek, F. G. Schröder, A. Schulz, J. Schumacher, S. J. Sciutto, A. Segreto, M. Settimo, A. Shadkam, R. C. Shellard, G. Sigl, G. Silli, O. Sima, A. Śmiałkowski, R. Šmída, G. R. Snow, P. Sommers, S. Sonntag, J. Sorokin, R. Squartini, D. Stanca, S. Stanič, J. Stasielak, P. Stassi, F. Strafella, F. Suarez, M. Suarez Durán, T. Sudholz, T. Suomijärvi, A. D. Supanitsky, J. Šupík, J. Swain, Z. Szadkowski, A. Taboada, O. A. Taborda, A. Tapia, V. M. Theodoro, C. Timmermans, C. J. Todero Peixoto, L. Tomankova, B. Tomé, G. Torralba Elipe, P. Travnicek, M. Trini, R. Ulrich, M. Unger, M. Urban, J. F. Valdés Galicia, I. Valiño, L. Valore, G. van Aar, P. van Bodegom, A. M. van den Berg, A. van Vliet, E. Varela, B. Vargas Cárdenas, G. Varner, R. A. Vázquez, D. Veberič, C. Ventura, I. D. Vergara Quispe, V. Verzi, J. Vicha, L. Villaseñor, S. Vorobiov, H. Wahlberg, O. Wainberg, D. Walz, A. A. Watson, M. Weber, A. Weindl, L. Wiencke, H. Wilczyński, M. Wirtz, D. Wittkowski, B. Wundheiler, L. Yang, A. Yushkov, E. Zas, D. Zavrtanik, M. Zavrtanik, A. Zepeda, B. Zimmermann, M. Ziolkowski, Z. Zong, and F. Zuccarello. Observation of a large-scale anisotropy in the arrival directions of cosmic rays above 8 × 10¡sup¿18¡/sup¿ ev. *Science*, 357(6357):1266–1270, 2017. doi: 10.1126/science.aan4338. URL https://www.science.org/doi/abs/10.1126/science.aan4338.

[18] James W. Cronin. From spontaneous ionization to subatomic physics: Some vignettes from cosmic ray history. *Astroparticle Physics*, 53:6–18, 2014. ISSN 0927-6505. doi: https://doi.org/10.1016/j.astropartphys.2013.04.003. URL https://www.sciencedirect.com/science/article/pii/S0927650513000613. Centenary of cosmic ray discovery.

[19] Viktor K. Decyk, Warren B. Mori, and Fei Li. An analytic boris pusher for plasma simulation. *Computer Physics Communications*, 282:108559, 2023. ISSN 0010-4655. doi: https://doi.org/10.1016/j.cpc.2022.108559. URL https://www.sciencedirect.com/science/article/pii/S0010465522002788.

[20] J. Donnert, F. Vazza, M. Brüggen, and J. ZuHone. Magnetic Field Amplification in Galaxy Clusters and Its Simulation. *Space Sci. Rev.*, 214(8):122, December 2018. doi: 10.1007/s11214-018-0556-8.

[21] Y. Dubois and R. Teyssier. Cosmological mhd simulation of a cooling flow cluster. *A&A*, 482(2): L13–L16, March 2008. ISSN 1432-0746. doi: 10.1051/0004-6361:200809513. URL http://dx.doi.org/10.1051/0004-6361:200809513.

[22] R. Durrer and A. Neronov. Cosmological magnetic fields: their generation, evolution and observation. *A&A Rev.*, 21:62, June 2013. doi: 10.1007/s00159-013-0062-7.

[23] Carmelo Evoli, Daniele Gaggero, Andrea Vittino, Mattia Di Mauro, Dario Grasso, and Mario Nicola Mazziotta. Cosmic-ray propagation with DRAGON2: II. Nuclear interactions with the interstellar gas. *J. Cosmology Astropart. Phys.*, 2018(7):006, July 2018. doi: 10.1088/1475-7516/2018/07/006.

[24] Thomas K. Gaisser, Ralph Engel, and Elisa Resconi. *Cosmic Rays and Particle Physics*. Cambridge University Press, 2 edition, 2016.

[25] M. Gaspari, D. Eckert, S. Ettori, P. Tozzi, L. Bassini, E. Rasia, F. Brighenti, M. Sun, S. Borgani, S. D. Johnson, G. R. Tremblay, J. M. Stone, P. Temi, H. Y. K. Yang, F. Tombesi, and M. Cappi. The X-Ray Halo Scaling Relations of Supermassive Black Holes. *ApJ*, 884(2):169, October 2019. doi: 10.3847/1538-4357/ab3c5d.

[26] S. Hackstein, F. Vazza, M. Brüggen, G. Sigl, and A. Dundovic. Propagation of ultrahigh energy cosmic rays in extragalactic magnetic fields: a view from cosmological simulations. *MNRAS*, 462:3660–3671, November 2016. doi: 10.1093/mnras/stw1903.

[27] S. Hackstein, F. Vazza, M. Brüggen, J. G. Sorce, and S. Gottlöber. Simulations of ultra-high energy cosmic rays in the local Universe and the origin of cosmic magnetic fields. *MNRAS*, 475(2):2519–2529, April 2018. doi: 10.1093/mnras/stx3354.

[28] E. R. Harrison. Magnetic fields in the early universe. *Monthly Notices of the Royal Astronomical Society*, 165(2):185–200, 11 1973. ISSN 0035-8711. doi: 10.1093/mnras/165.2.185. URL https://doi.org/10.1093/mnras/165.2.185.

[29] A. M. Hillas. The Origin of Ultra-High-Energy Cosmic Rays. *ARA&A*, 22:425–444, January 1984. doi: 10.1146/annurev.aa.22.090184.002233.

[30] T. Kahniashvili, A. Brandenburg, and A. G. Tevzadze. The evolution of primordial magnetic fields since their generation. *Phys. Scr*, 91(10):104008, October 2016. doi: 10.1088/0031-8949/91/10/104008.

[31] O. Kalashev, A. Korochkin, A. Neronov, and D. Semikoz. Modeling the propagation of very-high-energy γ-rays with the CRbeam code: Comparison with CRPropa and ELMAG codes. *A&A*, 675:A132, July 2023. doi: 10.1051/0004-6361/202243364.

[32] R. C. Kennicutt, Jr. The Global Schmidt Law in Star-forming Galaxies. *ApJ*, 498:541–552, May 1998. doi: 10.1086/305588.

[33] A. V. Kravtsov. On the Origin of the Global Schmidt Law of Star Formation. *ApJ*, 590:L1–L4, June 2003. doi: 10.1086/376674.

[34] R. M. Kulsrud, R. Cen, J. P. Ostriker, and D. Ryu. The Protogalactic Origin for Cosmic Magnetic Fields. *ApJ*, 480:481–491, May 1997. doi: 10.1086/303987.

[35] Nicola Locatelli, Franco Vazza, and Paola Domínguez-Fernández. The challenge of detecting intracluster filaments with faraday rotation, 2018. URL https://arxiv.org/abs/1811.11198.

[36] Nicola Locatelli, Franco Vazza, Annalisa Bonafede, Serena Banfi, Gianni Bernardi, Claudio Gheller, Andrea Botteon, and Timothy W. Shimwell. New constraints on the magnetic field in cosmic web filaments. *A&A*, 2021. URL https://api.semanticscholar.org/CorpusID:236224850.

[37] L. Merten, S. Aerdker, R. Alves Batista, J. Becker Tjus, J. Dörner, A. Dundovic, B. Eichmann, A. Frie, C. Heiter, M. R. Hoerbe, K. H. Kampert, G. Müller, P. Reichherzer, S. Rossoni, A. Saveliev, L. Schlegel, G. Sigl, A. van Vliet, and T. Winchen. CRPropa 3.2: a public framework for high-energy astroparticle simulations. In *38th International Cosmic Ray Conference*, page 1471, September 2024.

[38] Murgia, M., Govoni, F., Feretti, L., and Giovannini, G. A double radio halo in the close pair of galaxy clusters abell 399 and abell 401. *A&A*, 509:A86, 2010. doi: 10.1051/0004-6361/200913414. URL https://doi.org/10.1051/0004-6361/200913414.

[39] S. Navas, C. Amsler, T. Gutsche, C. Hanhart, J. J. Hernández-Rey, C. Lourenço, A. Masoni, M. Mikhasenko, R. E. Mitchell, C. Patrignani, C. Schwanda, S. Spanier, G. Venanzoni, C. Z. Yuan, K. Agashe, G. Aielli, B. C. Allanach, J. Alvarez-Muñiz, M. Antonelli, E. C. Aschenauer, D. M. Asner, K. Assamagan, H. Baer, Sw. Banerjee, R. M. Barnett, L. Baudis, C. W. Bauer, J. J. Beatty, J. Beringer, A. Bettini, O. Biebel, K. M. Black, E. Blucher, R. Bonventre, R. A. Briere, A. Buckley, V. D. Burkert, M. A. Bychkov, R. N. Cahn, Z. Cao, M. Carena, G. Casarosa, A. Ceccucci, A. Cerri, R. S. Chivukula, G. Cowan, K. Cranmer, V. Crede, O. Cremonesi, G. D'Ambrosio, T. Damour, D. de Florian, A. de Gouvêa, T. DeGrand, S. Demers, Z. Demiragli, B. A. Dobrescu, M. D'Onofrio, M. Doser, H. K. Dreiner, P. Eerola, U. Egede, S. Eidelman, A. X. El-Khadra, J. Ellis, S. C. Eno, J. Erler, V. V. Ezhela, A. Fava, W. Fetscher, B. D. Fields, A. Freitas, H. Gallagher, T. Gershon, Y. Gershtein, T. Gherghetta, M. C. Gonzalez-Garcia, M. Goodman, C. Grab, A. V. Gritsan, C. Grojean, D. E. Groom, M. Grünewald, A. Gurtu, H. E. Haber, M. Hamel, S. Hashimoto, Y. Hayato, A. Hebecker, S. Heinemeyer, K. Hikasa, J. Hisano, A. Höcker, J. Holder, L. Hsu, J. Huston, T. Hyodo, Al. Ianni, M. Kado, M. Karliner, U. F. Katz, M. Kenzie, V. A. Khoze, S. R. Klein, F. Krauss, M. Kreps, P. Križan, B. Krusche, Y. Kwon, O. Lahav, L. P. Lellouch, J. Lesgourgues, A. R. Liddle, Z. Ligeti, C.-J. Lin, C. Lippmann, T. M. Liss, A. Lister, L. Littenberg, K. S. Lugovsky, S. B. Lugovsky, A. Lusiani, Y. Makida, F. Maltoni, A. V. Manohar, W. J. Marciano, J. Matthews, U.-G. Meißner, I.-A. Melzer-Pellmann, P. Mertsch, D. J. Miller, D. Milstead, K. Mönig, P. Molaro, F. Moortgat, M. Moskovic, N. Nagata, K. Nakamura, M. Narain, P. Nason, A. Nelles, M. Neubert, Y. Nir, H. B. O'Connell, C. A. J. O'Hare, K. A. Olive, J. A. Peacock, E. Pianori, A. Pich, A. Piepke, F. Pietropaolo, A. Pomarol, S. Pordes, S. Profumo, A. Quadt, K. Rabbertz, J. Rademacker, G. Raffelt, M. Ramsey-Musolf, P. Richardson, A. Ringwald, D. J. Robinson, S. Roesler, S. Rolli, A. Romaniouk, L. J Rosenberg, J. L. Rosner, G. Rybka, M. G. Ryskin, R. A. Ryutin, B. Safdi, Y. Sakai, S. Sarkar, F. Sauli, O. Schneider, S. Schönert, K. Scholberg, A. J. Schwartz, J. Schwiening, D. Scott, F. Sefkow, U. Seljak, V. Sharma, S. R. Sharpe, V. Shiltsev, G. Signorelli, M. Silari, F. Simon, T. Sjöstrand, P. Skands, T. Skwarnicki, G. F. Smoot, A. Soffer, M. S. Sozzi, C. Spiering, A. Stahl, Y. Sumino, F. Takahashi, M. Tanabashi, J. Tanaka, M. Taševský, K. Terao, K. Terashi, J. Terning, U. Thoma, R. S. Thorne, L. Tiator, M. Titov, D. R. Tovey, K. Trabelsi, P. Urquijo, G. Valencia, R. Van de Water, N. Varelas, L. Verde, I. Vivarelli, P. Vogel, W. Vogelsang, V. Vorobyev, S. P. Wakely, W. Walkowiak, C. W. Walter, D. Wands, D. H. Weinberg, E. J. Weinberg, N. Wermes, M. White, L. R. Wiencke, S. Willocq, C. L. Woody, R. L. Workman, W.-M. Yao, M. Yokoyama, R. Yoshida, G. Zanderighi, G. P. Zeller, R.-Y. Zhu, S.-L. Zhu, F. Zimmermann, P. A. Zyla, J. Anderson, M. Kramer, P. Schaffner, and W. Zheng. Review of particle physics. *Phys. Rev. D*, 110:030001, Aug 2024. doi: 10.1103/PhysRevD.110.030001. URL https://link.aps.org/doi/10.1103/PhysRevD.110.030001.

[40] Eve C. Ostriker. Plasma physics for astrophysics. *Physics Today*, 59(1):58–58, 01 2006. ISSN 0031-9228. doi: 10.1063/1.2180179. URL https://doi.org/10.1063/1.2180179.

[41] S P O'Sullivan, M Brüggen, F Vazza, E Carretti, N T Locatelli, C Stuardi, V Vacca, T Vernstrom, G Heald, C Horellou, T W Shimwell, M J Hardcastle, C Tasse, and H Röttgering. New constraints on the magnetization of the cosmic web using lofar faraday rotation observations. *Monthly Notices of the Royal Astronomical Society*, 495(3):2607–2619, May 2020. ISSN 1365-2966. doi: 10.1093/mnras/staa1395. URL http://dx.doi.org/10.1093/mnras/staa1395.

[42] D. Paoletti and F. Finelli. Constraints on primordial magnetic fields from magnetically-induced perturbations: current status and future perspectives with LiteBIRD and future ground based experiments. *JCAP*, 2019(11):028, November 2019. doi: 10.1088/1475-7516/2019/11/028.

[43] Pignataro, G. V., Bonafede, A., Bernardi, G., de Gasperin, F., Brunetti, G., Pasini, T., Vazza, F., Biava, N., de Jong, J. M. G. H. J., Cassano, R., Botteon, A., Brüggen, M., Röttgering, H. J. A., van Weeren, R. J., and Shimwell, T. W. Abell 0399–abell 0401 radio bridge spectral index: First multi-frequency detection. *AA*, 685:L10, 2024. doi: 10.1051/0004-6361/202450051. URL https://doi.org/10.1051/0004-6361/202450051.

[44] Pignataro, G. V., O'Sullivan, S. P., Bonafede, A., Bernardi, G., Vazza, F., and Carretti, E. Detection of magnetic fields in superclusters of galaxies. *A&A*, 696:A203, 2025. doi: 10.1051/0004-6361/202553709. URL https://doi.org/10.1051/0004-6361/202553709.

[45] Maxim Pshirkov, Peter G. Tinyakov, and Federico R. Urban. Constraints on the extragalactic magnetic fields from the nvss faraday rotation measures. 2016. URL https://api.semanticscholar.org/CorpusID:56119898.

[46] C. Stuardi, S. P. O'Sullivan, A. Bonafede, M. Brüggen, P. Dabhade, C. Horellou, R. Morganti, E. Carretti, G. Heald, M. Iacobelli, and V. Vacca. The lofar view of intergalactic magnetic fields with giant radio galaxies. *A&A*, 638:A48, June 2020. ISSN 1432-0746. doi: 10.1051/0004-6361/202037635. URL http://dx.doi.org/10.1051/0004-6361/202037635.

[47] A. Taylor, Jeroen Stil, and and Sunstrum. A rotation measure image of the sky. *The Astrophysical Journal*, 702:1230, 08 2009. doi: 10.1088/0004-637X/702/2/1230.

[48] J. Tjemsland, M. Meyer, and F. Vazza. Constraining the Astrophysical Origin of Intergalactic Magnetic Fields. *ApJ*, 963(2):135, March 2024. doi: 10.3847/1538-4357/ad22dd.

[49] V. Vacca, N. Oppermann, T. Enßlin, J. Jasche, M. Selig, M. Greiner, H. Junklewitz, M. Reinecke, M. Brüggen, E. Carretti, L. Feretti, C. Ferrari, C. A. Hales, C. Horellou, S. Ideguchi, M. Johnston-Hollitt, R. F. Pizzo, H. Röttgering, T. W. Shimwell, and K. Takahashi. Using rotation measure grids to detect cosmological magnetic fields: A Bayesian approach. *A&A*, 591:A13, June 2016. doi: 10.1051/0004-6361/201527291.

[50] Tanmay Vachaspati. Progress on cosmological magnetic fields. *Reports on Progress in Physics*, 84(7): 074901, June 2021. ISSN 1361-6633. doi: 10.1088/1361-6633/ac03a9. URL http://dx.doi.org/10.1088/1361-6633/ac03a9.

[51] R. J. van Weeren, F. de Gasperin, H. Akamatsu, M. Brüggen, L. Feretti, H. Kang, A. Stroe, and F. Zandanel. Diffuse Radio Emission from Galaxy Clusters. *Space Sci. Rev.*, 215(1):16, Feb 2019. doi: 10.1007/s11214-019-0584-z.

[52] F. Vazza, C. Gheller, F Zanetti, M. Tsizh, E. Carretti, S. Mtchedlidze, and M. Brueggen. The evolution of cosmic ray electrons in the cosmic web: seeding by AGN, star formation and shocks. *arXiv e-prints*, art. arXiv:2501.19041, January 2025. doi: 10.48550/arXiv.2501.19041.

[53] Franco Vazza, Marcus Brueggen, Claudio Gheller, Stefan Hackstein, Denis Wittor, and Paul Marten Hinz. Simulations of extragalactic magnetic fields and of their observables. *Classical and Quantum Gravity*, 2017. URL http://iopscience.iop.org/10.1088/1361-6382/aa8e60.

[54] Franco Vazza, Nicola Locatelli, Kamlesh Rajpurohit, Serena Banfi, Paola Domínguez-Fernández, Denis Wittor, Matteo Angelinelli, Giannandrea Inchingolo, Marisa Brienza, Stefan Hackstein, Daniele Dallacasa, Claudio Gheller, Marcus Brüggen, Gianfranco Brunetti, Annalisa Bonafede, Stefano Ettori, Chiara Stuardi, Daniela Paoletti, and Fabio Finelli. Magnetogenesis and the Cosmic Web: A Joint Challenge for Radio Observations and Numerical Simulations. *Galaxies*, 9(4):109, November 2021. doi: 10.3390/galaxies9040109.

[55] T. Vernstrom, B. M. Gaensler, S. Brown, E. Lenc, and R. P. Norris. Low-frequency radio constraints on the synchrotron cosmic web. *Monthly Notices of the Royal Astronomical Society*, 467(4):4914–4936, 2017. ISSN 0035-8711. doi: 10.1093/mnras/stx424.

[56] T. Vernstrom, B. M. Gaensler, L. Rudnick, and H. Andernach. Differences in faraday rotation between adjacent extragalactic radio sources as a probe of cosmic magnetic fields. *The Astrophysical Journal*, 878(2):92, June 2019. ISSN 1538-4357. doi: 10.3847/1538-4357/ab1f83. URL http://dx.doi.org/10.3847/1538-4357/ab1f83.

[57] A.A. Watson. The role of cherenkov radiation in the detection of ultra-high-energy cosmic rays. *Nuclear Instruments and Methods in Physics Research Section A: Accelerators, Spectrometers, Detectors and Associated Equipment*, 553(1):256–263, 2005. ISSN 0168-9002. doi: https://doi.org/10.1016/j.nima.2005.08.053. URL https://www.sciencedirect.com/science/article/pii/S0168900205016062. Proceedings of the fifth International Workshop on Ring Imaging Detectors.

[58] Hao Xu, Hui Li, David C. Collins, Shengtai Li, and Michael L. Norman. Turbulence and dynamo in galaxy cluster medium: Implications on the origin of cluster magnetic fields. *The Astrophysical Journal*, 698(1):L14–L17, May 2009. ISSN 1538-4357. doi: 10.1088/0004-637x/698/1/l14. URL http://dx.doi.org/10.1088/0004-637X/698/1/L14.